PROJECT REPORT

NASA Contract NAS8-37141
USRA Study Subcontract 3473-01

Observation and Numerical Simulation of a Convective Inititation During COHMEX

By

J. Aaron Song and Michael L. Kaplan

Prepared for:

Michael W. Kalb
Universities Space Research Association
4950 Corporate Drive, Suite 100
Huntsville, AL 35806

Prepared by:

MESO, Inc.
185 Jordan Road
Troy, NY 12180

July 22, 1991

Observation And Numerical Simulation Of A Convective Initiation During COHMEX

J. AARON SONG AND MICHAEL L. KAPLAN

Mesoscale Environmental Simulations and Operations, Inc., 185 Jordan Rd., Troy, NY 12180

1. Introduction

It is generally accepted that atmospheric convection occurs in specific locations where the hydrostatic scales of motion are actively controlling the relative humidity and convective available buoyant energy (Anthes, 1977; Fritsch and Chappell, 1980). However, whether the hydrostatic forcing is very strong, as is the case in baroclinic jet/frontal systems or rather weak as is often the case in local thermodynamically-direct circulations such as sea breezes, orographic uplift, or convective outflow boundaries; how specific volumes of the atmosphere are 'triggered' into convection is not well understood and rarely accurately forecasted.

This storm initiation problem involves atmospheric spatial scales which are shorter than the organizing hydrostatic scales of motion responsible for producing a moist convectively unstable environment, *i.e.*, about 10 km and temporal scales of minutes. With the recent advances of computer speed, such meso-γ scale dynamical pre-convective processes which trigger convection are beginning to be incorporated into numerical simulations which explicitly resolve deep convection. For example, Crook *et al.*(1990), in simulating the regeneration of a nocturnal squall line which is described in detail in Carbone *et al.* (1990), considered three types of the regeneration mechanisms which are all associated with horizontal gradients in the upstream environment. Among them, they found that an increase of low-level moisture and increase of low-level shear following a gust-front (*i.e.* in a Lagrangian framework moving with the gust-front) are both able to lower the level of free convection (LFC) and/or increase the lifting at the gust-front thereby enhancing the convective regeneration. Redelsperger and Clark (1990) found that the spatial organization of the simulated clouds (*i.e.* scale selection of convection) is determined primarily by the magnitude and direction of the shear in the layer

spanning the boundary layer eddies and the overlying quasi-stationary gravity waves. Strong directional shear results in more banded (or two-dimensional) cloud structure, while speed shear results in more scattered (or three-dimensional) structure. Dynamically, the shear itself is maintained through a balance between the shear destruction by boundary layer mixing and shear production by a differential heating on a gentle slope. Tripoli and Cotton (1989a, 1989b) described a complete lifecycle of the interactions among processes which have horizontal scales ranging from cumulus clouds to large scale mountain-plain solenoidal circulations. Yoshizaki and Ogura (1988) found that an essential factor in simulating the observed heavy precipitation in the Big Thompson storm case is the incorporation of a horizontally varying moisture field in association with the local orography.

A common similarity among these studies is that all of them include convectively explicit simulations (Schlesinger, 1982) with initializations including a certain type of environmental horizontal discontinuity in physical fields near the onset of convection. For instance, gradients of terrain heights, gradients of surface moisture or solar heating, or other gradients associated with the surface "boundaries". As discussed in Balaji and Clark (1988), such a convective simulation initialization (or the "near-field" treatment) recognizes localized forcing, such as surface energy fluxes, as effective triggering mechanisms for deep convection. Convective initialization of this type is in contrast to those used when the mature stage convective processes (Klemp *et al.*, 1981) or convective-stratiform interactions (Lafore and Moncrieff,1989) are the main focus. That is, if only the mature stage is of interest, or that a large scale property (such as a strong shear exists horizontally-uniformly in the lower troposphere) and is known to dominate the storm dynamics, the use of a simple "bubble" (Schlesinger, 1982) has been a common way of initializing convective simulations. Due to computer limitations however, the incorporation of realistic environmental "gradients" into convective simulations requires simplification of the environmental forcing. For instance, the above cited studies, in simulating the relationships between cumulus convection and pre-convective processes on the scales of 100-1000 km, are essentially all restricted to two-dimensional models. Clearly, the simplification of considering only two-dimensional flow implies that a certain environmental realism is lost. There has not been, to the knowledge of the authors, studies utilizing convectively explicit simulations which are initialized with realistic environmental forcing in which the three-dimensional structure of both winds and thermodynamic fields are retained. In the current study, an attempt was made to illustrate a "first trial" of such a type of numerical simulation by utilizing a special observational dataset. Specifically, the goal of this study is to understand how exactly an observed convective initiation and its early-stage spatial organization is generated over a "horizontal" area of 200 km across, by using a convectively explicit simulation approach which, as an unavoidable limitation, uses a horizontal grid spacing of 3 km.

The case study chosen for the numerical experiments in this study is the June

28/29 event of COHMEX (COoperative Huntsville Meteorological EXperiment; Summer 1986; Northern Alabama and central Tennessee). A more detailed description of the experimental platform of COHMEX and the general weather conditions is given in Williams *et al.* (1987). Knupp and Williams (1988) provided a qualitative analysis of a series of convective events which occurred during the period of 1200 UTC 28 June to 1200 UTC 29 June, in which the particular period from 2100 to 0000 UTC is of the main concern in this study. Overall, under a synoptically undisturbed condition, a dual-peak convective lifecycle is observed within the COHMEX observational network over a 24-hour period. The lifecycle includes a multicell storm, which lasted about 6 hours and produced a peak rainrate exceeding 100 mm/hour, and a downstream mesoscale convective system. The 24-hour accumulated rainfall of this event is the largest during the entire COHMEX. The downstream mesoscale convective system, unfortunately, has been difficult to investigate quantitatively due to the lack of mesoscale observations. On the other hand, data collected near the time of the multicell storm evolution, including its initiation, is one of the best datasets of COHMEX. In this study, the initiation of this multicell storm is chosen as the target of the numerical simulations.

Given these goals, it is necessary to first describe the observed three-dimensional mesoscale pre-convective evolution leading to the target initiation, from which the numerical simulations will be initialized. Section 2 provides such an observational background. The purpose of section 2 is to provide the most relevant observations which describe how the target convective initiation (hereafter referred to as TCI) was generated based on the data collected. This observational background is then followed by a description of the data preparation in the early part of section 3, which explains how a three-dimensional gridded dataset is established from the observations and how it is used for both the observational analysis included in section 2 and as the input for all the numerical simulations. The numerical model used in this study is then introduced. Once the observational and the numerical background are established, the goal of the study will be more specifically illustrated in section 3, together with a description of how the model outputs in the numerical experiment will be used under the study goal. In the rest of section 3, the control simulation results will be described in detail, together with its verification using the best available observations. The control simulation is then followed by two sensitivity simulations described in section 4. In section 5, the effect of the observed three-dimensional wind field will be briefly discussed in terms of its contribution to the TCI. Section 5 is included because, as will be illustrated, the TCI from all the numerical simulations appears to be determined largely by the pre-convective horizontal thermodynamical distribution and, therefore, receives the most attention throughout this study. In section 6, the implications for mesoscale predictability are briefly discussed specifically regarding the observed large mesoscale spatial variabilities in forcing functions. Finally, a summary and the conclusion of this study are included in section 7.

2. An Observational Analysis

2.1 Synoptic-Scale Background

Figures 2a and 2b show, respectively, the large scale distribution of the 500 mb height field and mean sea level pressure at 1200 UTC 28 June (about 10 hours before the TCI). These large scale patterns should be referenced relative to the COHMEX data network depicted in Figure 1. It is seen that the large scale background in this study is a dynamically quiescent environment, namely a well-developed summertime Bermuda high pressure system located off the Atlantic coast with a quasi-geostrophic southwesterly flow dominating most of the southeastern U.S.. A weak shortwave trough is oriented about northeast-southwest across the Missouri and Mississippi Valley regions throughout the mid-to-lower troposphere. The weakness of the synoptic-scale dynamical forcing in this case can also be clearly realized from the weak winds near the tropopause (not shown) which were only about 10 ms^{-1} everywhere over the COHMEX network area and did not increase before the onset of the TCI. Throughout the day, high moisture (relative humidities, or RH, above 90%) was provided by the lower-tropospheric remnants of Hurricane Bonnie, which was advected into the COHMEX region generally from the southwest during the period prior to the TCI. In fact, the COHMEX mesoscale environment was complicated on June 28 by the merging of the Bonnie remnants and the slowly-moving shortwave trough. Figure 3a shows that the clouds associated with remnants of Bonnie were just upstream from the COHMEX region (*i.e.* over northern Mississippi and southern Arkansas) around 1200 UTC 28 June. Figure 3b shows the cloud distribution 12 hours later, which indicates that the deep convection in the COHMEX area was embedded within the merged complex covering a large scale area. It will be illustrated in this study that the TCI is closely related to the background moisture supply.

2.2 Mesoscale Pre-Convective Destabilization

Around 1800 UTC 28 June (about 4 hours before the TCI), the shortwave trough had propagated into the western network area, as shown by the horizontal wind directions and speeds on the 750 mb analysis depicted in Figure 4. Radar observations (Figure 4) indicate that there was essentially no convection over the COHMEX network area except for the weak cloud activity near the southwest corner around 1800 UTC. The large scale mid-to-lower tropospheric quasi-geostrophic southwesterly flow has a maximum speed of about 16 ms^{-1} near the southeast corner of the network, which results in a weak positive vorticity field over the COHMEX area. The shortwave trough propagated slowly eastward toward the network center during the next 4 hours.

The effect of the low-level moisture supply in conjunction with surface heating and meso-β scale hydrostatic upward motions is found to be rather effective in producing localized destabilization during the pre-convective period. For example, Figure 5 shows the soundings at Lexington, Tennessee, at (a); 1800 and (b); 2100 UTC. It is clearly seen that a significant inversion in 700-850 mb layer at 1800 UTC was completely eliminated by 2100 UTC. Figures 5c and d show similarly the soundings at Columbia, Tennessee. Figure 7 indicates that near Columbia the CAPE values increased by a factor of 4 (from 668 to 2531 Joule/Kg) in no more than 3 hours.

The mid-to-lower tropospheric horizontal wind fields shown in Figures 4 and 5 indicate that during 1800-2100 UTC, the trough axis was located between Lexington and Columbia. Figure 6 shows the moist-static-energy (or MSE, hereafter representing $C_p*T+L*Q_v$, where T and Q_v are temperature and mixing ratio, respectively) field as superimposed upon the wind field and the radar reflectivity field around 2100 UTC. It is seen that the developing convection near Lexington was supported by both the highest MSE over the network area as well as a surface meso-β scale (50-100 km across) region of velocity convergence at the surface. Aside from the Lexington area, there was essentially no convection around 2100 UTC except for the network northern boundary.

The mesoscale pre-convective destabilization may be summarized by the evolution of CAPE values at the COHMEX rawinsonde stations shown in Figure 7. It is seen that the CAPE values at Lexington, Columbia and St. Joseph, Tennessee, (which form a triangular area) all increased by a factor of 2-4 between 1800 and 2100 UTC. This trend continued at St Joseph through 0000 UTC. The CAPE values near these stations increased by 1000 to 2000 (Joule/Kg) during a period of 3 hours or less. Figure 7 shows that at 0000 UTC the highest CAPE values were in the region encompassing St Joseph and Booneville, Mississippi. Therefore, during the 3-hour period of 2100-0000 UTC, the thermodynamically most favorable area for convection was shifted southward from the northwest quadrant (as represented by the triangular area encompassing Lexington, Columbia and St. Joseph) to the southwest quadrant of the domain. As will be clear from this study, this southward shift marks the onset of the TCI which is illustrated below.

2.3 *Target Convective Initiation*

Throughout this study, the target convective initiation (or TCI) refers to the early-stage convective-scale cells which develop and are aligned along the general direction of southwest-northeast across the network center and near the southwest corner during the 3-hour period of 2100-0000 UTC. A more detailed illustration of the sequence of the cell development is given below. It is worth noting that the actual generation of the TCI appears to be closely related to the southward shift of the convectively most favorable zone, which is closely related to the weakening of

the Lexington convection.

As discussed previously, the triangular area surrounded by Lexington, Columbia and St. Joseph appeared to be the convectively most favored area by around 2100 UTC based on the surface MSE and wind distributions. Since the shortwave trough was moving slowly eastward over this area around 2100 UTC, it would be intuitively expected that the developing Lexington convection would strengthen while propagating eastward toward the network center. This did not occur. Instead, Figures 8a and 8b show that the TCI is associated with LOCALLY initiated cells near the network center around 2200 UTC, as opposed to the continuous development of the Lexington convection. By 2310 UTC, shown in Figure 8c, it is seen that the convective cells near the network center had intensified, while the Lexington convection had extended eastward and weakened. Figure 8d indicates that the Lexington convection turned into an anvil-type of inactive cloud by 0000 UTC.

The exact cause of the weakening of the Lexington convection is beyond the scope of this study because it involved processes outside the domain of analysis. Accordingly, this generates problems of time-dependent lateral boundary conditions for a limited-domain model such as that in this study. The implications for the problem of mesoscale predictability will be briefly discussed in section 6. Nevertheless, the fact of the weakening of the Lexington convection during 2100-0000 UTC can be illustrated by a pair of surface PAM observations shown in Figure 9a and 9b. Figure 9a shows that by about 2310 UTC, a convectively-generated surface outflow was recorded at the PAM station #45 in association with the Lexington convection. The outflow characteristics, such as gusty wind, a nearly 2°C cooling, and nearly 1 mb mesohigh pressure perturbation are seen in Figure 9a. However, the rainfall recorded at the same time was negligible. In sharp contrast, Figure 9b shows another surface outflow, recorded at PAM station #46 shortly after 0000 UTC, was accompanied by a large rainrate (which is the peak rainfall associated with the TCI). Therefore, a comparison between Figure 9b and 9a clearly indicates that regardless of the cause of the weakening of the Lexington convection, it is the area encompassing the network center and the southwest corner in which the TCI was generated.

According to the BNA radar observation, as shown in Figure 8a and 8b, the time of TCI appears to be during 2100-2200 UTC. In Figure 10, a detailed illustration of the sequence of development for the 2-hour period from 2000-2200 UTC using the PAM observations is given. Surface wind fields and horizontal divergence fields at 2000, 2020, 2040, 2100, 2130 and 2200 UTC are shown in, respectively, Figures 10a through 10f, which are superimposed upon the radar reflectivity of 2200 UTC. The 2200 UTC BNA radar observation is used throughout this study for the purpose of indicating the location of the TCI. First, Figure 10a shows clearly a surface convergence maximum existed near the Lexington area. Figures 10a through 10c show clearly the aforementioned southward shift (actually southeastward shift),

which occurred during 2000-2100 UTC. The new location of the center of convergence (as analyzed) was in direct proximity to St. Joseph, as seen from Figures 10c through 10f. The excellent alignment between the center of convergence and the convective cells of TCI implies that the TCI is related to the surface convergence.

The importance of this surface meso-β scale (50-100 km across) convergence is likely in its location, rather than its magnitude. The convergences, shown in Figure 10, are all weaker than -3×10^{-5} (s^{-1}). On the other hand, Figures 11a-11d show that because of this convergence the southwest corner area of the COHMEX network became the convectively most favorable zone in which the TCI was generated. The surface wind field around the southwest corner, shown in Figure 11a, is seen to be accompanying the background southwesterly flow and therefore the advection of the upstream moisture into the network area. Figure 11b shows the RH values are 93% or higher around the southwest corner, with the larger RH values bulging toward the northeast. Figure 11c shows the MSE ridge line nearly coincides with the line of the convective cells of the TCI. Furthermore, the convectively favorable condition around the southwest corner can also be understood from the analyzed approximate cloud-base heights. Figure 11d shows the heights of Lifting Condensation Level (LCL, in mb), calculated using the formulation of Bolton (1980) with source air near the surface. It is seen that the surface air parcels in the southwest corner area need to rise only a few hundred meters (*i.e.* a few tens of mb) to reach condensation. Thus, near-saturated air is seen to dominate the lower troposphere around the southwest corner area during the TCI. Figure 12, showing the soundings at St. Joseph which were released at 2015 and 2315 UTC, clearly indicates that completely or nearly saturated air was found throughout a layer between 750 mb and 950 mb by 2315 UTC.

The horizontally concentrated high moisture content also extended over a deep layer. Figures 13a and 13b show the RH values at, respectively, 850 mb and 750 mb around 0000 UTC. It is clearly seen that a band of moistening, or a moist tongue, extended from the southwest corner toward the northeast at 850 mb, or from the southern part of network toward the NNE at 750 mb. The RH values in these narrow bands are 95-98% near the southwest corner at 850 mb, and approximately 94% near St. Joseph at 750 mb.

Because only the early-stage of deep convection is of interest in this study, rainfall accumulations are generally not significant enough to be a good indicator of convective development. Nevertheless, the PAM rainfall data is used to further illustrate the spatial sequence of convective development within the network area. First, Figure 14 shows the horizontal distribution of the 21.5-hour accumulated rainfall (*i.e.* starting from 0000 UTC 28 June) at 2130 UTC. It is seen that due to the aforementioned Lexington convection, the largest rainfall was along the network western boundary by 2310 UTC. For the purpose of this study, the rainfall shown in Figure 14 is considered as not related to TCI, and any rainfall recorded over the area interested (*i.e* the central-southwestern network) after 2130 UTC is considered to be

associated with the TCI. By subtracting out the accumulated rainfall at 2130 UTC, Figures 15a through 15d show, respectively, the rainfall during 2130-2230, 2130-2300, 2130-2330 and 2130-0030 UTC periods. It is seen, by comparing Figure 15b with 15a, that the newly recorded rainfall during 2230-2300 UTC was almost completely around the southwest corner area. On the other hand, Figure 15c shows clearly the rainfall maximum was near the network center by 2330 UTC. Therefore, the PAM observations indicate that the rainfall associated with TCI was first around the southwest corner of the COHMEX network, and moved to be near the network center during the later stages of convective development. This spatial sequence of the TCI development will further be discussed in the next section.

In summary, mesoscale surface, rawinsonde, radar, and satellite datasets of June 28 indicate that a hydrostatic environment conducive to convective development has been established over the southwestern part of the COHMEX network area. This is manifested as maxima in observed values of surface moist-static-energy, mean relative humidity over a substantial depth of the column, and surface velocity convergence. Having established proof for this hydrostatic organization, we will report on the use of a non-hydrostatic convective numerical model to diagnose the dynamical processes which further focus on specific meso-β/meso-γ scale convective initiation.

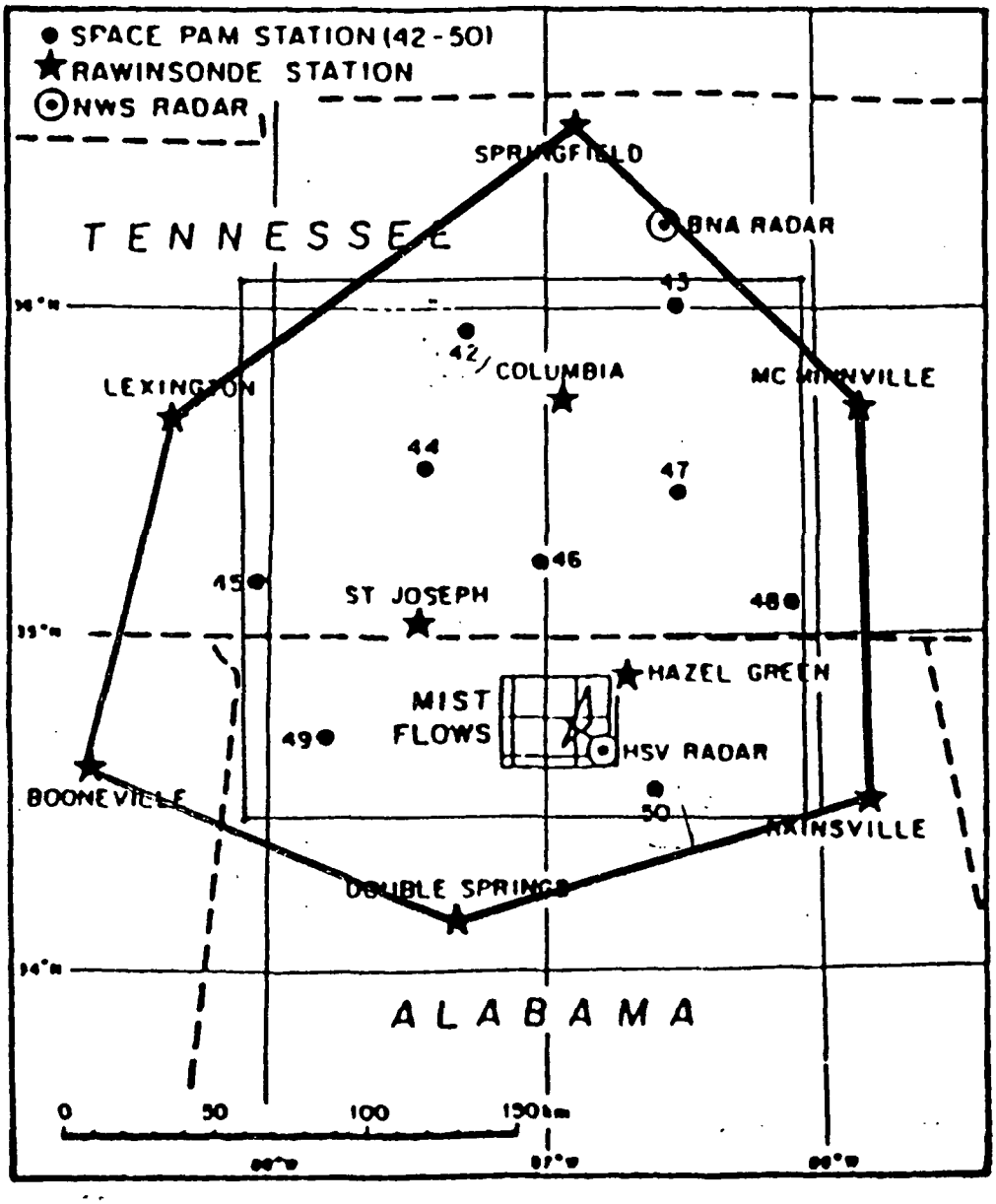

Figure 1: The COHMEX meso-ß scale observational network. The rawinsonde stations are denoted by stars, and the surface PAM stations by dots (which are numbered from 42 to 50). The NWS WSR-57 radar is located at Nashville (BNA), TN. The 3 doppler radars are all located near Huntsville (HSV), AL. Distance scale is shown at the bottom.

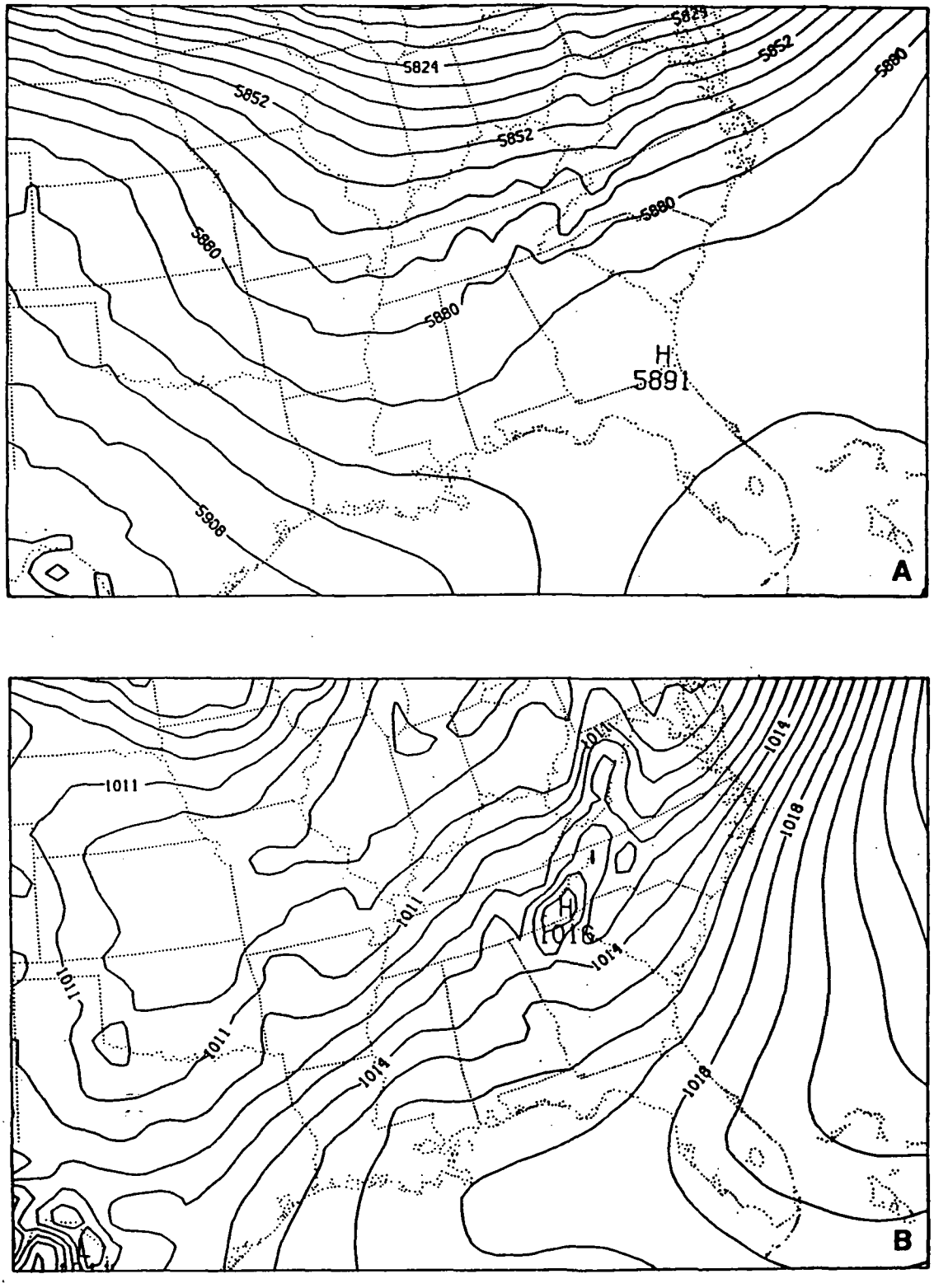

Figure 2: (a) Observed large scale distributions of 500 mb height field and (b) mean sea level pressure field at 1200 UTC 28 June.

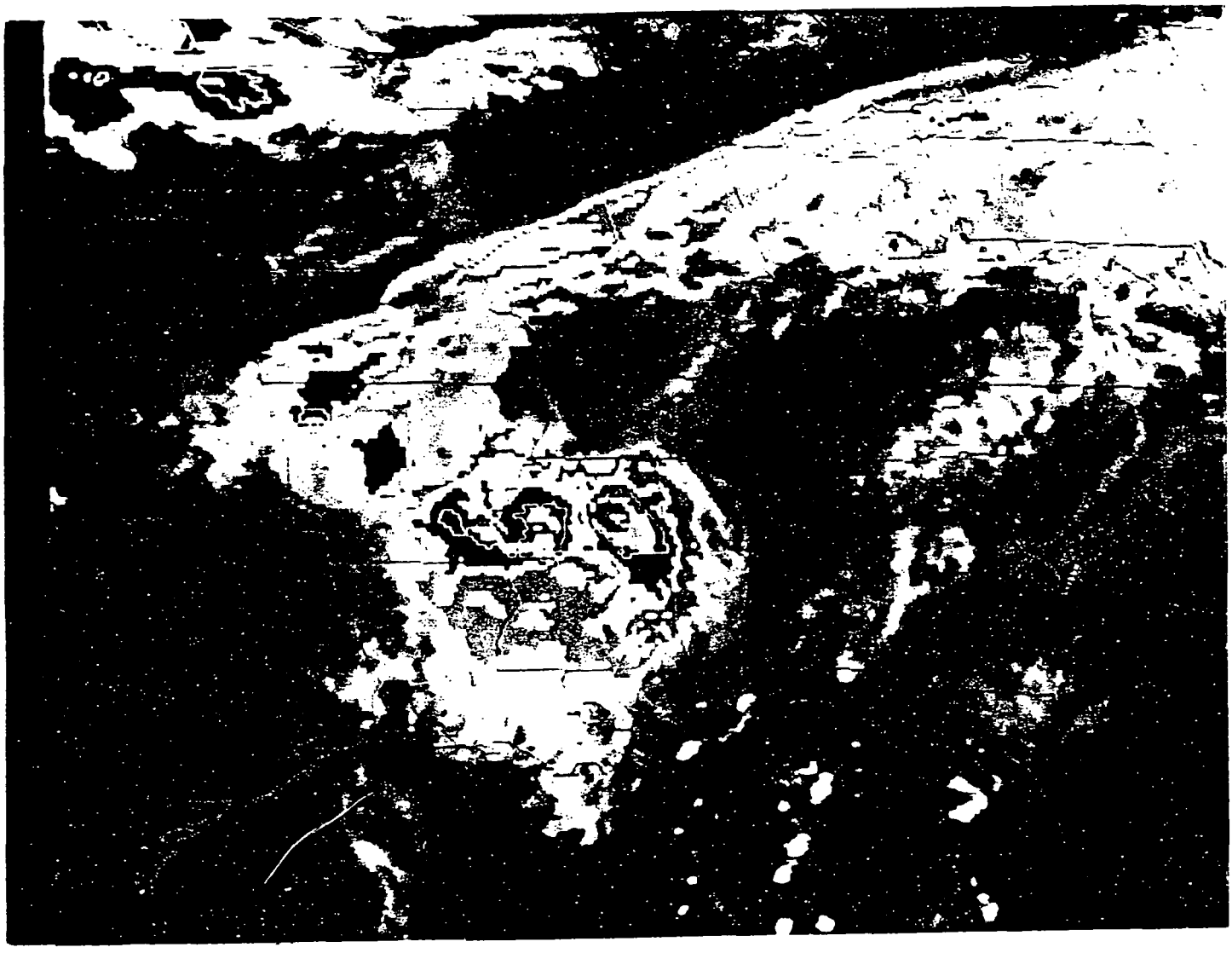

Figure 3a: Visible satellite image at 1200 UTC 28 June

Figure 3b: Visible satellite image at 0000 UTC 29 June.

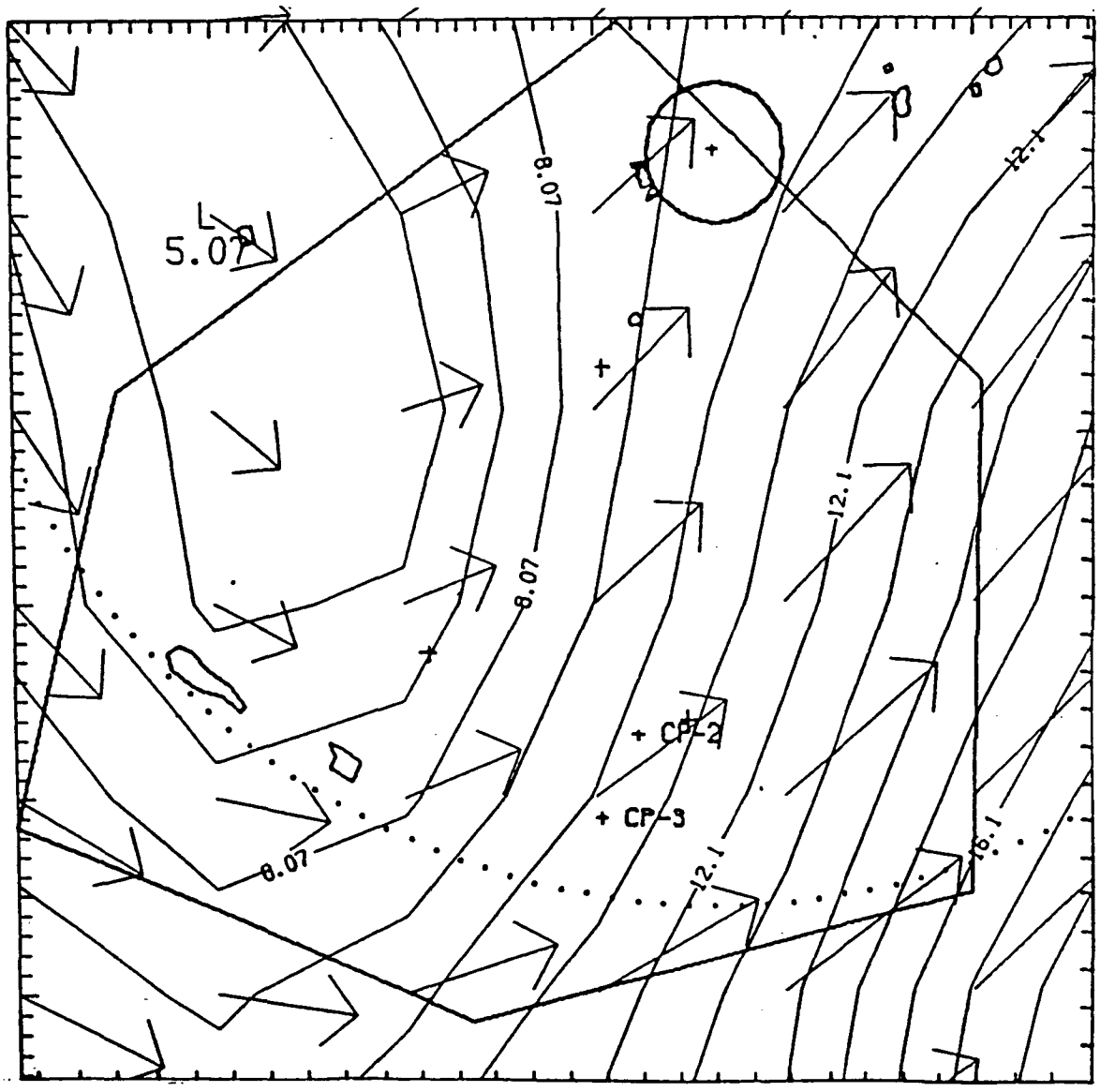

Figure 4: Observed horizontal wind speeds at intervals of 1 ms^{-1}. As superimposed upon the reflectivities (contoured from 18 dBZ) of the BNA radar, over the COHMEX network.

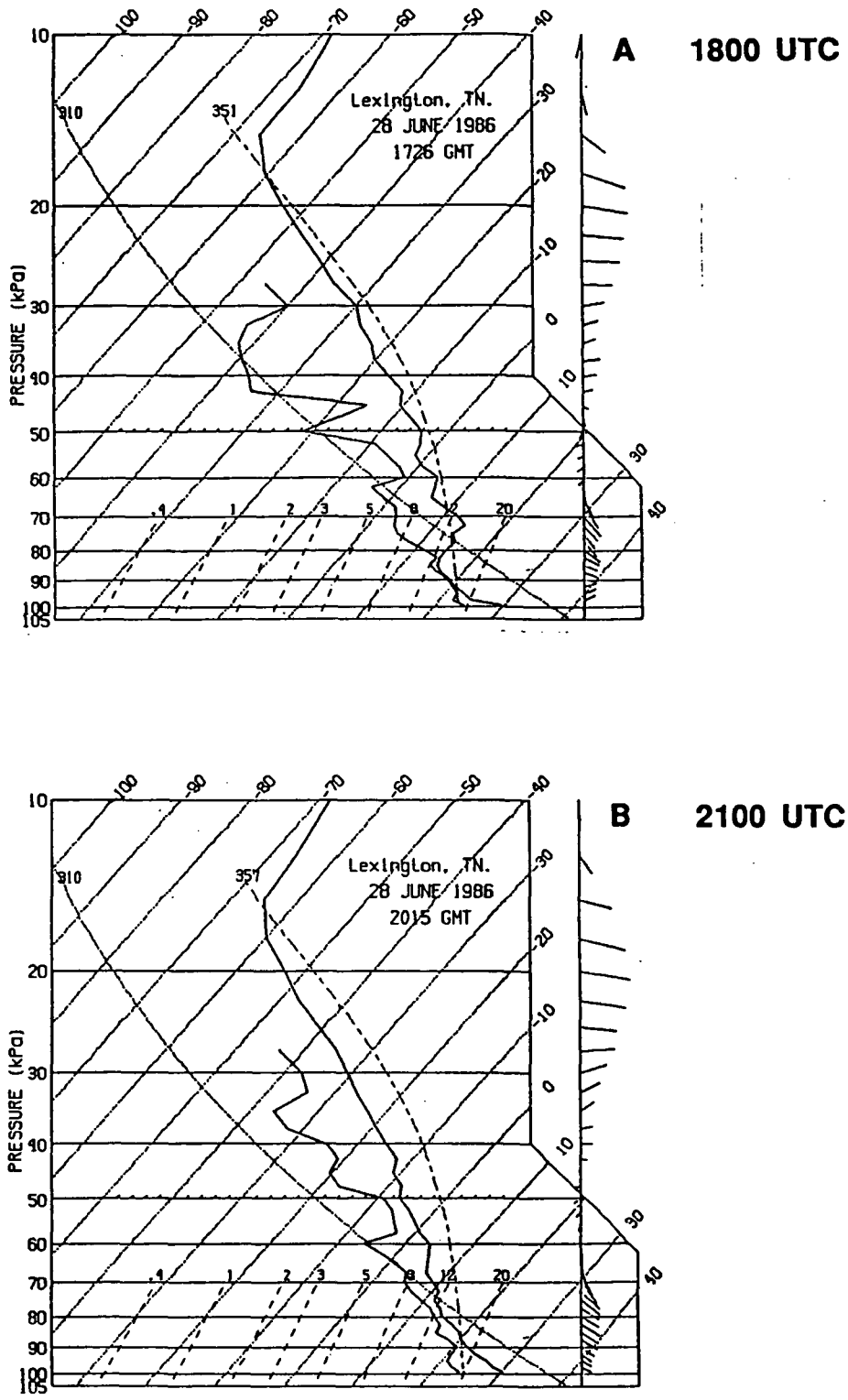

Figure 5: Rawinsonde soundings at Lexington, TN, at (a)1800 and (b) 2100 UTC.

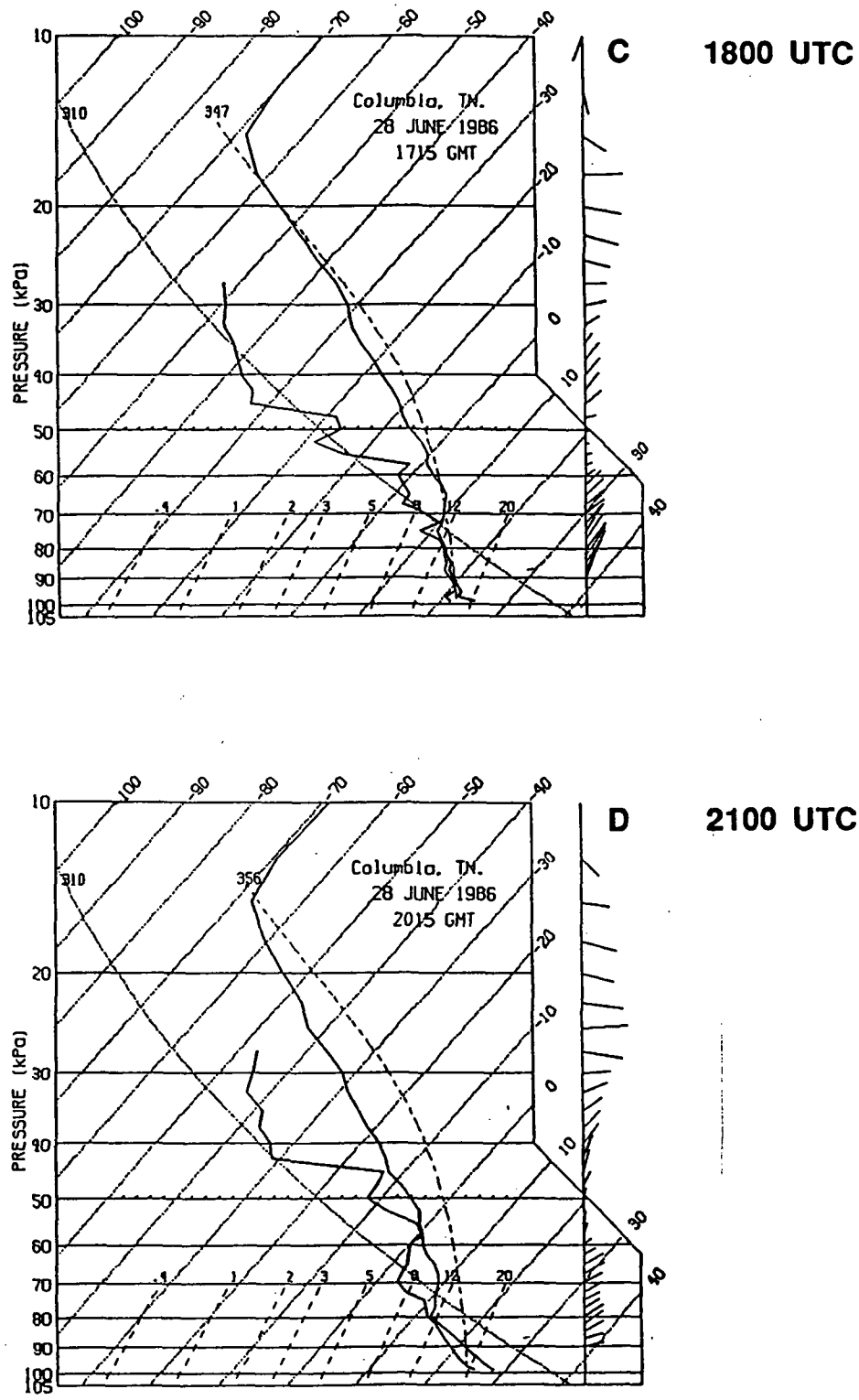

Figure 5: Rawinsonde soundings at Columbia, TN, at (c) 1800 and (d) 2100 UTC.

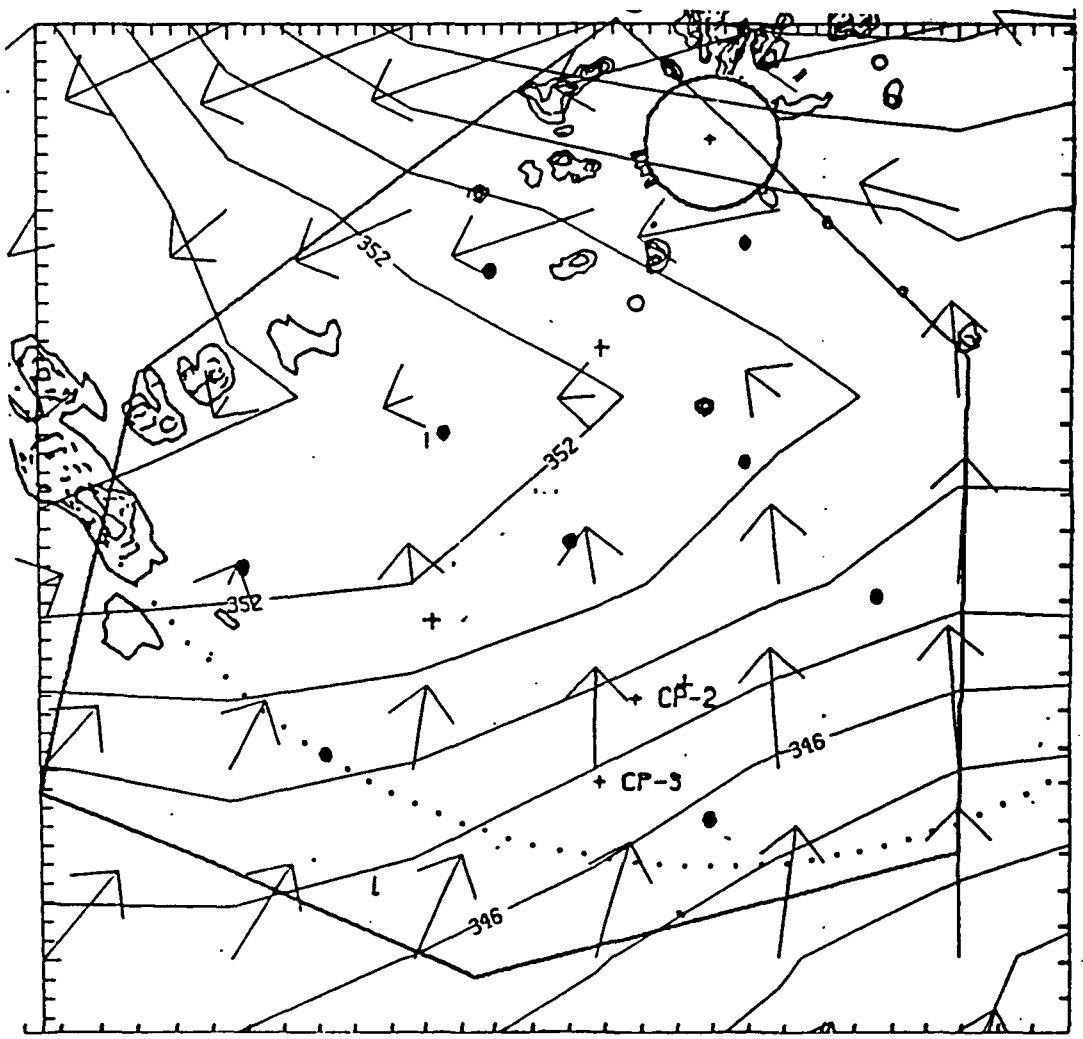

Figure 6: Observed surface wind vector field and the calculated (see text) moist-static-energy (contoured at 1.5 x 10^3 joule/kg) field near the surface at 2100 UTC 28 June, as superimposed upon the BNA radar reflectivities (which are contoured at 18, 30, 38 dBZ), over the COHMEX network.

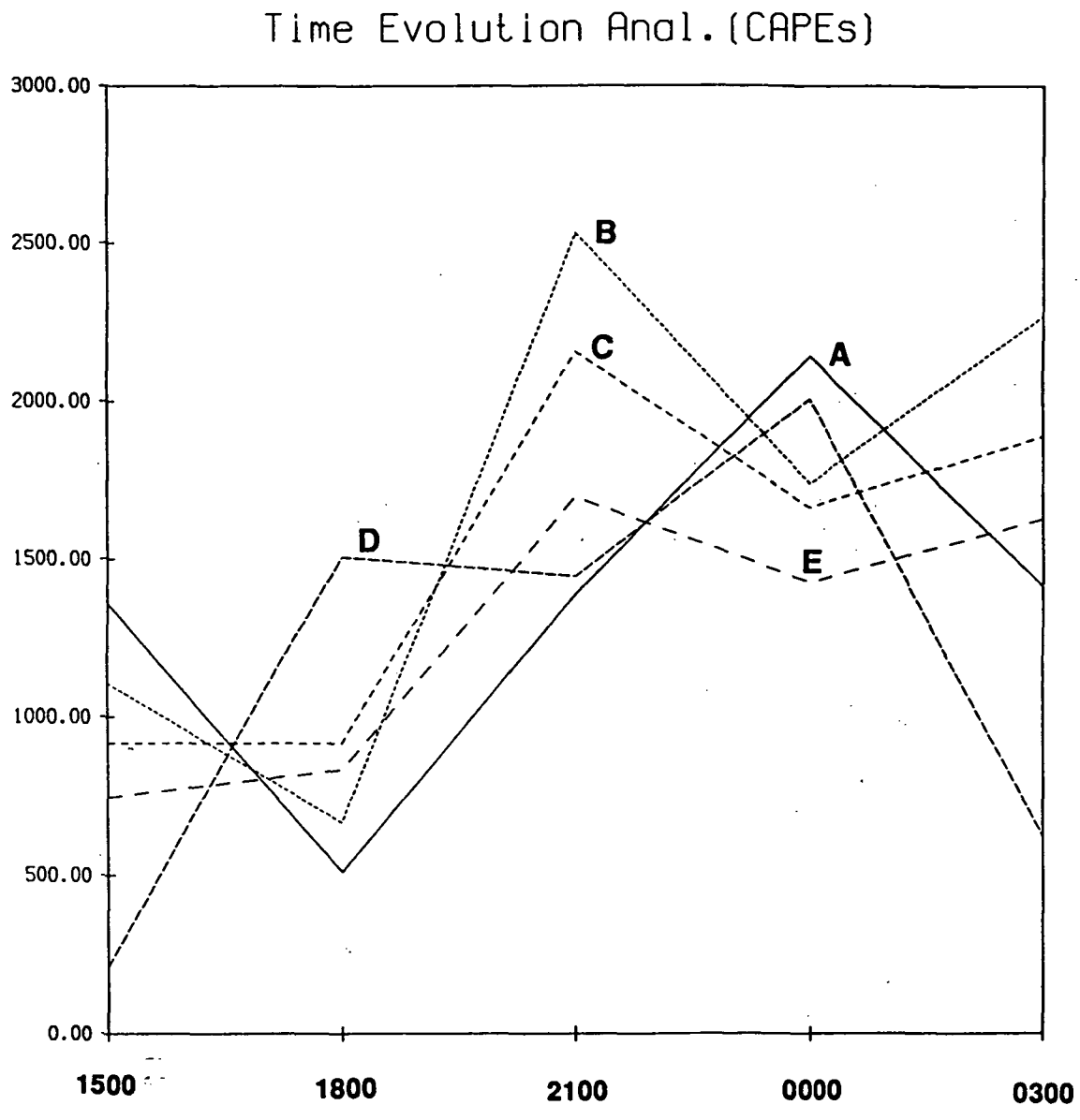

Figure 7: Time evolutions of convective available potential energy at five selected rawinsonde stations using the 3-hour COHMEX sounding data. Abcissa indicate the five rawinsonde times. Line A: St. Joseph, TN; B: Columbia, TN; C: Lexington, TN; D: Booneville, MS; E: Double Springs, AL.

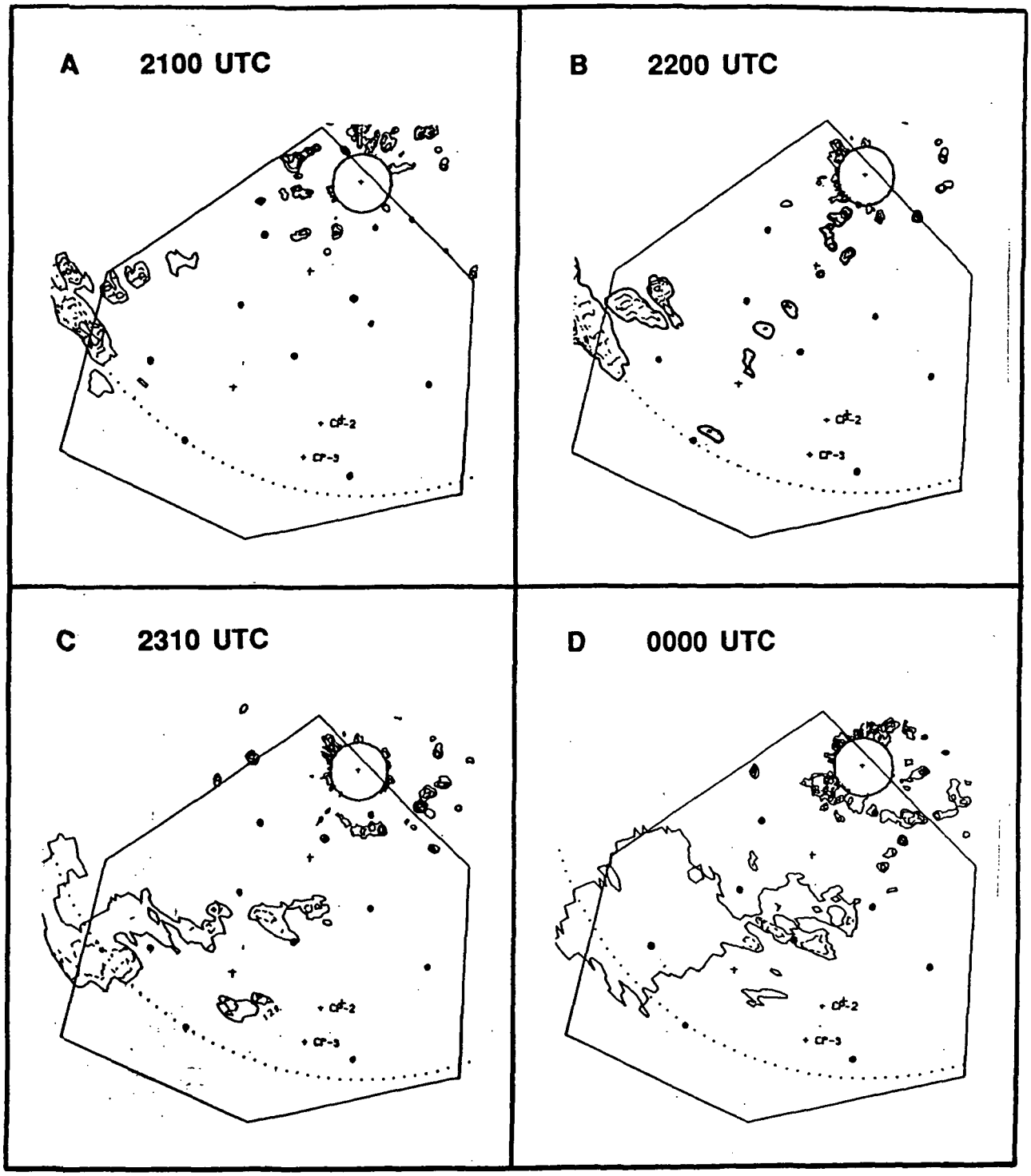

Figure 8: The BNA radar reflectivities (contoured at 18, 30, 38 dBZ) over the COHMEX network at (a) 2100 UTC; (b) 2200 UTC; (c) 2310 UTC and (d) 0000 UTC. Also the dots indicate the PAM stations.

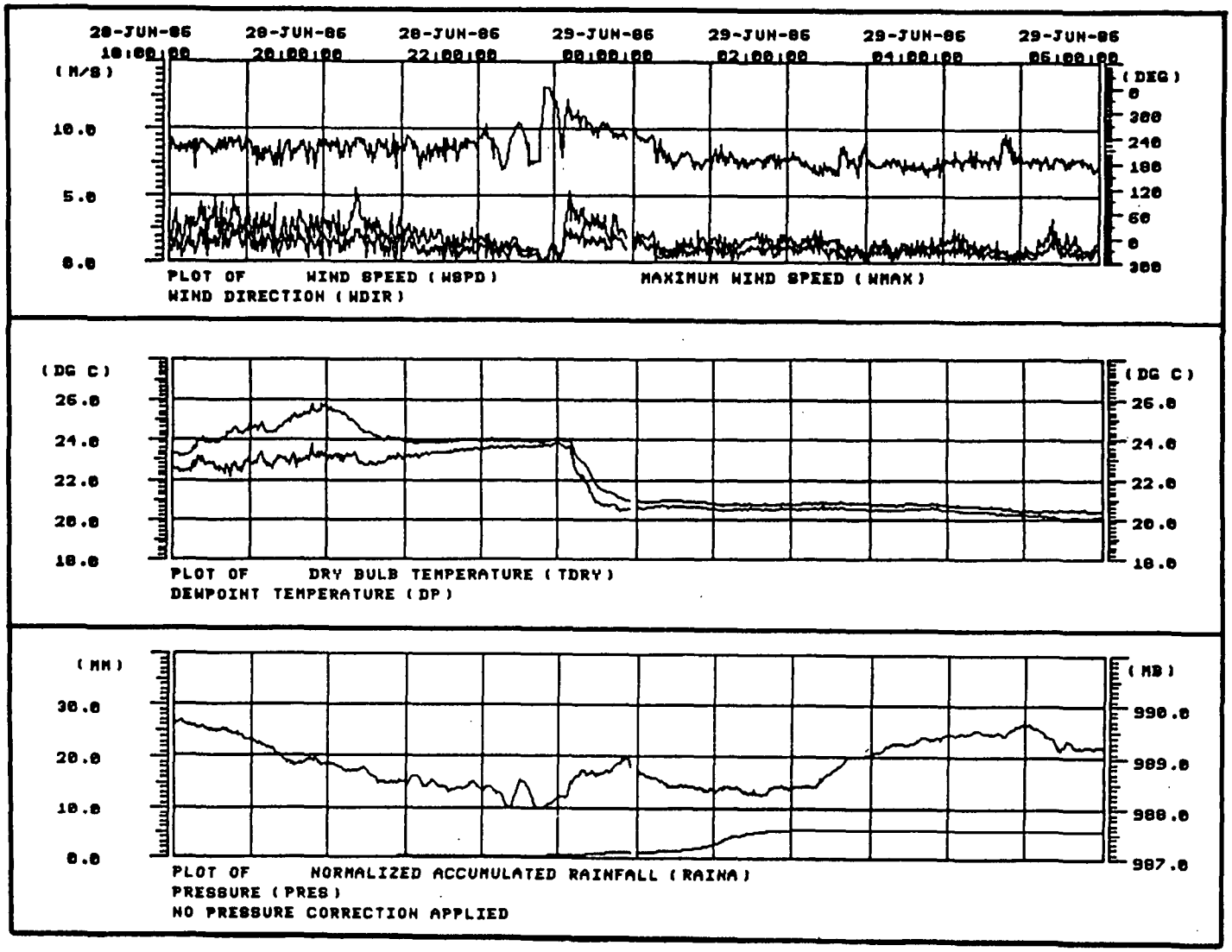

Figure 9a: Time evolutions of the surface PAM observations of wind speed and direction (upper panel), temperature and dew point (middle panel) and rainfall and surface pressure (lower panel), over the 12-hour period from 1800 UTC 28 June to 0600 UTC 29 June, at PAM station #45 (the western-most PAM within the COHMEX network)

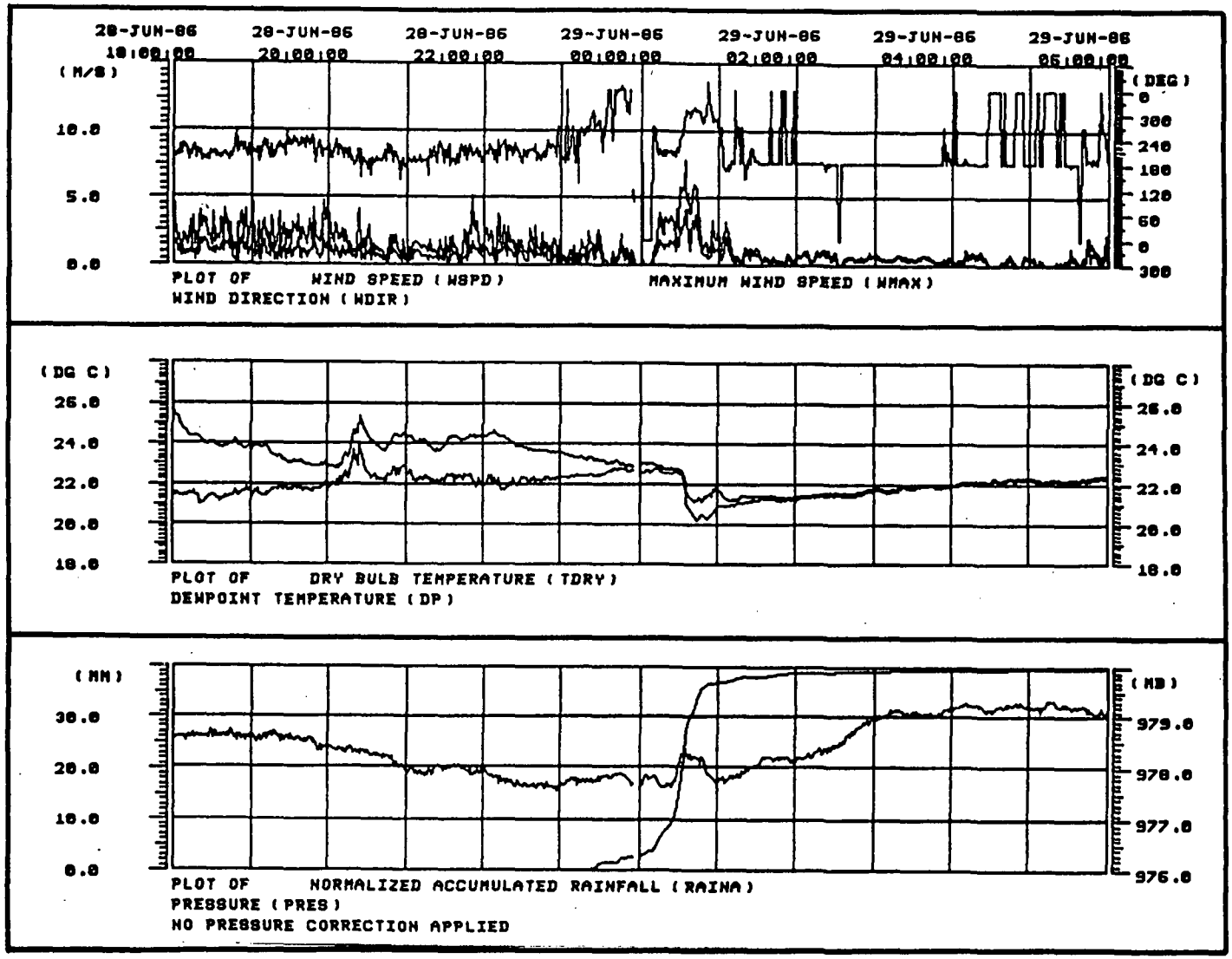

Figure 9b: Same as figure 9b but for PAM station # 46 (center of network).

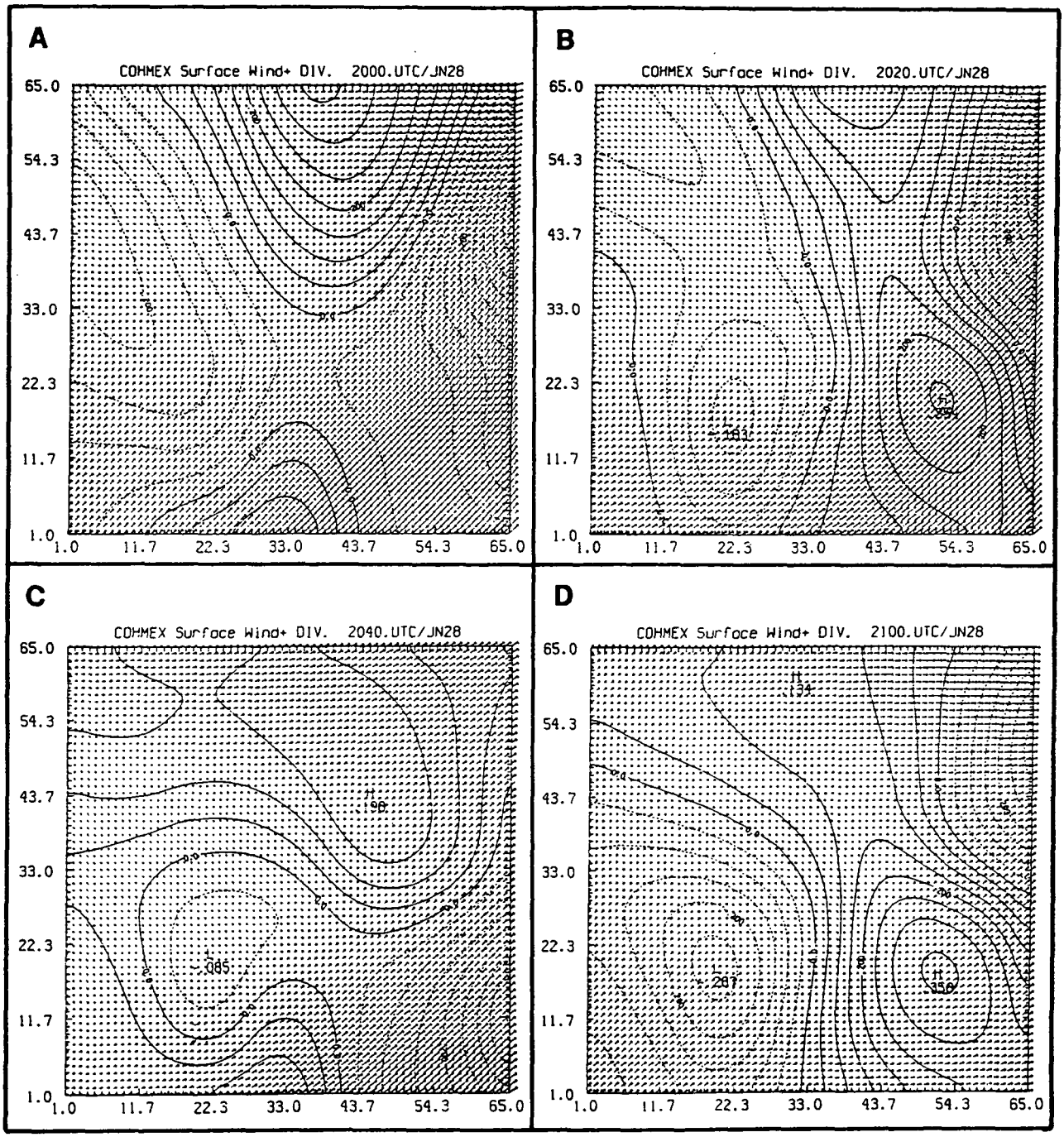

Figure 10: Observed surface wind vector field and the calculated horizontal divergence field (contoured at .05 x 10^{-4} sec^{-1}; negative values dashed) over the square-area just enclosing the 9 PAM stations, at (a) 2000 UTC; (b) 2020 UTC; (c) 2040 UTC; (d) 2100 UTC 28 June.

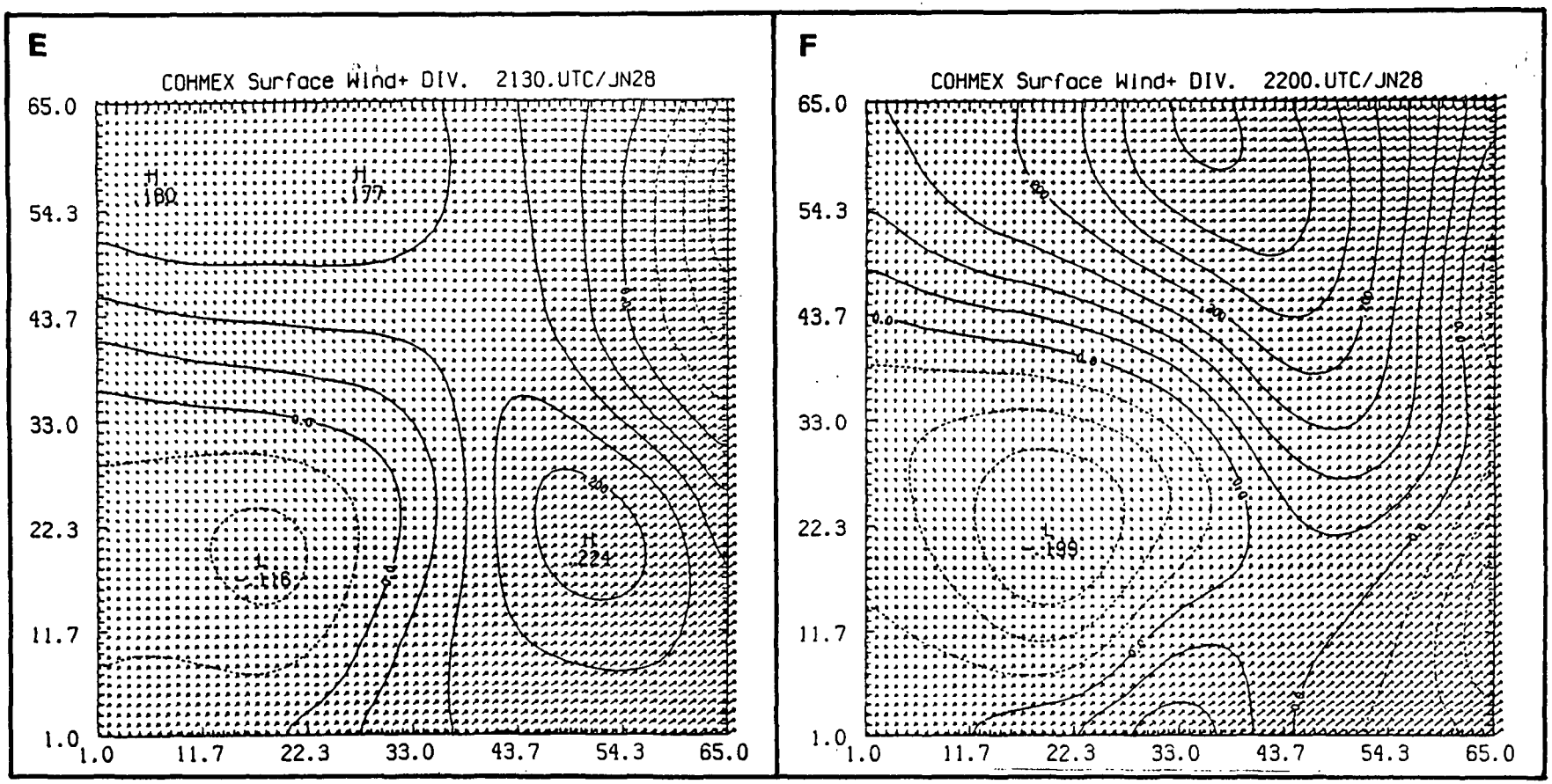

Figure 10 continued: (e) 2130 UTC and (f) 2200 UTC 28 June.

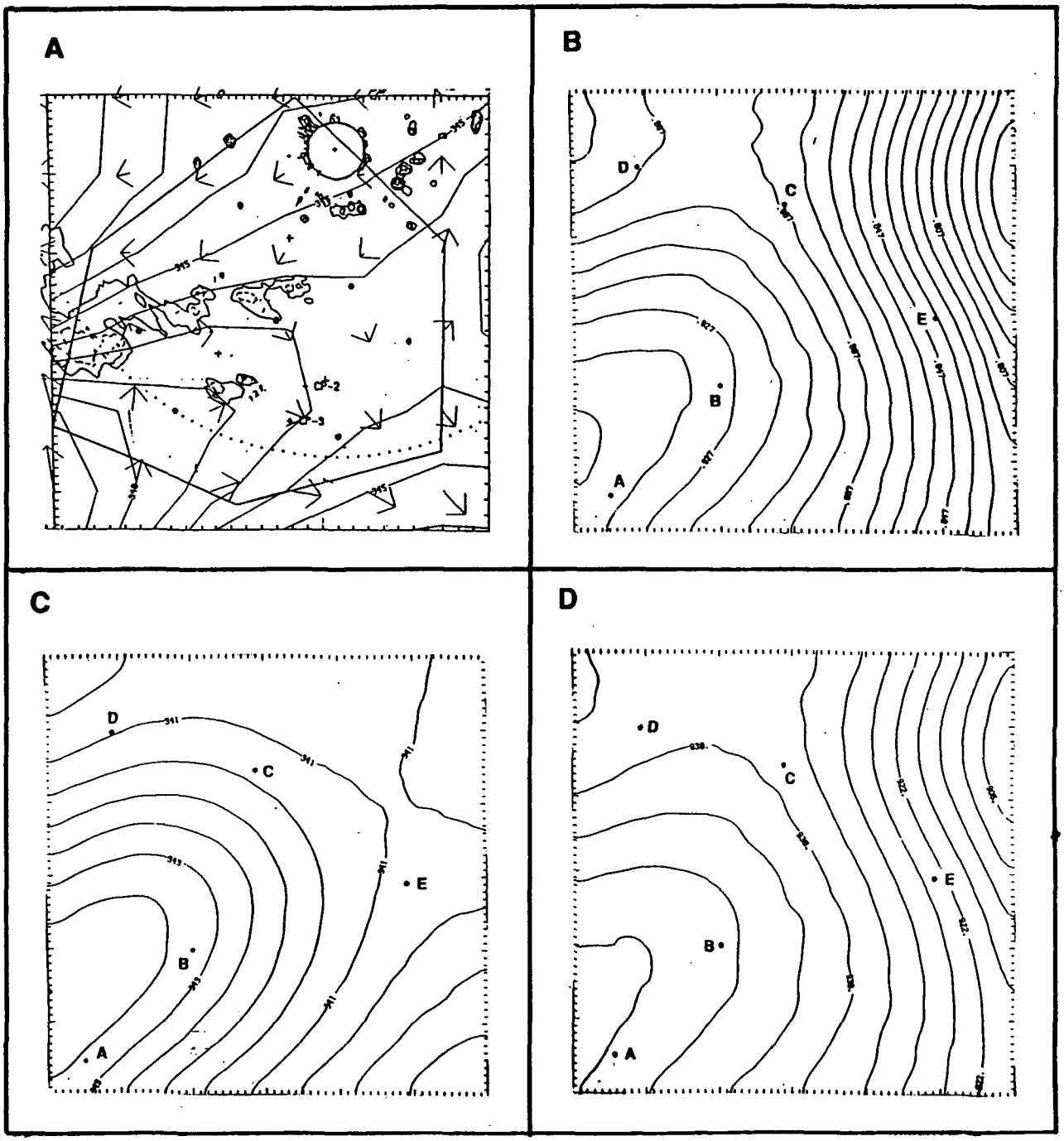

Figure 11: (a) same as figure 6 except for 0000 UTC 29 June, together with the radar data at 2310; (b) observed surface relative humidity field over the square-area just enclosing the PAM stations at 0000 UTC; (c) same as above but for the moist-static-energy field; (d) same as above but for the calculated horizontal distribution of lifting condensation level (mb, contoured at 4 mb).

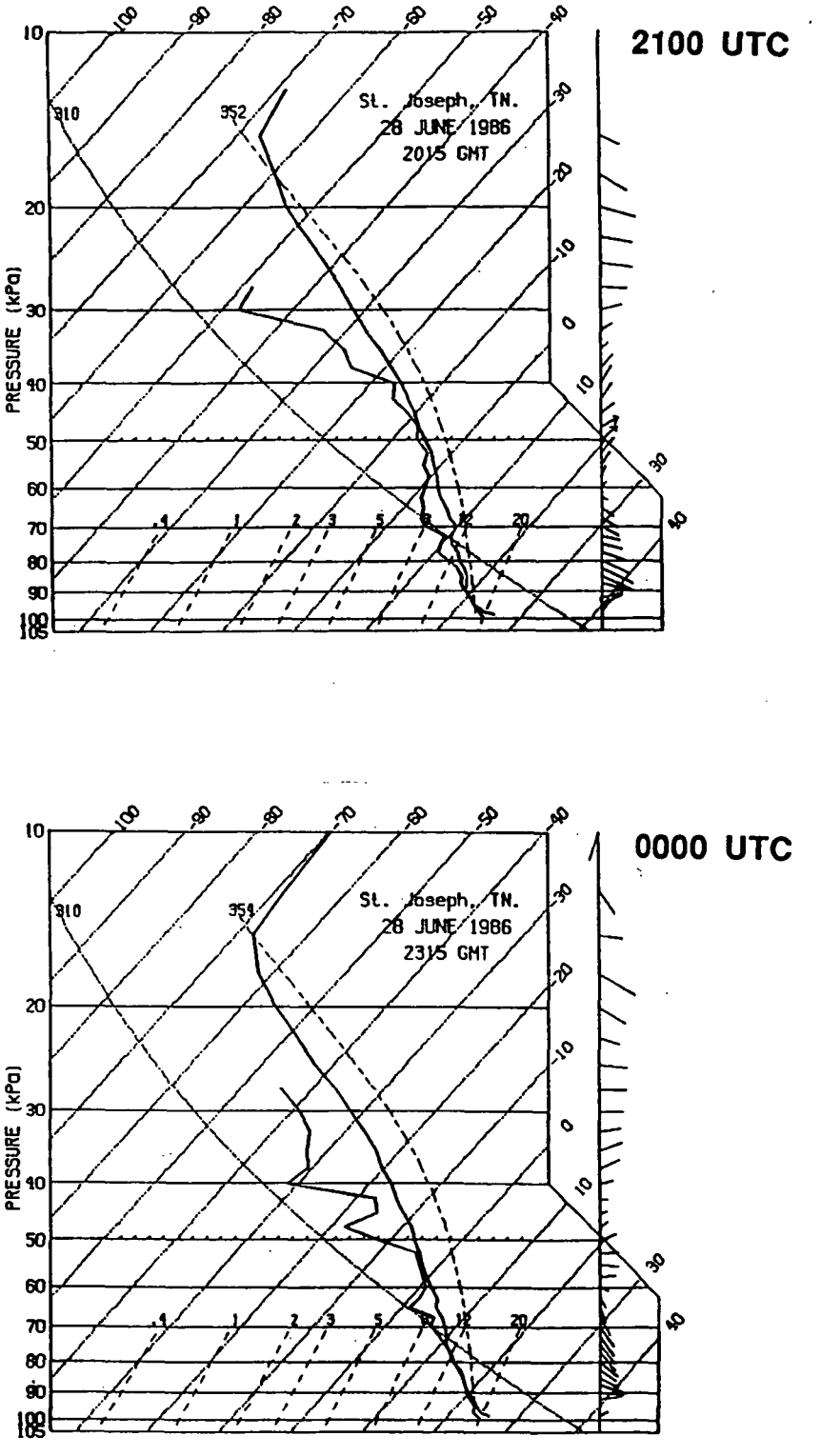

Figure 12: Rawinsonde soundings at St. Joseph, TN, at 2100 UTC and 0000 UTC.

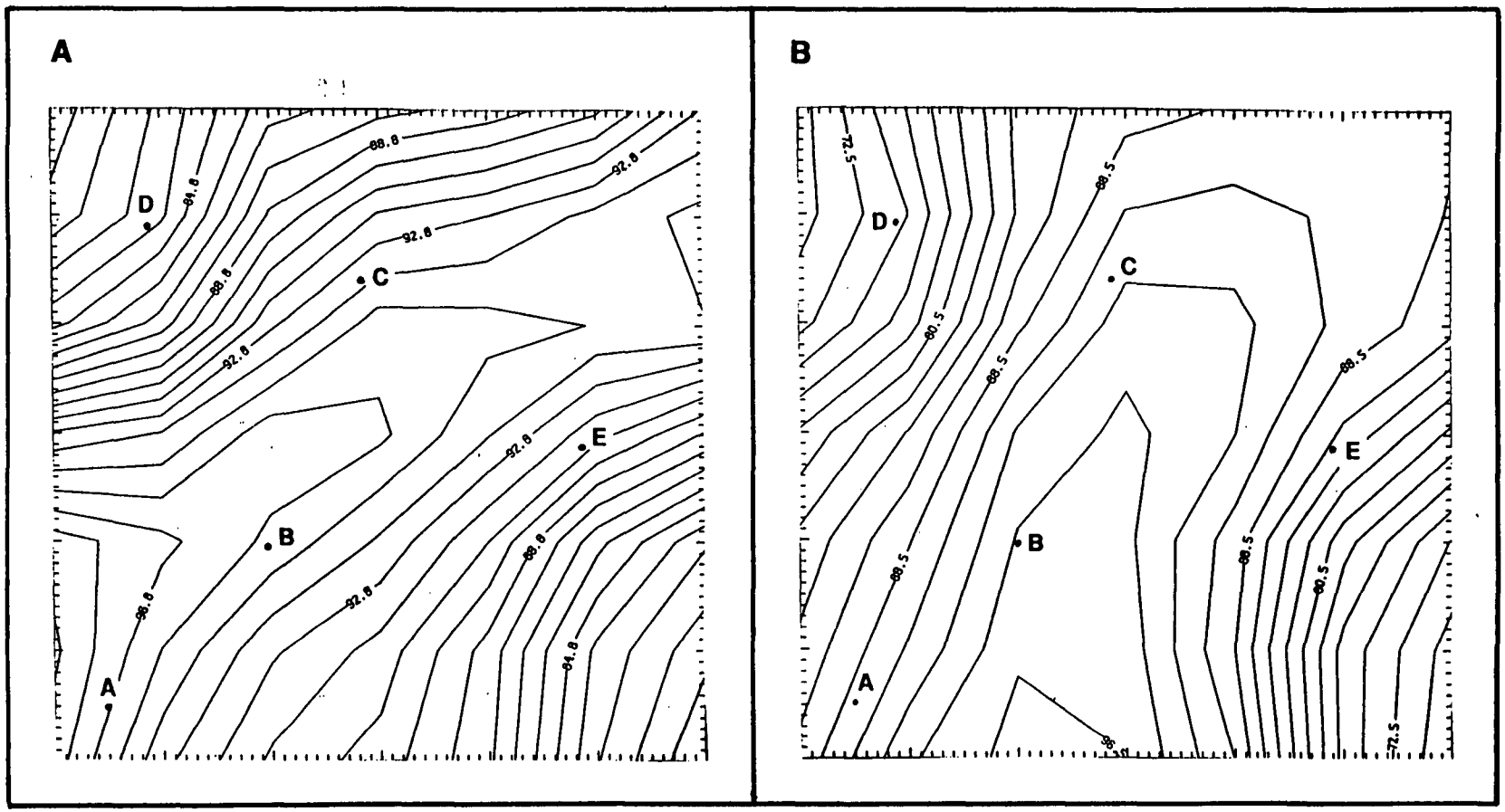

Figure 13: Observed horizontal relative humidity fields of 0000 UTC at (a) 850 mb; and (b) 750 mb, over the square PAM network.

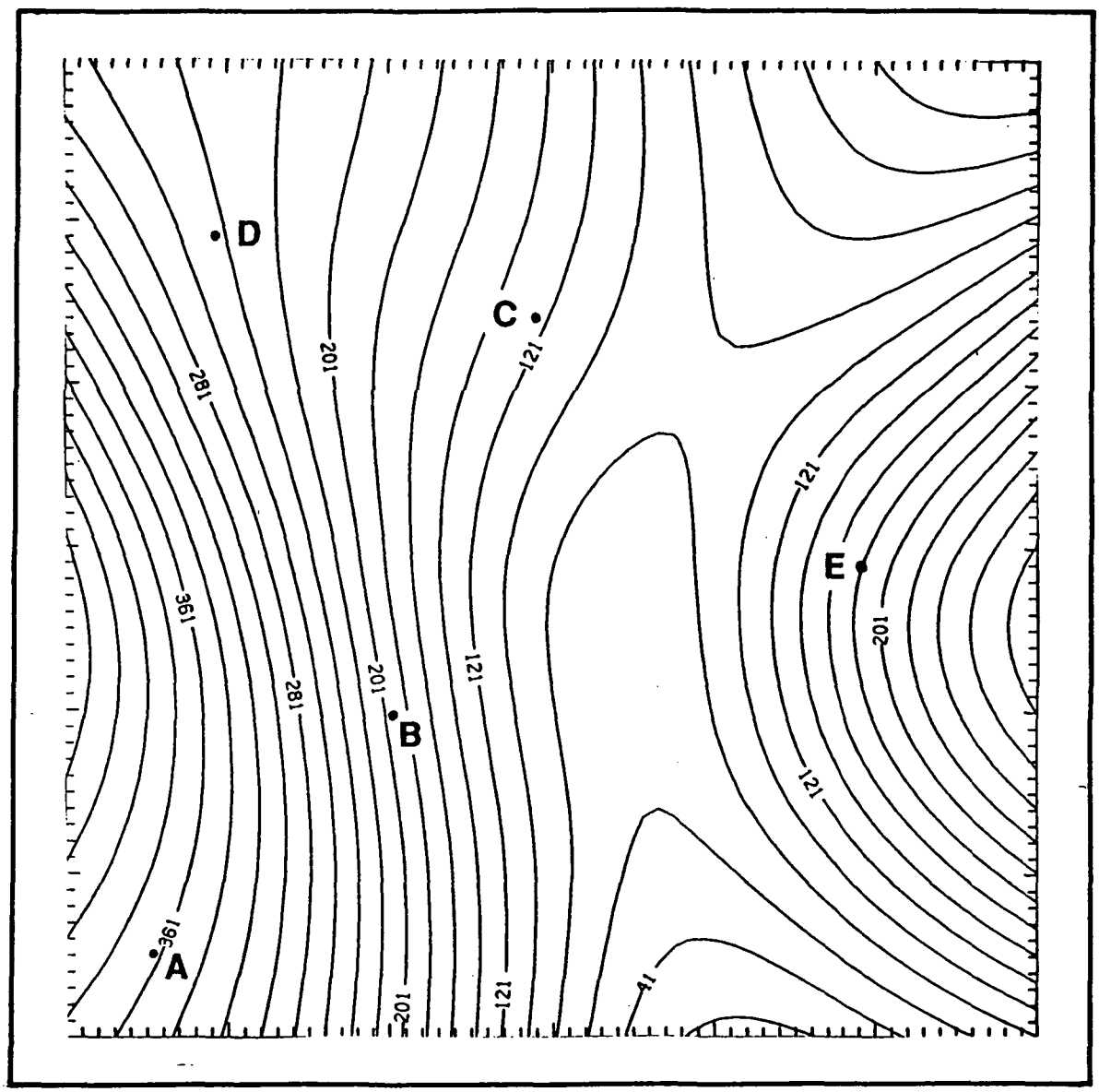

Figure 14: Accumulated surface PAM rainfall distribution over the square PAM network at 2130 UTC (contoured at 0.2 mm; starting time is 0000 UTC 28 June).

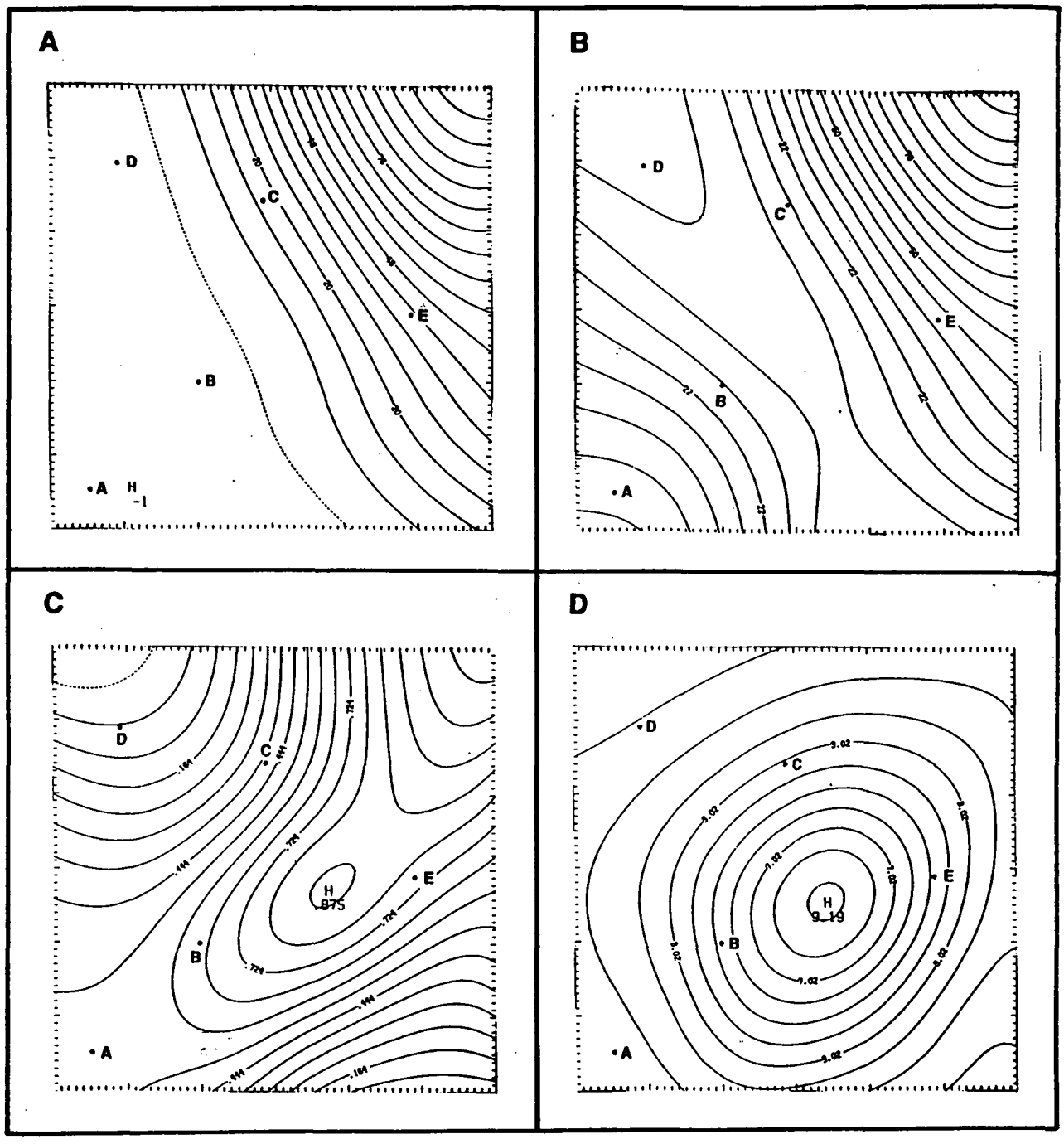

Figure 15: Same as figure 14 but for the newly recorded rainfall during the period of (a) 2130-2230 UTC; (b) 2130-2300 UTC; (c) 2130-2330 UTC; (d) 2130-0030 UTC.

3. 3D-Initialized Convectively Explicit Simulation

3.1 Data and Numerical Model

The COHMEX meso-β scale network, depicted earlier in Figure 1, is composed of 9 rawinsonde stations separated by 100-150 km over an area about 255 km x 255 km, 9 surface PAM stations separated by 50-100 km over an area about 192 km x 192 km, a WSR-57 radar located in Nashville, TN (which is approximately 150 km from the network center), 3 Doppler radars (CP-2, CP-3, CP-4, all located near Huntsville, AL), and other observational platforms (Williams *et al.*,1987). During June 28-29, rawinsonde soundings at 3-hour intervals were released from 1500 UTC to 0300 UTC at the 9 stations, while the PAM data contains standard surface observations at 5-min intervals. Satellite GOES visible and IR images are also available for the area throughout the period.

In order to quantitatively analyze the network pre-convective evolution as well as provide model simulations with observed data, a set of gridded data was established using a Barnes objective analysis scheme together with the 3-hourly rawinsonde observations. At each of the rawinsonde times, three-dimensional gridded data arrays, with a horizontal grid spacing of 0.5 degrees of Latitude, were constructed from the sounding data. The result is a set of three-dimensional "coarse grid" gridded datasets of temperature, relative humidity, geopotential height, and horizontal wind components over the COHMEX network area at 25 mb intervals from the surface to the 50 mb level. These analysis fields are used in some of the pre-convective illustrations (such as in Figure 4). For the numerical simulations, this coarse-grid dataset is converted into a fine-grid dataset using a cubic-spline interpolation scheme. The fine-grid dataset contains the same data fields but with a horizontal grid spacing of 3 km over the square area encompassing the PAM stations (*i.e.* an area of 192 km x 192 km). The model vertical levels are on a stretched grid using the formulation of Wilhelmson and Chen (1973) with a spacing of 200 m near the surface and about 1.5 km near the model top. These fine-grid datasets are used for some of the TCI analysis (such as in Figure 11) and all the numerical simulations. Using the same procedure, the PAM data were analyzed into a fine-grid dataset over exactly the same domain (*i.e.* the 192 km x 192 km domain), which are used as well in some of the observational analyses (such as in Figure 10).

It was noted in section 1 that the purpose of this study is to perform convectively explicit simulations wherein the convection is triggered by the realistic mesoscale three-dimensional winds and thermodynamics and to diagnose the dynamical processes involved in said triggering. Hence, unlike many previous studies, such as Crook and Moncrieff (1988), an observed horizontally-varying three-dimensional dataset unmodified by the use of artificial impulses is employed to

trigger the convection. In an effort to encompass this initial meso-β scale circulation, computer limitations restricted the horizontal resolution to a relatively coarse 3 km. Since it was necessary to define the variations of observed convective initiation over the 192 km x 192 km region, such a relatively coarse resolution was utilized. Accordingly, it is recognized that by using 3 km for the convectively explicit simulations a certain degree of microphysical and turbulence dynamics must be misrepresented or totally lost. Thus, the model outputs to be illustrated in this study should be interpreted with these engineering limitations in mind. Nonetheless, as will be clear through this study, the numerical experiment performed in this study reproduces the qualitative nature of the observed target convective initiation and, therefore, it sheds light on the feasibility of performing convectively explicit simulations which are initialized with realistic three-dimensional observations.

The numerical model used in this study is a convectively explicit model developed by Proctor (1987a,b; 1989). Briefly, the model has 11 prognostic variables: 3 velocity components; the non-hydrostatic pressure perturbation; potential temperature; water vapor and 5 categories of condensate (cloud water, ice particle, rain, snow, and hail). The model prognostic equations are integrated, following Klemp and Wilhelmson (1978) and Cotton and Tripoli (1978), using a time-splitting method treating acoustic waves separately from meteorological waves. Time integrations are done using the Adams-Bashforth scheme. The grid-volume averaging results in quantities which represent subgrid scale Reynolds stresses in the momentum equation and subgrid eddy transports in the rest of prognostic equations. The first-order theory (Clark, 1979) is used for the Reynolds stresses and the eddy transports. A constant-flux layer is defined for the model lowest layer (in this case, the lowest 200 m), in which the nondimensional shear and temperature gradient functions of Businger *et al.* (1971) are used for the surface layer parameterizations. More detailed descriptions of the model can be found in Proctor (1987a).

The model does not include a surface energy budget nor topographic variation. The possible terrain effect in this case cannot be completely ignored, since, for example, there is a small hill in proximity to St. Joseph, Tennessee, which is the closest and the most important station associated with the TCI. However, the resolution used in this study would simply exclude any incorporation of such a microscale terrain effect. On the meso-β scale, there are no major terrain gradients within the COHMEX region (Williams *et al.*, 1987). The absence of energy fluxes across the air-ground interface is considered to produce possible errors in the numerical experiment. Nevertheless, as illustrated previously, the TCI was associated mainly with an existing convergence zone over which the mid-to-lower tropospheric advection of the upstream moisture by the southwesterly flow plays the major role in establishing the environment for convective development. The circulation caused by differential vertical fluxes of surface quantities was not expected to be crucial in convective triggering. The model was initialized with a

warm, buoyant, and unstable boundary layer. Therefore, for such a short period simulation, the lack of surface fluxes is not considered a fatal factor in this study. A model sensitivity test regarding the surface input data is discussed in section 4.

As mentioned previously, the convectively explicit simulations performed in this study are unique because they are triggered by actual three-dimensional fields, as opposed to any artificial impulses. The incorporation of the 3D initial data follows the same rule as used in the "traditional" cloud simulations. That is, a horizontally homogeneous "basic state" is first established using the domain-averaged stratification. Upon this basic state, rather than adding a bubble, a 3D data field (including both winds and thermodynamics) is inserted as the "initial perturbation" at the beginning of the simulation. Thus, the 3D-initialized simulations performed in this study are technically the same as the bubble-initialized simulations (*i.e.* regarding the use of a basic state), except for the form and characteristics of the initial perturbation.

3.2 *Study Goal and Experiment Design*

To actually reproduce all the details of the four-dimensional convective-environmental interactions on the network scale leading to the correct locations/sizes of the observed initial cloud-scale cells is clearly beyond the capability of a 3 km grid simulation with coarse initial data and no variation in surface forcing. Instead, only a small part of the observed convective initiation (during the period from 2130-2330 UTC) is taken as the goal of the numerical simulations of this study. Figures 16a-16c show, respectively, the radar reflectivity maps over a part of the COHMEX network observed by the CP-4 Doppler radar at 2130, 2200 and 2330 UTC 28 June (data edited by Dr. Peter Ray). The three stages of the TCI to be considered as the goal of the numerical simulations performed in this study are schematically shown in Figure 16, namely:

(1) the first cells developed near St. Joseph, or around the network southwest corner, around 2130 UTC (Figure 16a);
(2) cells formed alone a line extending generally NE-SW through St. Joseph by 2200 UTC (Figure 16b);
(3) those cells between St. Joseph and Columbia intensified and developed eastward or southeastward by 2330 UTC Figure 16c).

The peak reflectivities of the first cells were below 20 dBZ (Figure 16a), while they grew to be 30-40 dBZ after about one hour of development (Figure 16b,16c). It is worth noting that the actual "cloud coverage" was much larger horizontally than those shown by the cells in Figure 16. For example, Figure 17 shows the similar reflectivity plots of the CP-4 observation (data obtained from Dr. Kevin Knupp) about at the same time but from a three-dimensional view. It is clear from Figure 17

that the TCI was associated with a rather cloudy environment.

Throughout this study, for the purpose of model output analysis the three-dimensional domain is divided into two layers: a "convective layer" (CL) which is 1-4 km above the surface, and a "boundary layer" (BL) which is 0-2 km. All the horizontal cross-sections to be discussed are composed of model output quantities which are mass-weighted averages within either the CL or the BL. The CL is chosen because the model produced peak reflectivities are always within this layer, and because the heights of the top and bottom of the CL are consistent with those observed by the CP-4 Doppler radar (which were 2-3 km above the surface, as diagnosed by Dr. Kevin Knupp). The BL is chosen simply because within this layer the surface thermally-produced dry turbulent motions are likely to dominate energetically over the latent heating processes during the first 20 minutes or so. Therefore, a turbulent kinetic energy (TKE) budget analysis (Stull, 1988) is performed only for this layer. Likewise, the TKE budget components are probably meaningful only during the first 20 minutes of the simulations. After that, latent heating dominates in the simulations of this study.

More detailed time evolution of the model fields are illustrated using 5-minute model time series at five selected grid points whose locations are indicated in Figure 11b (which hereafter are referred to as point A, B, etc.). The five points are selected such that points A and B are within the initial convectively favorable zone (*i.e.* the southwest corner), while points A, B and C are approximately along the line of the initial cells illustrated previously (*i.e.* the NE-SW line). Points D and E are within the initially less-favorable zones, being upstream and downstream, respectively, relative to the flow across the trough axis.

3.3 *Control Simulation*

Throughout this study, the control simulation refers to the 1-hour three-dimensional convectively explicit simulation which is initialized with the three-dimensional gridded rawinsonde data valid at 0000 UTC. In this subsection, the model results of the control simulation are illustrated using (a) 5-minute time series of selected model quantities (within the BL or the CL) at the five chosen points; (b) vertical distributions of equivalent potential temperatures at 20-minutes interval at the five points; and (c) horizontal cross-sections within the CL over the entire model domain.

3.4 *Time Evolution of Key Variables*

Figure 18a shows the time variability of equivalent potential temperature (q_e) at the five chosen points, as calculated following the procedure of Bolton (1980). It is clearly seen that points A and B are initially thermodynamically more favored than the other points, namely their surface q_e values are initially 2-3 K higher than those

at points C, D and E. During the 50 minute period as shown in Figure 18a, convective consumption (*i.e.* surface thermodynamic energy depletion due to convective overturning) produced the general decreases of the q_e values. It is important to note that, although there seem to be different rates of convective consumption, points A and B seem to be able to remain as the thermodynamically most favored points throughout the simulation according to the surface q_e values. The persistence of this spatial pattern of convective potential indicates the contribution to the TCI by the pre-convective mesoscale hydrostatic circulations over the COHMEX network area. This contribution will be further discussed throughout the rest of this study.

Figure 18b shows similar time curves as Figure 18a but for the buoyancy production terms of the TKE budget within the BL (the shear production terms and the other TKE budget components are at least an order of magnitude smaller, therefore are not shown). It is seen that due to the pre-convective destabilization pattern, spatially-varying turbulent-plume intensities are expected to be generated at the five points due to the different buoyancies of the plumes. It is also noted that stronger TKE is developed first at point A and then at point B, thereby implying a tendency of developing toward the northeast direction. This tendency will be discussed in detail in subsequent sections.

The plume vertical velocities within the BL are shown in Figure 18c. It is seen that the peaks of the vertical velocities at points A and B correspond well with the peaks of the buoyancy production terms of TKE shown in Figure 18b, thus indicating the origin of these plumes. It is noted that the TKE quantities are probably meaningful only during the first 20 minutes, due to the dry-process assumption inherent to the TKE budget equation.

In order for the boundary layer dry plumes to become clouds, not only condensation must occur but also the negative buoyancies of the plumes near the condensation levels must be overcome such that "updrafts" could rise freely. Figure 18d and 18e show, respectively, the temperature-excess terms at the LCLs and the LCL heights (in mb), both obtained using the formulations of Bolton (1980). It is clearly seen that the negative buoyancies are in the range of -0.5 to -2.0°C. The corresponding LCLs, which vary slowly with time, are all below the height of the 920 mb level during the first 20 minutes at the five points. For example, point A has a surface pressure (not shown) of 995 mb, and LCL pressures in the first 20 minutes of 930-950 mb. Therefore, surface air in proximity to point A generally needs to rise only a few hundred meters to reach condensation. Accordingly, the fact that the LCLs are well within the BL indicates that "moist plumes", as opposed to dry plumes, should dominate the upper-BL and the entire CL after the first 20 minutes.

Figure 18f clearly indicates that the model total condensate at point A, for instance, has reached a magnitude such that reflectivity values of 20 dBZ develop at 20 minutes, and continues to increase until around 30 minutes of simulation. The

aforementioned tendency of developing toward the northeast is seen by the fact that the sequence of reaching the peak reflectivities is: first point A; then point B; then point C. Point D shows essentially no condensate is produced within the CL, while point E developed weak convection even though it is not initially a favored point.

Once latent heating starts, the growth of the moist plumes is strengthened resulting in initial convective updrafts which grow beyond the turbulent boundary layer. At this stage, the extent to which an initial updraft can grow is determined generally by two constraints: a static constraint of enough CAPE, and a dynamic constraint of enough vertical velocity. Figures 18g, 18h and 18i show, respectively, the CAPEs, buoyancies within the CL and the vertical velocities within the CL, at the five points. It is clearly seen that points A and B are supported by the largest CAPEs throughout the simulation period. The vertical velocities and the buoyancies do not show the same pattern over the entire period, but nevertheless show that point B develops with a time lag after the point A development.

3.5 *Vertical Profiles*

Figure 19a shows the vertical profiles of q_e at point A at the 3 selected model times (0, 20, and 40 minutes). Only the lowest 10 km of model vertical domain (which extends to 18 km) is used here for showing the most important q_e changes. It is seen that during the first 20 minutes, convective overturning results in a decrease of q_e in the lowest 2 km and an increase of q_e in the layer between 2 and 6 km. After the first 20 minutes, the convective development in the vicinity of point A diminishes. This is indicated in Figure 18f by the termination of the rapid rise in model reflectivity after the first 20 minutes of the simulation. On the other hand, Figure 19b shows clearly that the point B convection continues to grow even during the second 20-minute period. Similarly, Figure 19c shows that the point C convection continues to grow as well during the period of 20-40 minutes, only to a lesser degree as compared with the point B development. Therefore, the tendency of developing toward the northeast is further seen from these figures. Figure 19d shows that negligible convection is found at point D, while Figure 19e shows that weaker and shallower convection has developed at point E as compared with those at points A, B and C.

3.6 *Horizontal Distribution*

Figure 20a shows the horizontal distribution of buoyancy field within the CL at 20 minutes of simulation. It is seen that the pre-convective thermodynamic pattern, previously shown in Figure 11, is identifiable from the model buoyancy field at the end of the first 20 minutes. That is, the southwest corner persistently appears to be the most favored zone for convective development, whether viewed from the initial thermodynamic pattern near the surface or from the horizontal

distribution of buoyancy within the CL 20 minutes later. Therefore, it is confirmed that on the domain scale the convective development is largely determined by the pre-convective thermodynamic pattern near the surface.

On the finer scales, however, Figure 20b shows that the buoyancy distribution does not seem to be able to "predict" the resultant much wider spectrum of scales of motion, even though in this case the buoyancy term is the most important forcing component generating vertical velocities. The vertical motion field shown in Figure 20b is composed of either relatively stronger "cores" of updrafts or downdrafts with speeds of 30-40 cm s^{-1}, or weaker motions of approximately 10 cm s^{-1} or less covering a large fraction of the domain. The scales of the most developed updrafts or downdrafts within the southwest corner area appear to be in the range of 10 km x 10 km to 15 km x 15 km. Although not based on the same physical details, Redelsperger and Clark (1989), in their two-dimensional simulation, found the dominant deep mode in the wet simulations (*i.e.* water cycles included) appear to be with scales of 10-16.7 km. The main difference between the physical background of their study and this study may well be that the domain of this study is dominated by the buoyancy distribution resulting from the pre-convective mesoscale circulations. However, the question of why some scales appear to be more favored than other scales does not seem to be clearly answered in either study. Schlesinger (1982) noted: "It is not clear whether the horizontal scale of real thunderstorm cells is determined by 'mesoscale' distributions 50-100 km in length or by a much narrower 'cloud-scale' forcing region such as a 'bubble', or maybe by aggregates of yet narrower thermals.". From the results of this study, it seems that an initial environmental forcing of 50-100 km (*i.e.* the southwest corner, or the band of moistening) appears to interact non-linearly with the convective processes such as to produce the relatively dominant scales of 10-15 km across. However, it is clear that higher observational and numerical resolutions, in both spatial and temporal domains, are required to fully address the question raised by Schlesinger.

As in Figure 20, Figure 21a and 21b show the buoyancy and the vertical motion fields, respectively, at 40 minutes. It is seen that the domain-scale convective development basically remains the same. On the smaller-scale area near the southwest corner, Figure 21b shows that the vertical motion field becomes more "organized" with an apparent scale of 50 km x 50 km (as opposed to the 10-15 km scale 20 minutes earlier). On the other hand, the rest of the domain becomes "noisier" with stronger but horizontally less-organized upward or downward motions covering a large fraction of the domain. It is worth noting that because the latent heating processes dominate the second 20-minute period and beyond, the model reflectivity field, as opposed to the vertical motion field, may become a better choice regarding the verification of the model.

3.7 *Control Simulation Verification*

To briefly summarize the control simulation, a comparison among the convective development at points A, B and C as shown in Figures 18f and 19a-c, together with 20b and 21b, describes the following scenario:

(1) Due to the favorable environment created by the pre-convective mesoscale destabilization, point A develops the earliest convection, in the form of lower-tropospheric plumes which "root" within the turbulent boundary layer but with significant upper fractions being associated with latent heat release;

(2) Point B, and then point C, develop convection of comparable intensities but at later times. Since these three points are aligned SSW-to-NNE, the time lags imply the existence of a tendency similar to the observed. However, this model-produced tendency does not seem to result in a "linear" form of convective cells, as viewed from the model vertical motion field alone (rather, a continuous organization is found for only the developments near the southwest corner).

In order to verify the model results, the model generated reflectivity and horizontal wind fields within the CL are superimposed on the radar reflectivity of 2200 UTC. Figures 22a through 22c show, respectively, the model results at 20, 35 and 50 minutes. Before discussing the verification, however, it should be noted that, due to the likely data resolution problem, the rainfall observation by the PAM stations does not match with those by the radar. For instance, according to the analyzed PAM rainfall data the network center had no rainfall until as late as 2300 UTC, while the cloud-scale cells detected by radar already indicate reflectivities up to 30 dBZ at a time of almost an hour earlier. Because all simulations performed in this study are only one-hour long, it is clear, therefore, that any model quantitative verification on the cloud-scale is practically impossible. Nevertheless, a qualitative verification on the meso-β scale (*i.e.* 50 km x 50 km to domain size) could be carried out and which is described below:

(1) Figure 22a shows the earliest model convection is around the southwest corner, which is consistent with the observed (Figure 16a);
(2) Figure 22b shows the model convection tends to develop toward the northeast, which is consistent with the observed (Figure 16b);
(3) A careful comparison between Figures 22c with 22b indicates that the

"band" of the model convection strengthens itself relatively more over its northern portion than its southern portion during the model time of 35-50 minutes. For example, the area just halfway between St. Joseph and Columbia shows model reflectivities of only 10 dBZ in Figure 22b, but nearly 20 dBZ in Figure 22c, while during the same time the southwest corner shows model reflectivities of 30-35 dBZ without any significant increases. Therefore, on one hand the model does produce a "differential" convective development along the NE-SW band, which is consistent with the observed (Figure 16c). On the other hand, however, the southwest corner model convection remains strong and organized after one hour of development, which is not observed.

The reason for the model's inability to replace the spatially maximum convection from the southwest corner to near the network center, as observed, is likely a direct result of the pre-convective thermodynamic pattern (*i.e.* through a CISK-like self-enhancing mechanism associated with a positive feedback process initiated by the earliest latent heating around the southwest corner). The high humidity condition throughout the lower troposphere likely reduces the downdraft cooling effect near the surface, thereby reducing the convective stabilization on the surface. In the situation with a strong environmental wind field and/or strong shears, there could be a dramatically different process of convective organization. However, as will be illustrated later in this study, the three-dimensional environmental wind field in this case seems to be able to produce only minor effects upon the convective organization.

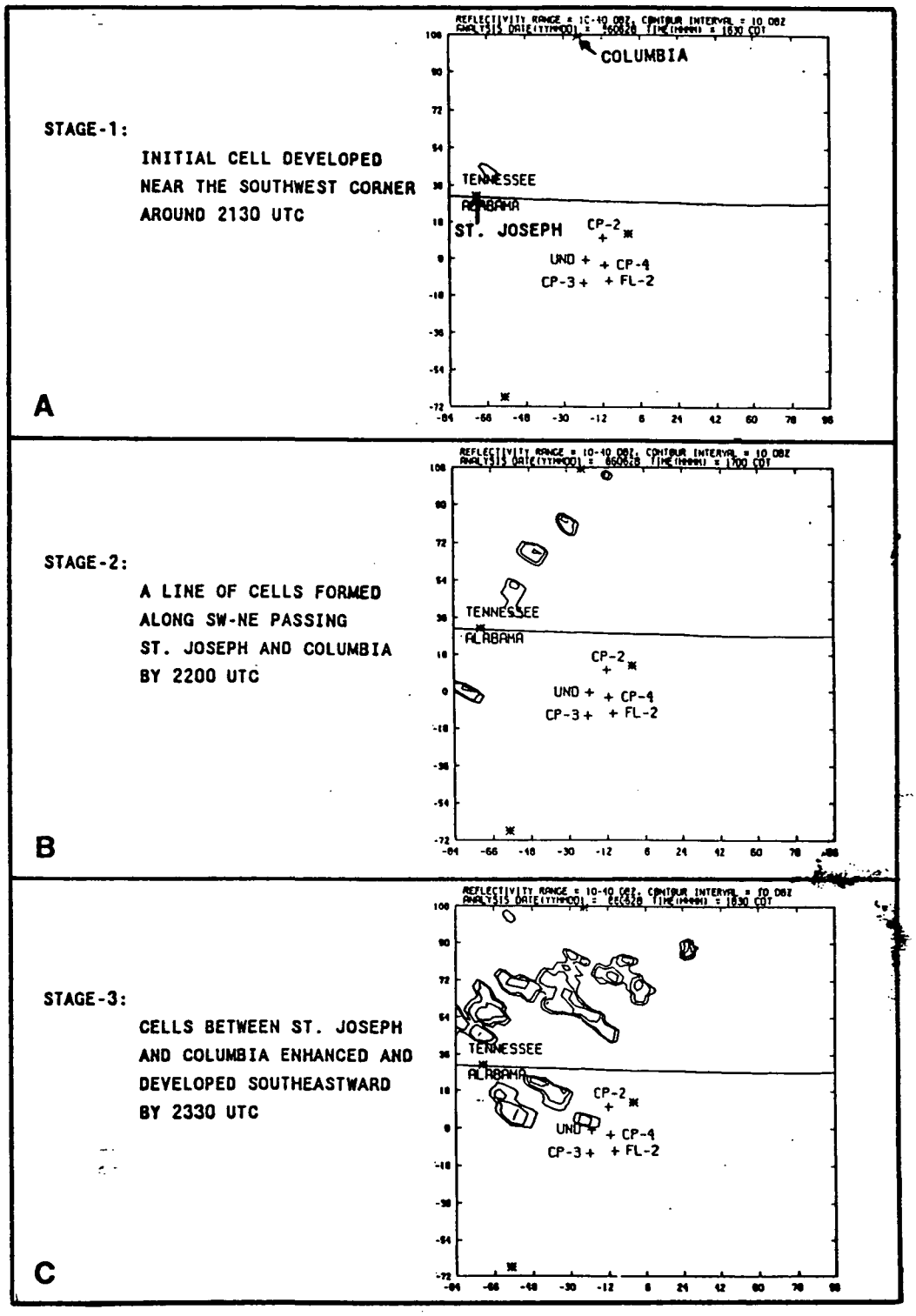

Figure 16: Observed radar reflectivity fields by the CP-4 doppler radar, which is located (as shown) near Huntsville, AL, looking toward the northwest, at (a) 2130 UTC; (b) 2200 UTC and (c) 2330 UTC. The 3-stage convective development as outlined in this figure is denoted as the target convective initiation (TCI), which serves as the goal of the numerical simulations performed in this study.

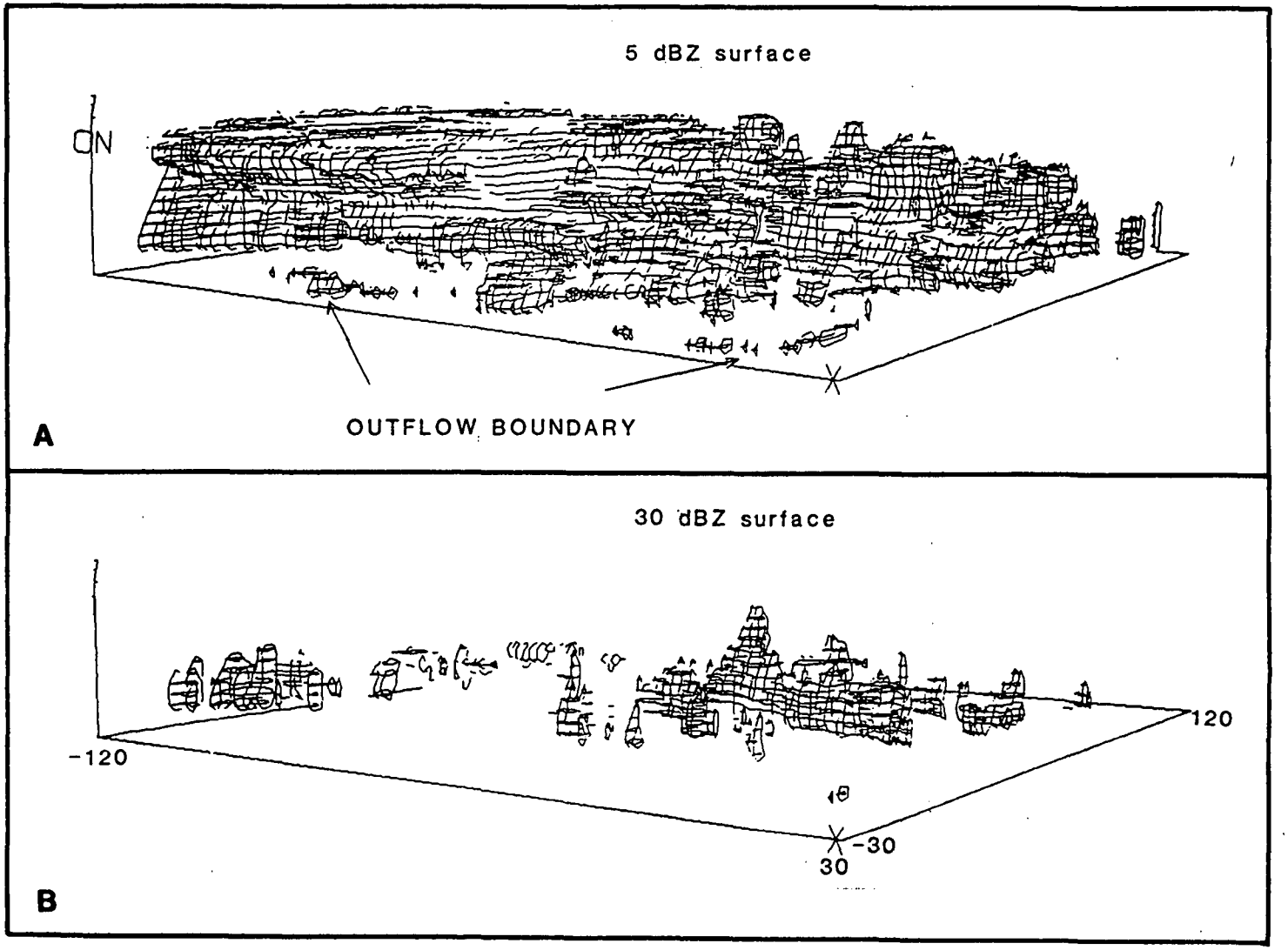

Figure 17: Three-dimensional plots of the observed reflectivities by the CP-4 doppler radar (looking toward the northwest from CP-4, which is denoted by "X") at 0000 UTC, at the starting contour value of (a) 5 dBZ, and (b) 30 dBZ.

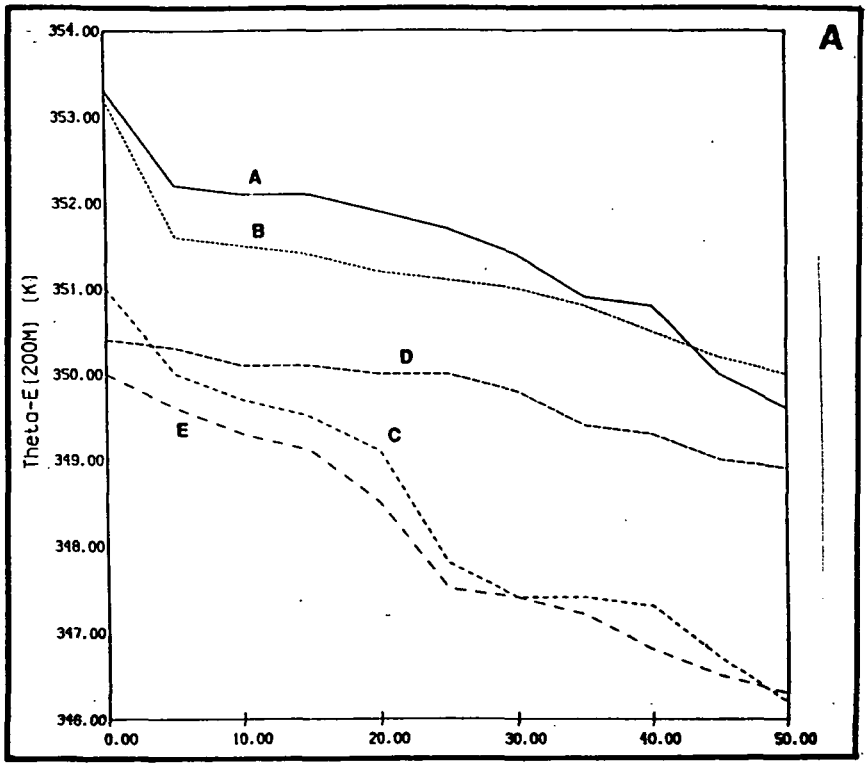

Figure 18a: Time evolutions of the equivalent potential temperatures, calculated using the model lowest level data of the control simulation, at the 5 chosen grid points (whose locations are indicated in figure 11b). Abscissa indicates the model execution time in minutes.

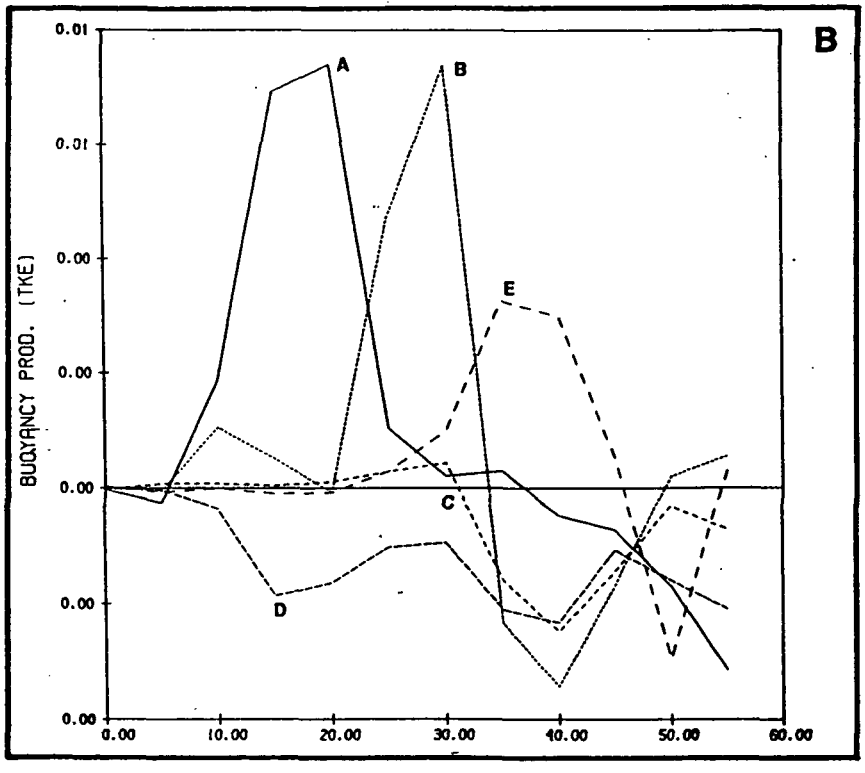

Figure 18b: Time evolutions of the buoyant production terms, which are shown as mass-weighted averages within the lowest 2 km at each of the 5 chosen points.

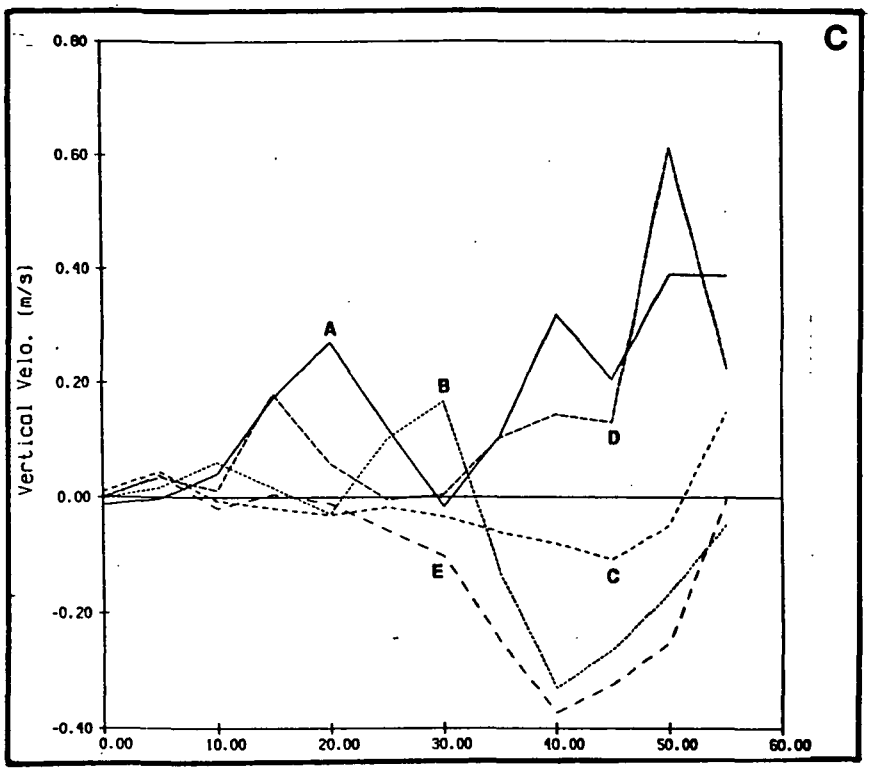

Figure 18c: Same as figure 18b but for the vertical velocities.

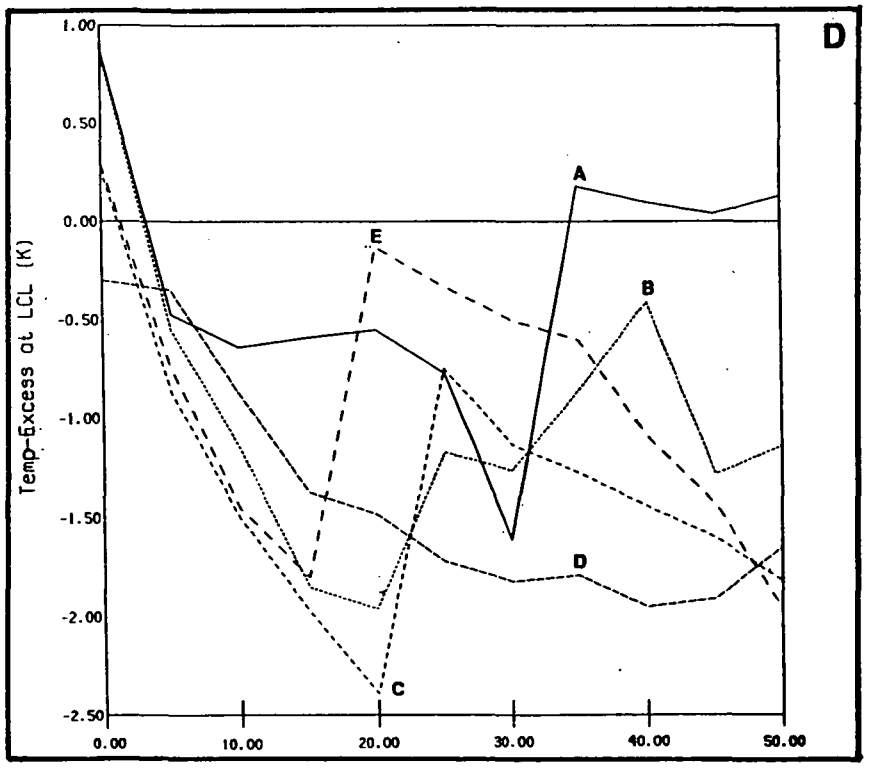

Figure 18d: Same as figure 18a but for the temperature excess values at the lifting condensation levels.

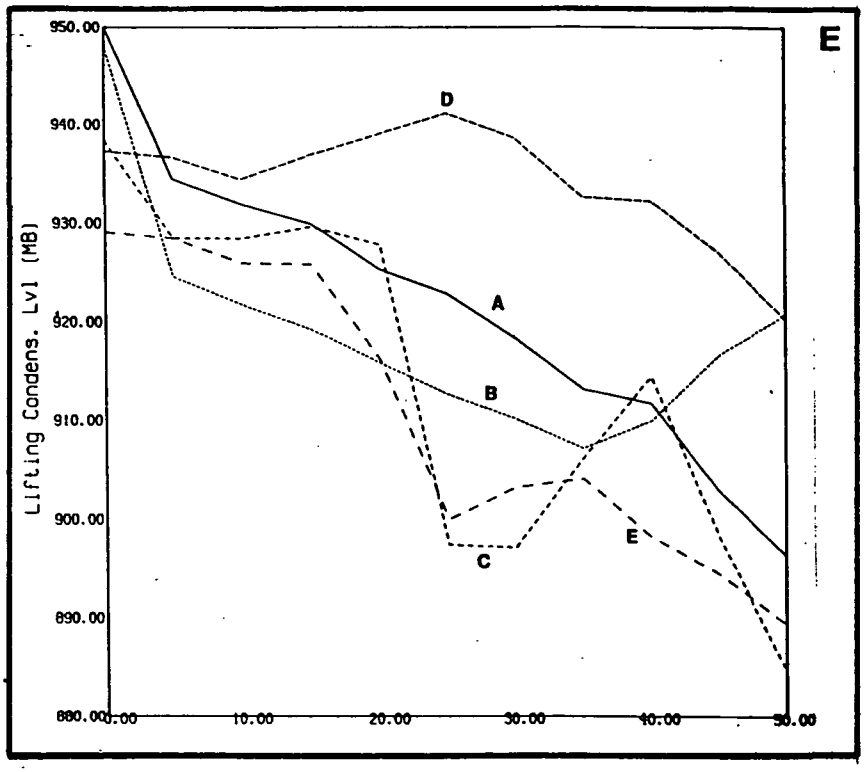

Figure 18e: Same as figure 18a but for the lifting condensation levels (mb).

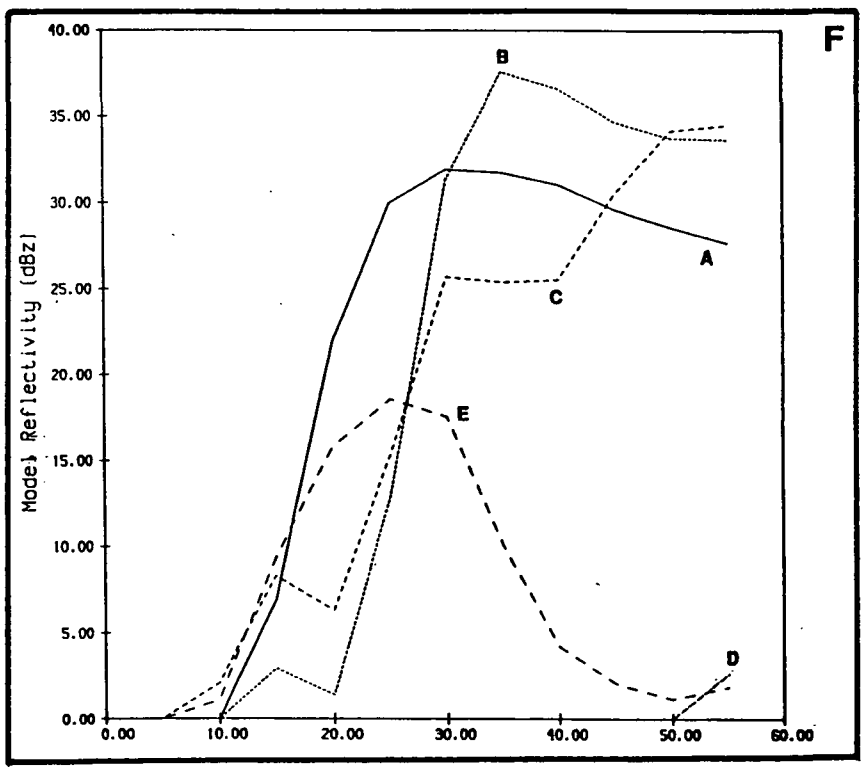

Figure 18f: Same as figure 18b but for the model reflectivities (dBZ).

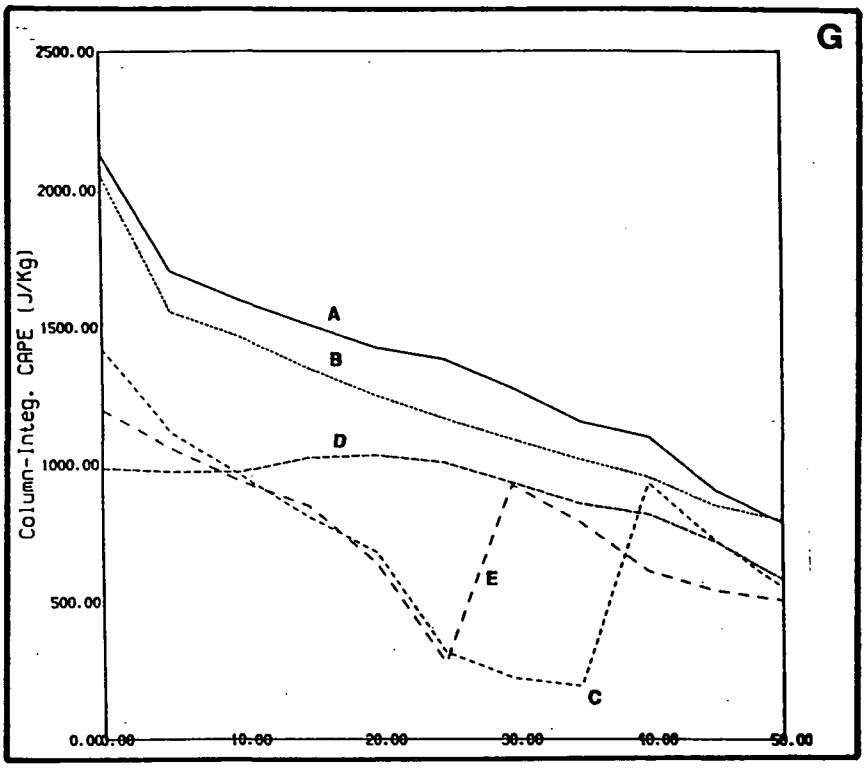

Figure 18g: Same as figure 18a but for the convectively available potential energies.

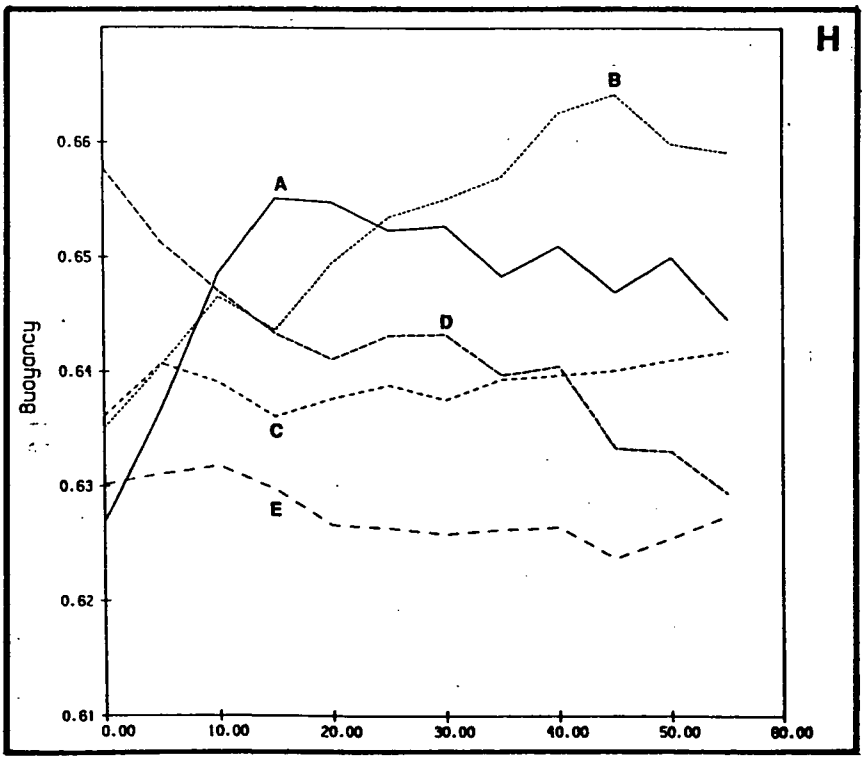

Figure 18h: Time evolutions of the buoyancy terms, which are shown as mass-weighted averages within the model layer between 1 km and 4 km, at the 5 chosen points.

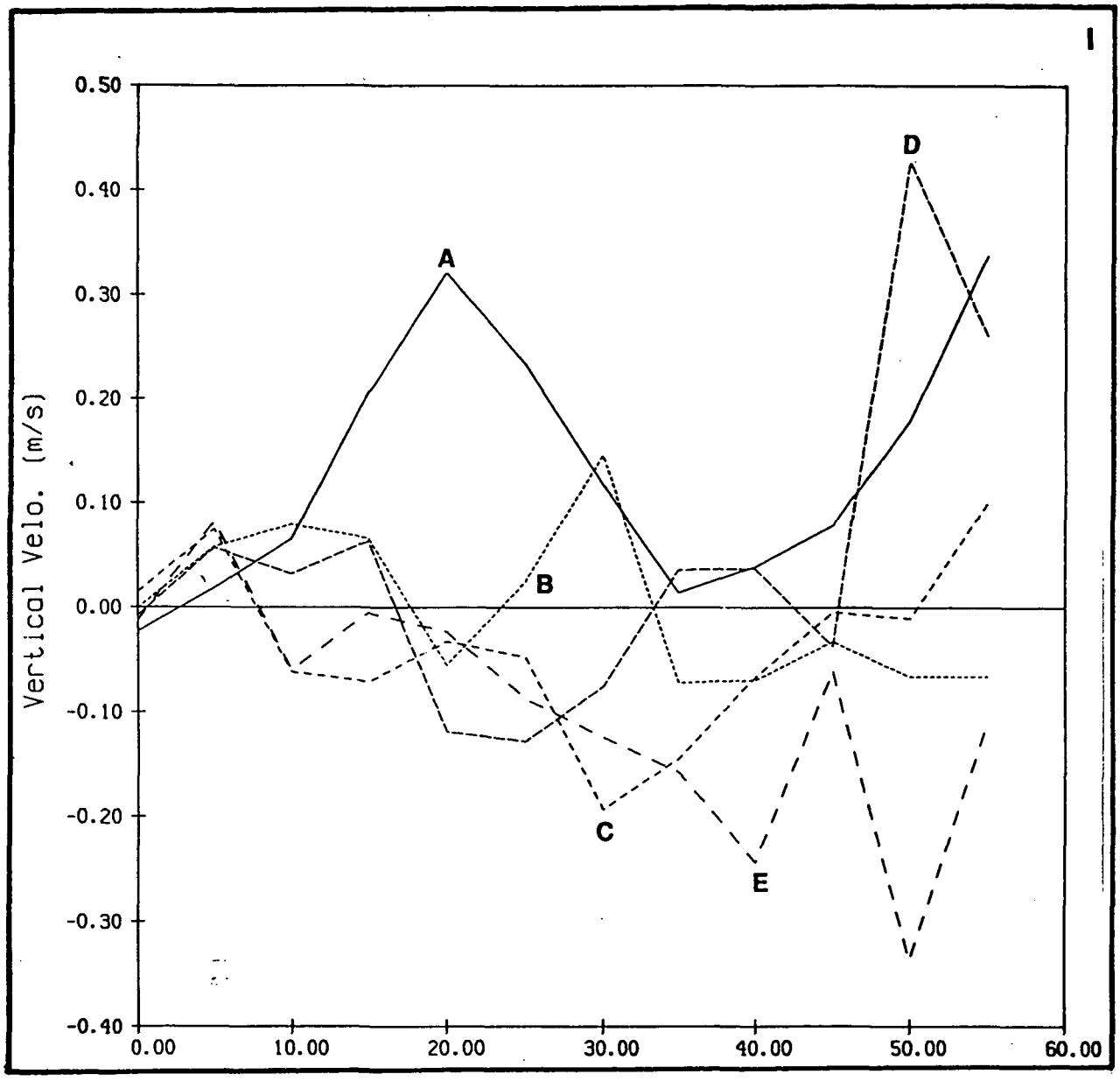

Figure 18i: Same as figure 18h but for the vertical velocities.

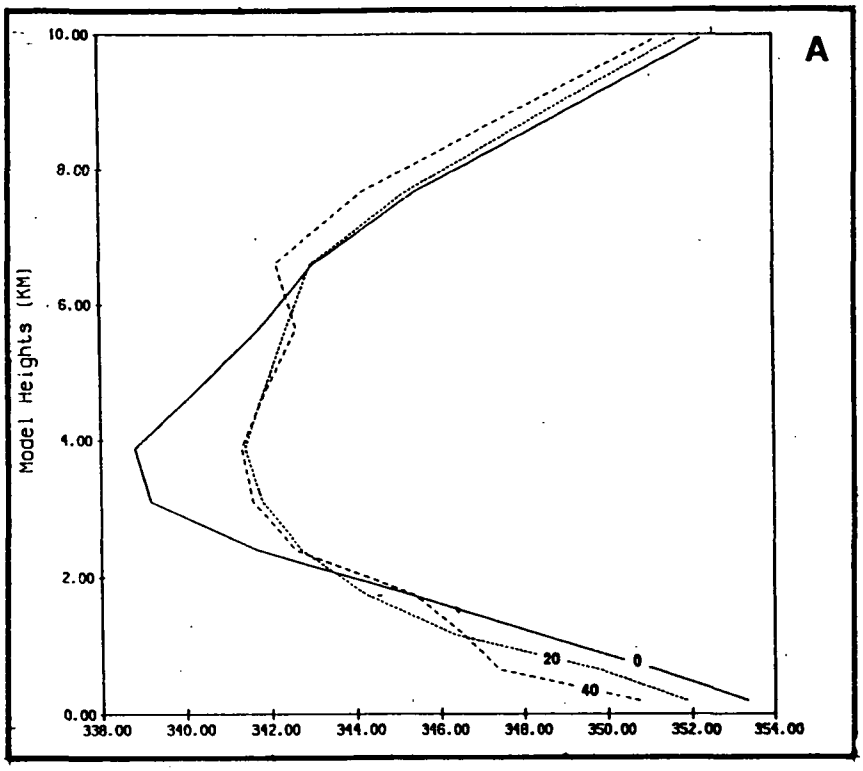

Figure 19a: Vertical profiles within the lowest 10 km of model domain of the model equivalent potential temperatures at point-A at 0, 20, and 40 minutes of the control simulation.

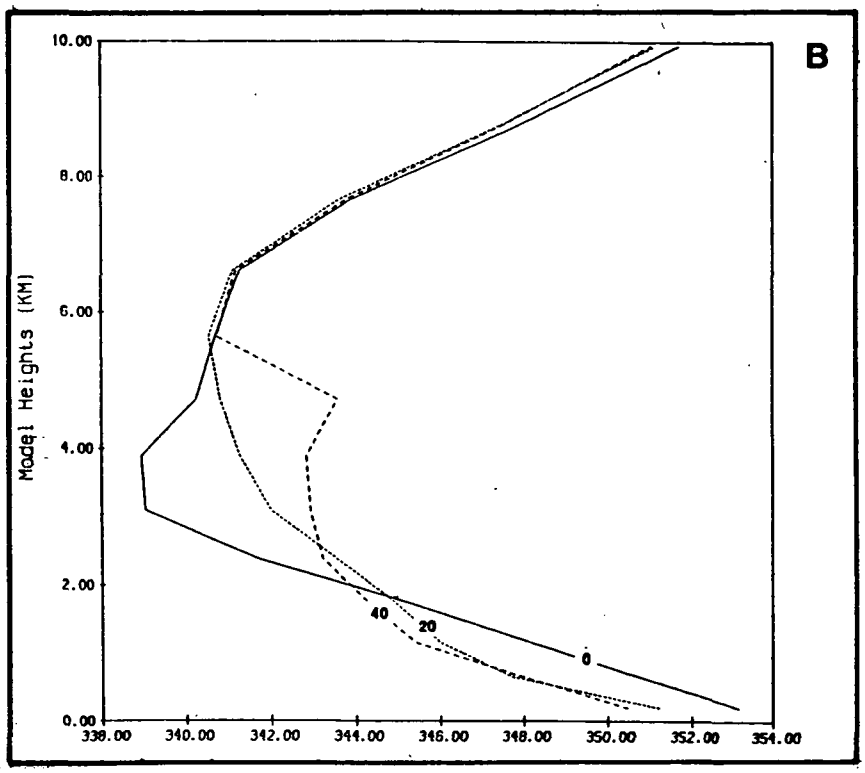

Figure 19b: Same as figure 19a but for the point-B.

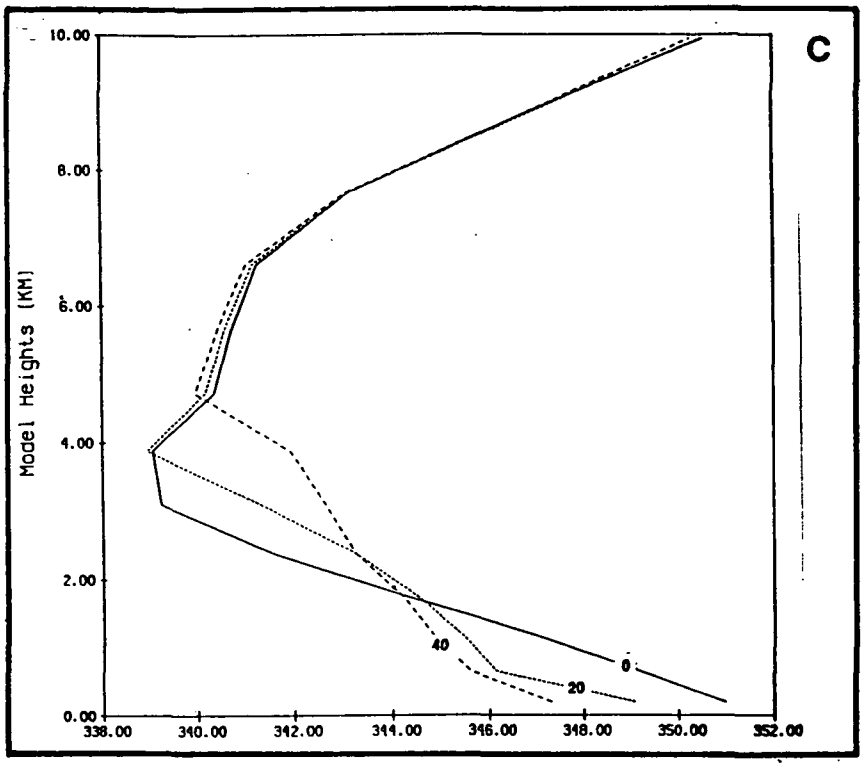

Figure 19c: Same as figure 19a but for the point-C.

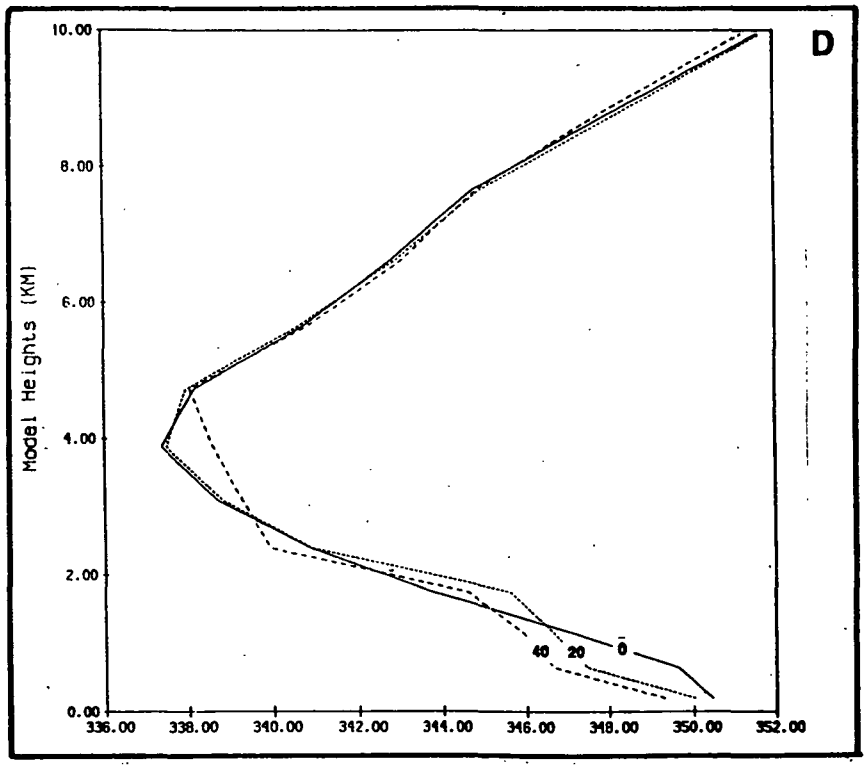

Figure 19d: Same as figure 19a but for the point-D.

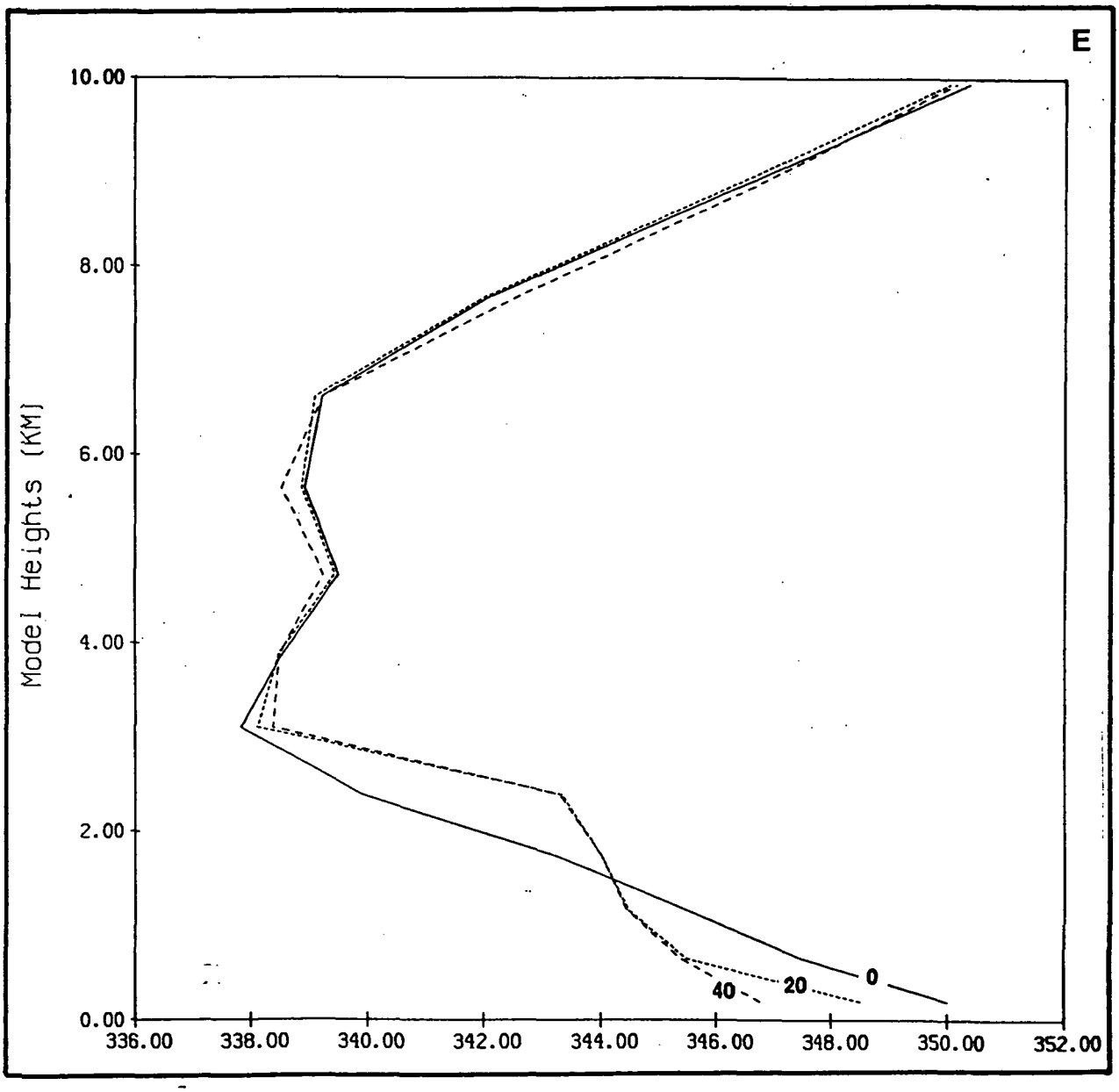

Figure 19e: Same as figure 19a but for the point-E.

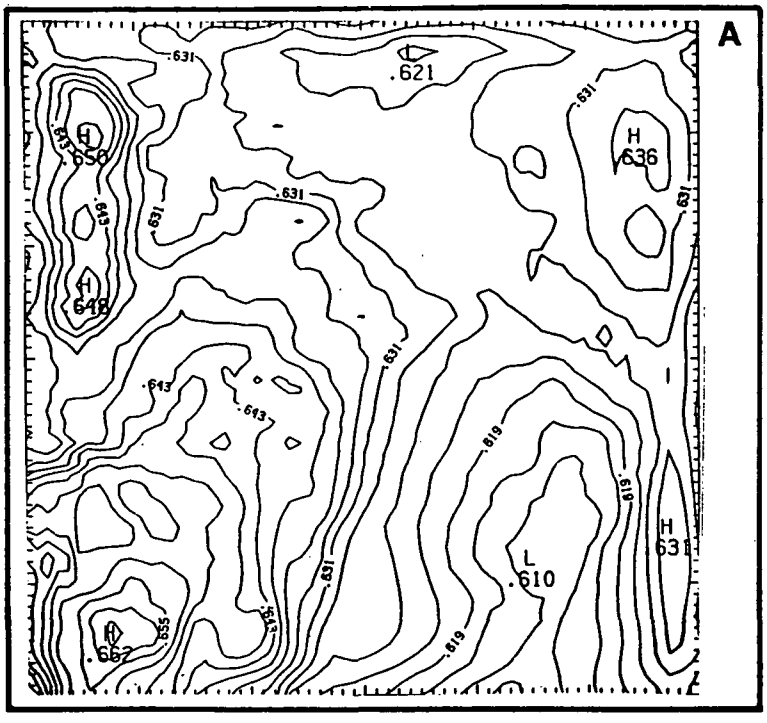

Figure 20a: Horizontal distribution of the buoyancy term over the square-area just enclosing the PAM stations (this square is also the model horizontal domain of all the three-dimensional simulations performed in this study; hereafter referred to as model domain), shown as mass-weighted averages within the model layer of 1-4 km, at 20 minutes of the control simulation. Contours are at intervals of 3 x 10^{-4} ms^2.

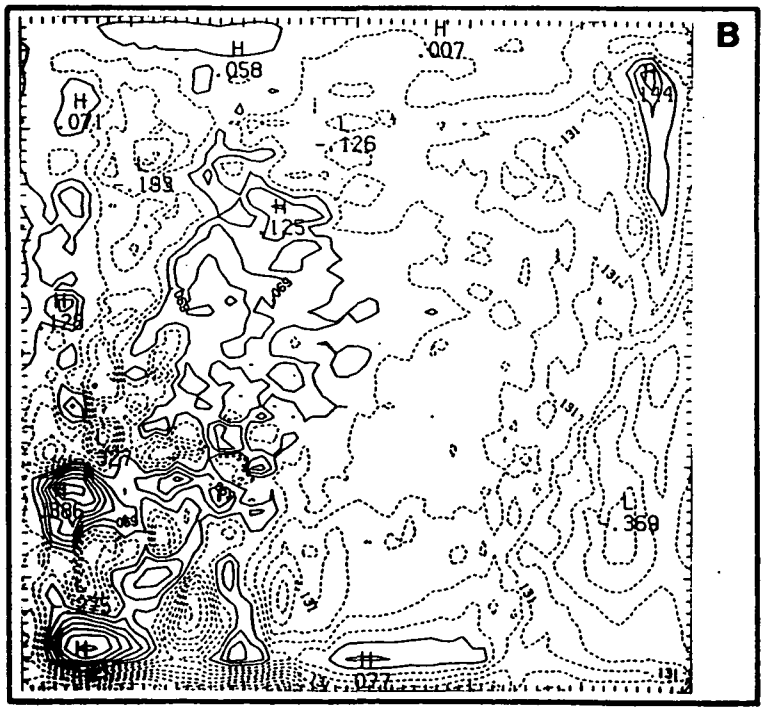

Figure 20b: Same as figure 20a but for the vertical velocities (plotted values are in ms^{-1}; contours are at intervals of 5 cms^{-1} with zero-line not shown).

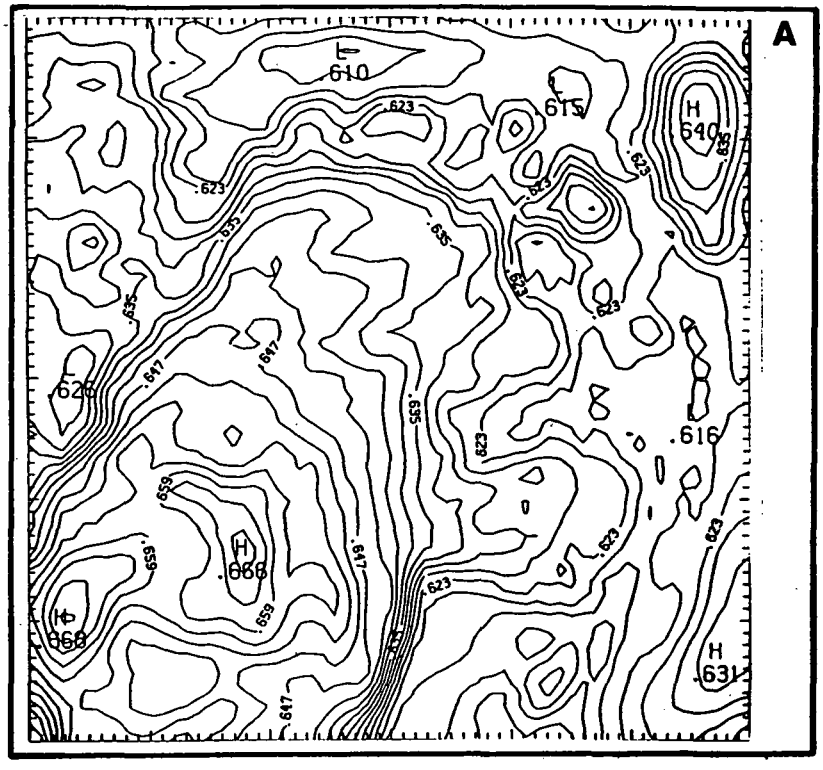

Figure 21a: Same as figure 20a but for 40 minutes of model time.

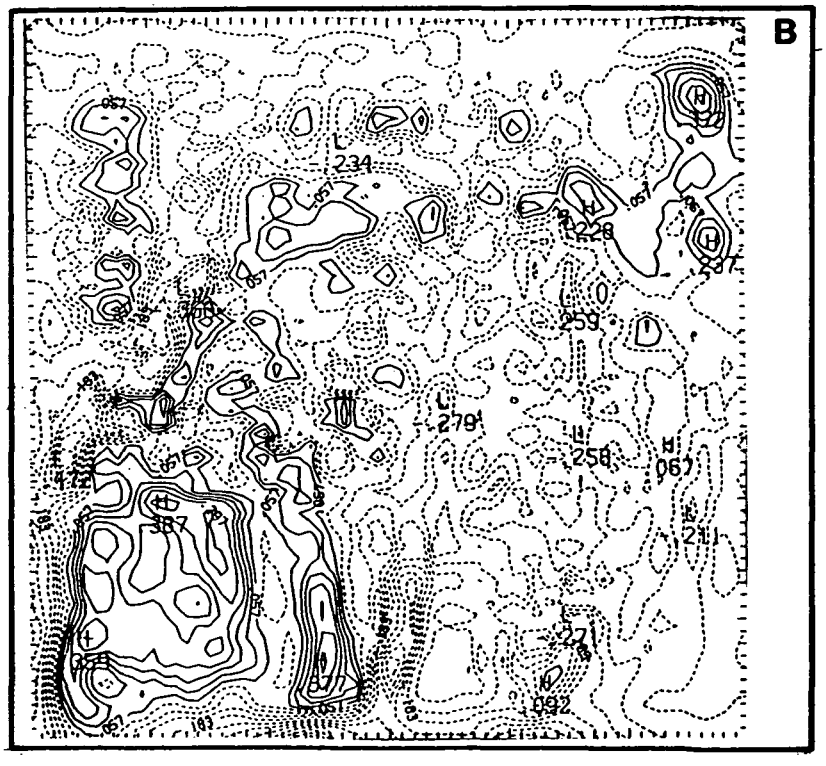

Figure 21b: Same as figure 20b but for 40 minutes of model time.

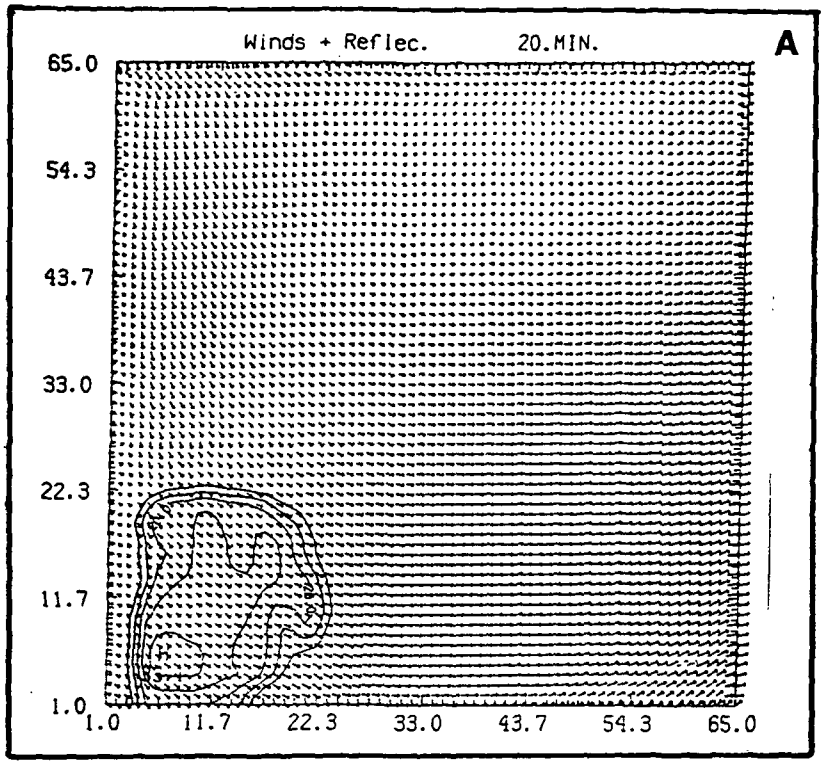

Figure 22a: Mass-weighted model reflectivities and horizontal wind field within the 1-4 km layer over the model domain at 20 minutes of control simulation. Reflectivities are contoured at 10, 20, 30, 40 dBZ, while the length of one grid of the plotted wind vectors denotes a wind speed of 8 ms^{-1}.

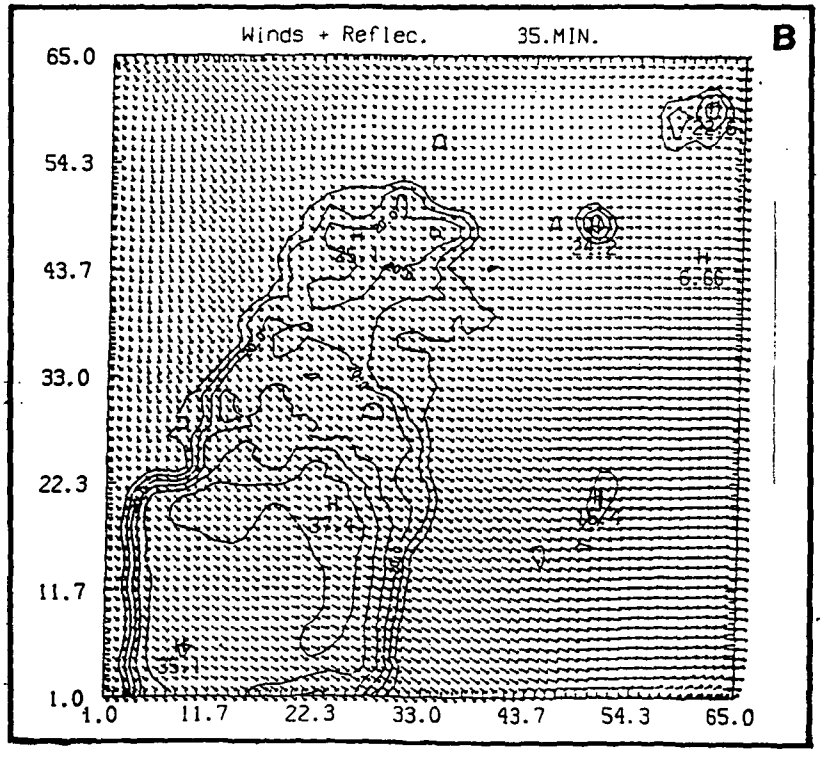

Figure 22b: Same as figure 22a but for 35 minutes of model time.

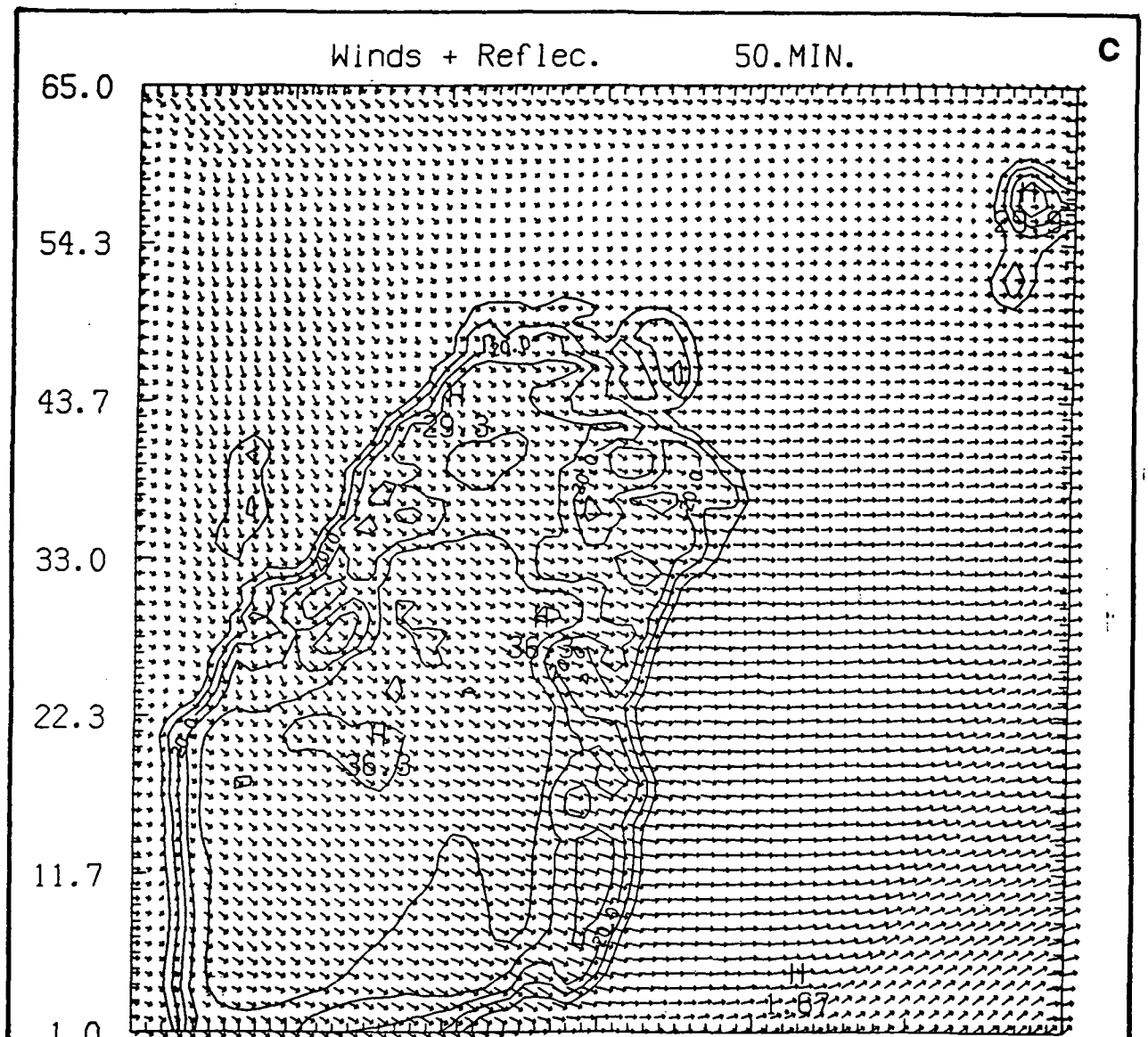

Figure 22c: Same as figure 22a but for 50 minutes of model time.

4. Sensitivity Experiments

4.1 Sensitivity to Surface Input Data

The numerical simulations of this study are all initialized with the gridded data which are constructed from the COHMEX meso-β scale rawinsonde observations. All other data sources of COHMEX, such as the PAM surface data, NWS WSR-57 radar data, NCAR Doppler radar data, Satellite GOES images etc., could indeed each provide a certain unique advantage over a small fraction of the four-dimensional domain considered in this study. However, for the purpose of convective model initialization in this study, only the rawinsonde observations could provide the desired input data.

Nevertheless, in order to see if there may be surface features which contributed to the TCI but not picked up by the rawinsonde observations, a sensitivity simulation was made. This sensitivity simulation is otherwise exactly the same as the control simulation except that the PAM data (described below) replaces the model lowest level input data. The purpose of this simulation is only to see how sensitive the model would be if a small fraction of the total input is replaced with completely independent data.

The PAM data chosen for the sensitivity simulation is the 2115 UTC observation, because this time is considered to be the closest time to the TCI and yet before any cells have been already detected. The wind field of this data is shown in Figure 23a, which shows the same surface convergence zone as shown in Figure 10. Figures 23b and 23c show, respectively, the RH and MSE fields of the PAM data, which can be compared with those of control simulation shown in Figures 11b and 11c. It is seen that the PAM data provides a smoother thermodynamic field around the southwest corner with somewhat lower RH but similar MSE as compared with the sounding-derived data. Over the north central part of the domain, however, the PAM data provides higher MSE air on the surface, as can be seen near Columbia where MSEs are 343-344K (Figure 23c) against only about 341K (Figure 11c).

As in Figure 22, Figures 24a-24c show the model horizontal wind and reflectivity fields within the CL at 20, 35 and 50 minutes of simulation. Comparing Figures 24a-c with Figures 22a-c, respectively, it is seen that the replacement of the model lowest level input with the PAM data does not produce any significant difference during the first 20 minutes but some noticeable differences during the later times. The differences are mainly the enhanced model reflectivities in the downstream area over the eastern one-third of domain, but not with significantly different reflectivity peak values. The three-stages of the TCI (as illustrated in Figure 16) are all qualitatively produced as in the control simulation, without showing large model sensitivities which is as observed.

4.2 *Sensitivity to Surface Random Bubbles*

Another sensitivity simulation was made which is otherwise exactly the same as the control simulation except that a 2°C temperature "bubble" is added to the lowest level at the five analysis points. These bubbles are chosen to occupy only one grid point at one level, and are thus expected to be small enough to not alter the domain energy budgets. The purpose of this sensitivity simulation is only to see if the pre-convective thermodynamic pattern could be easily distorted by simply adding small temperature perturbations at randomly selected grid points.

Figures 25a and 25b show, respectively, the time evolution of model vertical motions and reflectivities within the CL at the five analysis points. Comparing Figures 25 a,b with Figures 18i, 18f, respectively, it is seen that the temperature bubbles are able to produce generally larger upward velocities during the first 20 minutes. For instance, point C has 20-30 cm s^{-1} upward velocities with the bubbles, as compared with fluctuating vertical velocities between ~10 cm s^{-1} and -10 cm s^{-1} in the control simulation during the first 20 minutes. However, Figure 25b shows that the velocity impulses due to the bubbles do not affect the model condensate production in any substantial manner, except perhaps for point C which develops condensate at an earlier time. The pattern of convective evolution is retained.

Similarly to Figure 22, Figures 26a-c show the model wind and reflectivity fields at 20, 35 amd 50 minutes. Comparing Figure 26 with 22, it is seen that the addition of the surface bubbles does not produce significant differences in the model results until the end of the 1-hour simulation. The differences are mainly the somewhat enhanced model reflectivities over the northcentral part of the domain and the eastern portions of domain. Thus, it is further confirmed that the TCI was essentially determined by the pre-convective thermodynamic horizontal distribution within the lower troposphere.

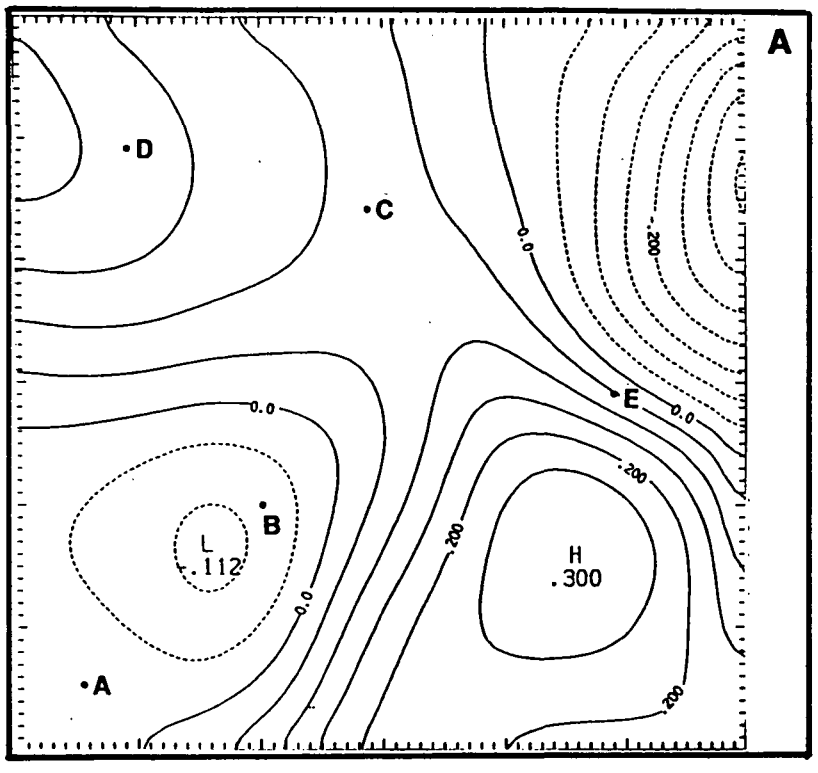

Figure 23a: As in figure 10a but only with the divergence field at 2115 UTC.

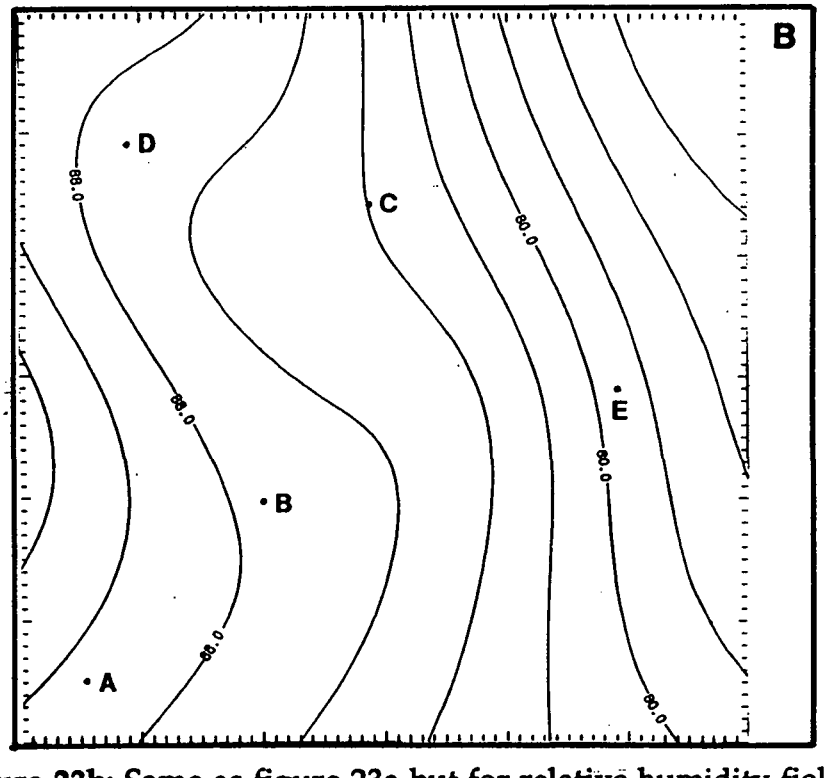

Figure 23b: Same as figure 23a but for relative humidity field.

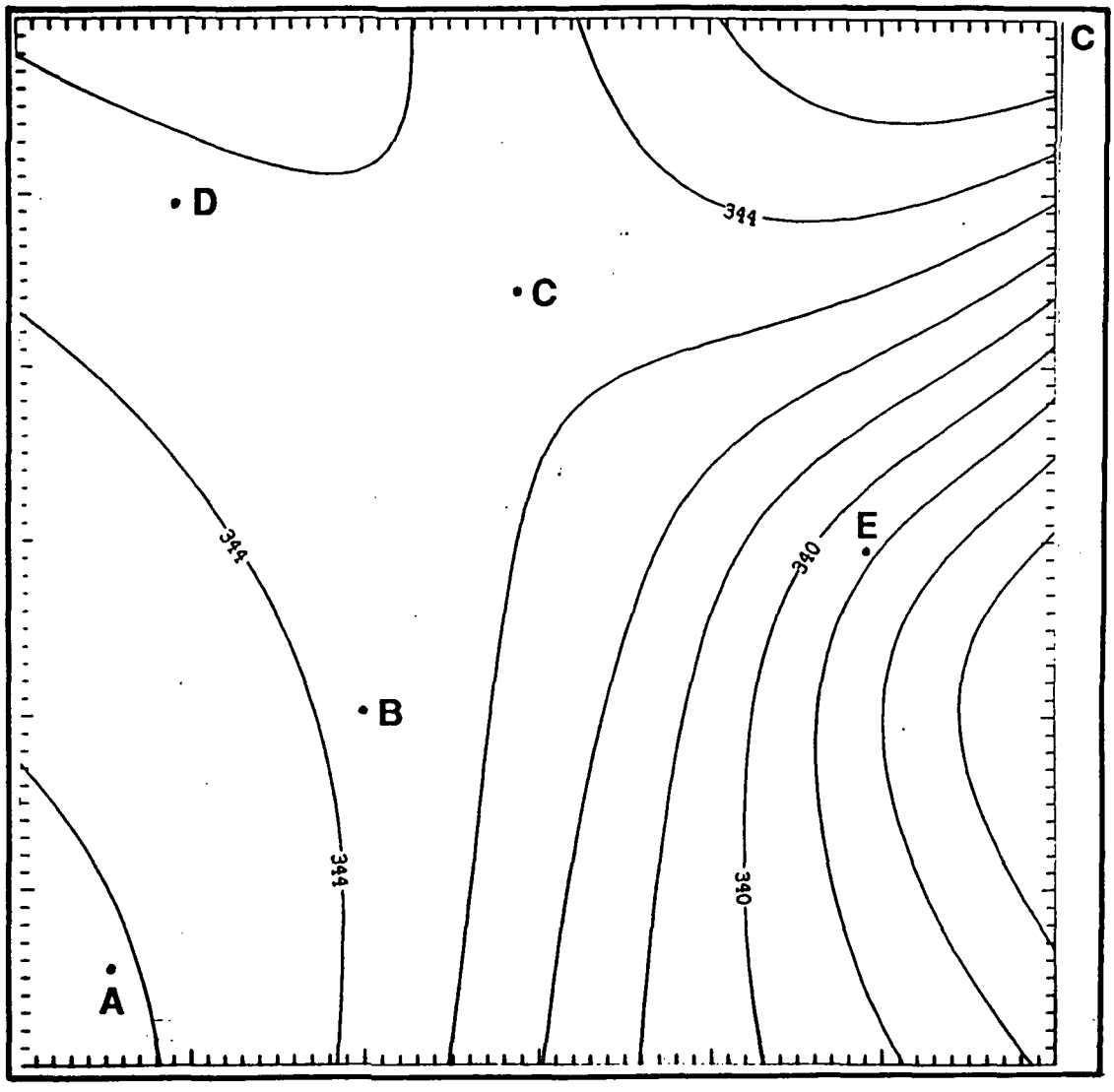

Figure 23c: Same as figure 23a but for the moist-static-energy field.

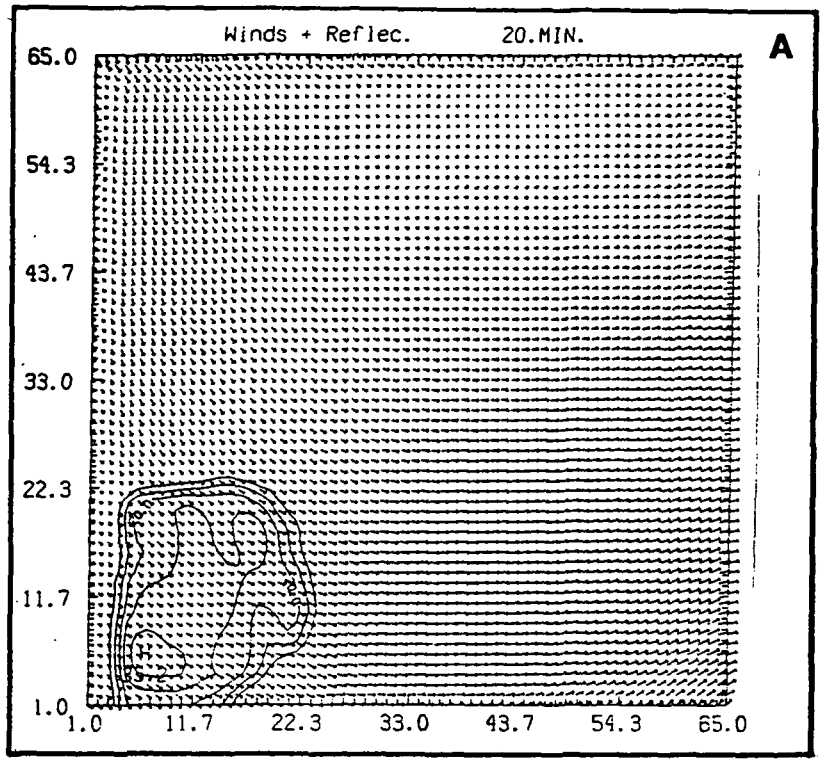

Figure 24a: Same as figure 22a but for the simulation with the lowest input data replaced by the PAM data.

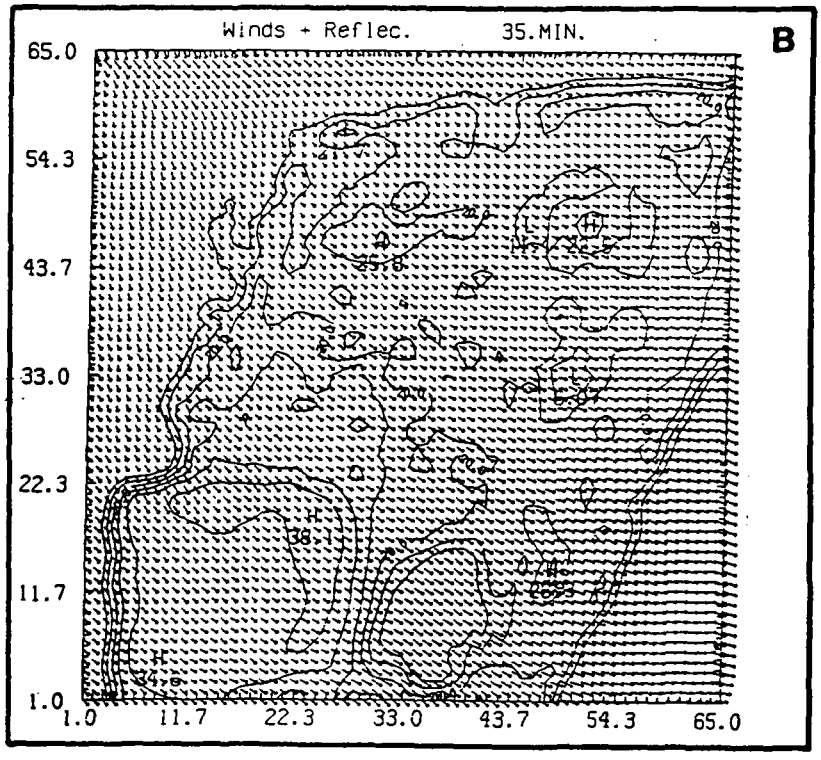

Figure 24b: Same as figure 24a but for 35 minutes of model time.

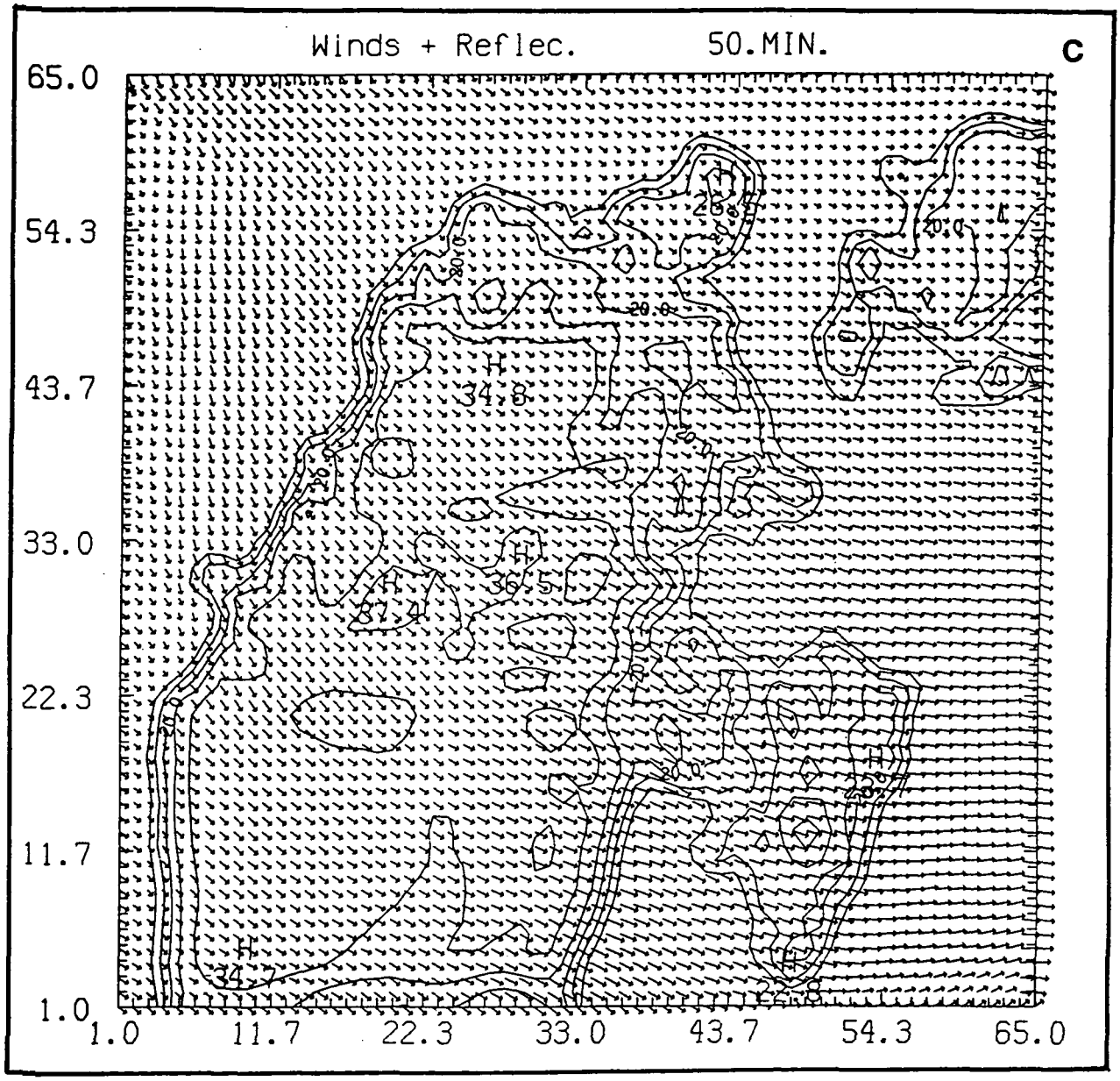

Figure 24c: Same as figure 24a but for 50 minutes of model time.

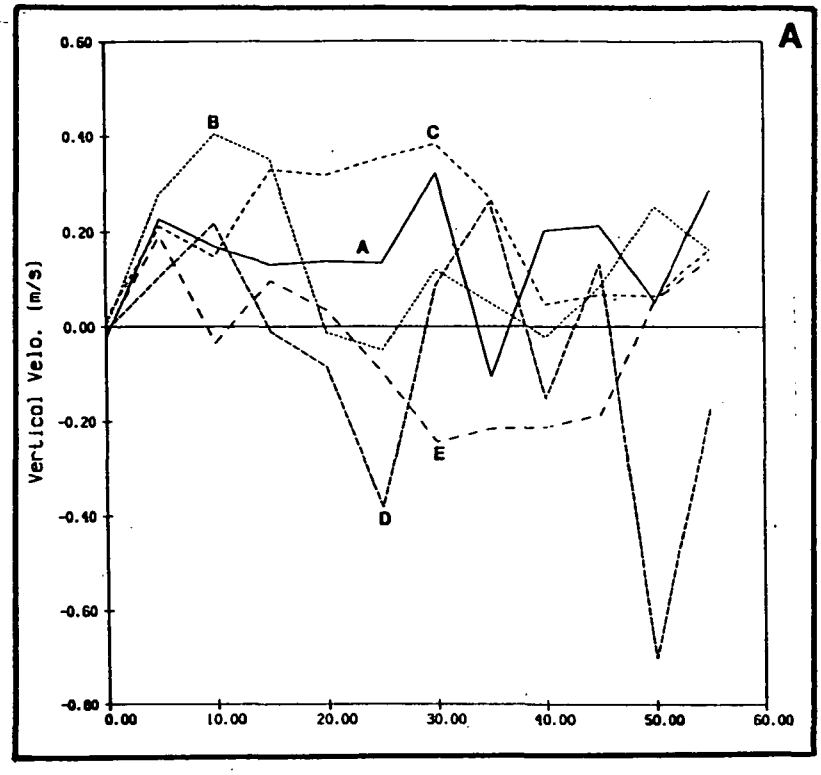

Figure 25a: Same as figure 18i but for the simulation with the PAM data.

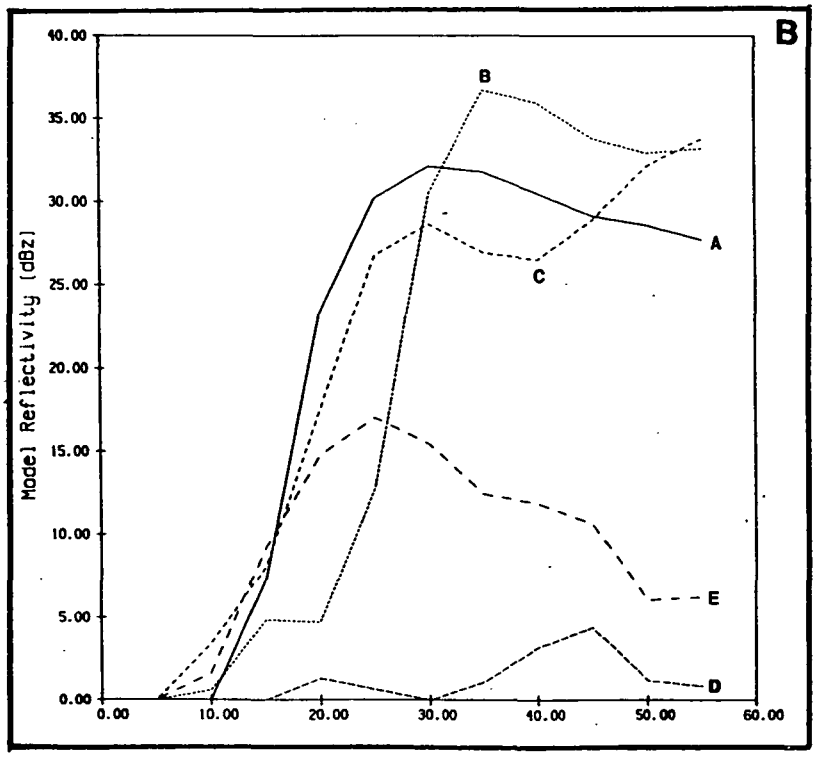

Figure 25b: Same as figure 18f but for the simulation with the PAM data.

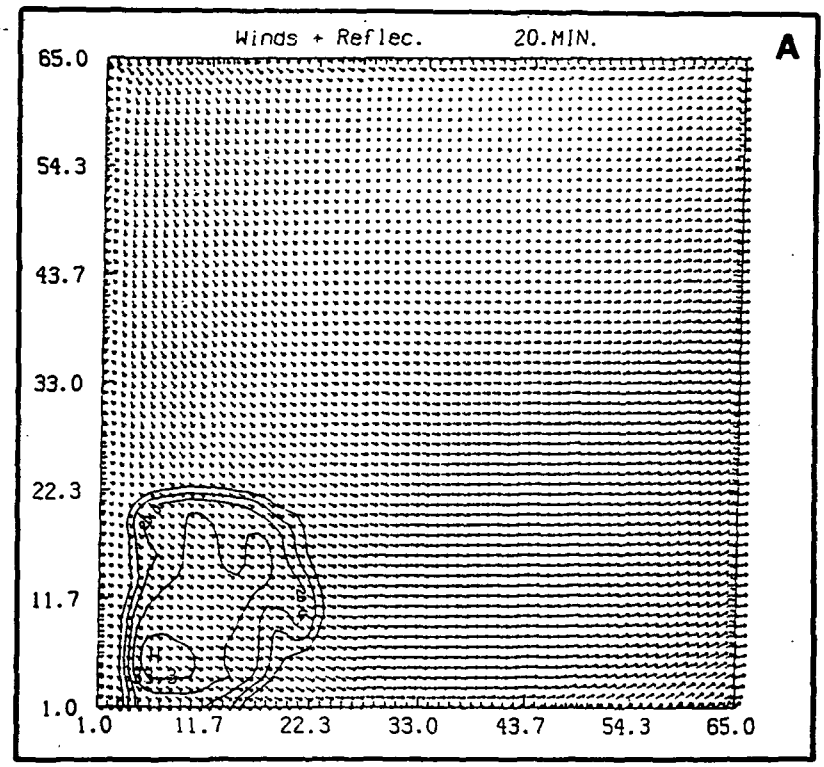

Figure 26a: Same as figure 22a but for the simulation with surface small temperature bubbles added at the 5 chosen points.

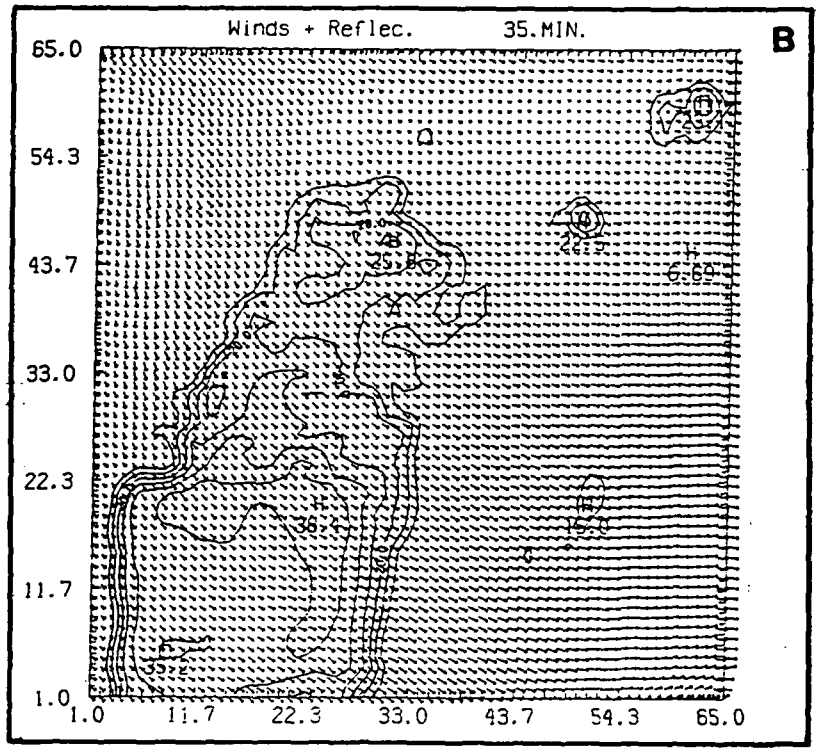

Figure 26b: Same as figure 26a but for 35 minutes of model time.

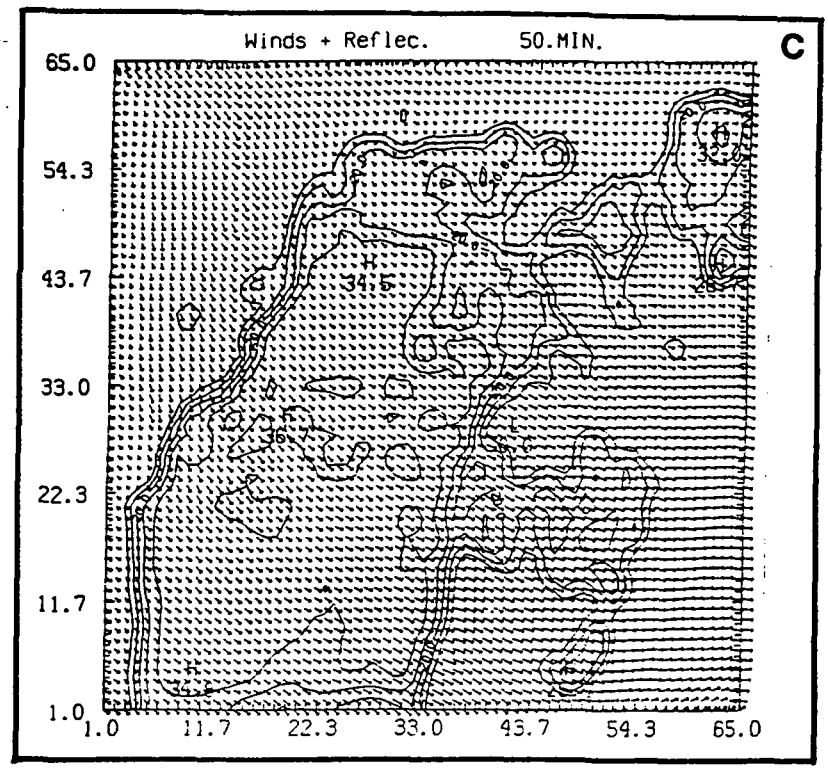

Figure 26c: Same as figure 26a but for 50 minutes of model time.

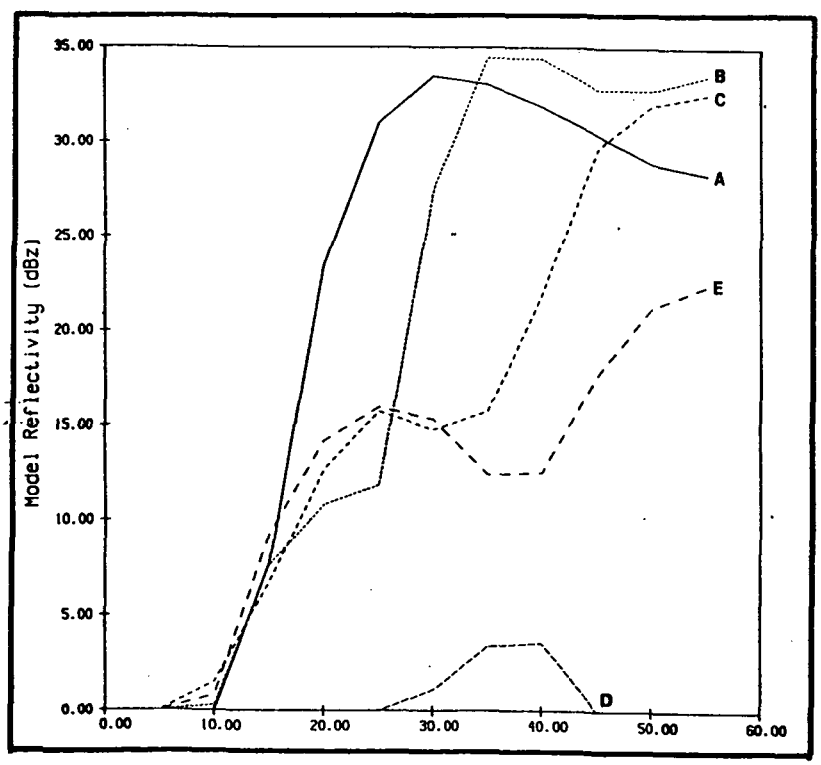

Figure 27: Same as Figure 18f but for the simulation with the initial uniform horizontal winds.

5. Effect Of 3D Wind Field Upon Convective Initiation

As discussed thus far in this study, the TCI was largely a result of the pre-convective mesoscale destabilization due to the low-level moisture supply associated with the background southwesterly flow and the Hurricane Bonnie remnants. Numerical simulations have been shown to be, at least qualitatively, able to reproduce the three stages associated with the TCI, thereby confirming the effect due to the pre-convective thermodynamic pattern. On the other hand, the effect of the wind field associated with the shortwave trough has not been discussed in detail.

In order to determine the impact of the three-dimensional variability in the wind field on the simulation, a TASS run with a horizontally uniform initial wind field was executed. This run was exactly the same as the control simulation with the exception that only the temperature and humidity fields were included in the 3-D initialization. Therefore, the difference, if any, between this and the control simulations would be due to the effect of the "3-D" wind field in the model initialization.

Figure 27 shows the time evolution of model reflectivities at the five analysis points. Comparing Figure 27 with Figure 18f, it is seen that the model condensate evolution at points A, B and D in this uniform-wind simulation are about the same as those in the control simulation. On the other hand, rather clear differences can be found for the point C reflectivities during 20-40 minutes and for the point E after 30 minutes of simulation. For example, at point C, the lack of the 3D initial winds reduces the model condensate production from 25 dBZ to 15 dBZ during 30-35 minutes of simulation. Figures 28a-e show, as in Figure 19, the vertical profiles of equivalent potential temperatures at the five points. By carefully comparing Figures 28a-e with Figures 19a-e, respectively, it is clear that the model convective development:

(1) is essentially the same over the southwest corner area (as represented by points A and B) in both simulations, indicating that this area is the thermodynamically most favored area such that convection will develop regardless of the wind fields (Figures 28a, 28b versus 19a, 19b);

(2) is reduced somewhat over the northeast-extension of the model convection (as in point C) in the uniform-wind simulation only, indicating that the 3D initial wind field may have contributed to organizing the convection such as to develop toward the northeast (Figures 28c versus 19c; note that the differences are during 20-40 minutes of simulation);

(3) is essentially the same over the northwest area (as represented by

point D) in both simulations, indicating this area is the thermodynamically least-favored area such that convection will not develop regardless of the wind fields (Figure 28d versus 19d).

It should be noted that point E is located downstream from the model convective area, and the differences shown in Figures 28e and 19e are during the later times of the simulation. This implies that the differences at point E may be a result of the changes already noted at points A, B and C.

Similar to Figure 22, Figures 29a-c show the model results at 20, 30 and 40 minutes of the uniform-wind simulation. It is seen by comparing Figure 29a with Figure 22a that the lack of the 3D initial wind field does not produce significant differences during the first 20 minutes. In order to show the difference at the later times, Figures 30a-c show, respectively, the "difference fields" (described below) at 20, 30 and 40 minutes of simulation. The "difference fields" are obtained by subtracting the model wind and reflectivity fields within the CL of the uniform-wind simulation from the corresponding fields of the control simulation. Therefore, the horizontal wind fields shown in Figure 30 are the actual "local" wind fields since the constant background wind is subtracted out. First, from Figure 30a it is seen that the local domain-scale cyclonic wind field associated with the shortwave trough seems to have produced only minor differences in the model reflectivity by 20 minutes of simulation.

Between 30 and 40 minutes of simulation, Figures 30b and 30c show that there are quantitative, although not dramatic, differences in terms of the distributions and magnitudes of the model reflectivity production due to the lack of the 3D initial wind field. Figure 30c clearly shows that larger differences in the model reflectivity production are along the northeastern edge of the model convection (*i.e.*, by comparing among Figures 22c, 29c and 30c). The differences are both positive or negative. That is, the 3D initial wind field may have organized the convection in such a way as to both increase and decrease the production of model reflectivities. The increased reflectivities imply enhanced updraft activities, while the decreased reflectivities may imply either weakened updrafts or enhanced downdraft activities.

Therefore, summarizing Figures 30a-c it is seen that there is more convective activity (updraft or downdraft) generated along the northeastern edge of the model convection when the local cyclonic wind field (associated with the shortwave trough) is incorporated into the model initialization, although the differences in reflectivity are not very significant.

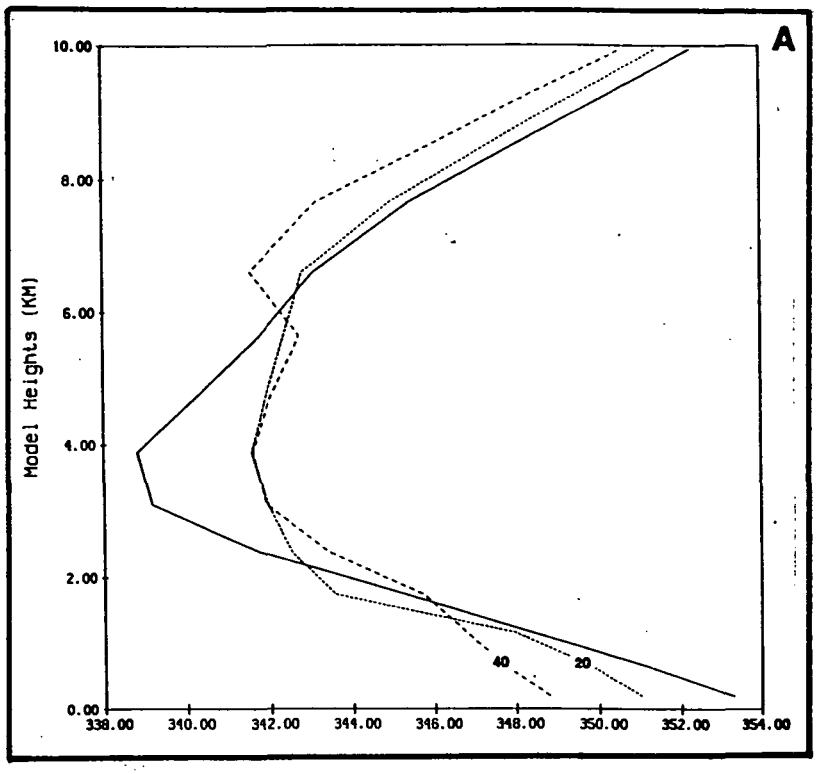

Figure 28a: Same as figure 19a but for the uniform-wind simulation.

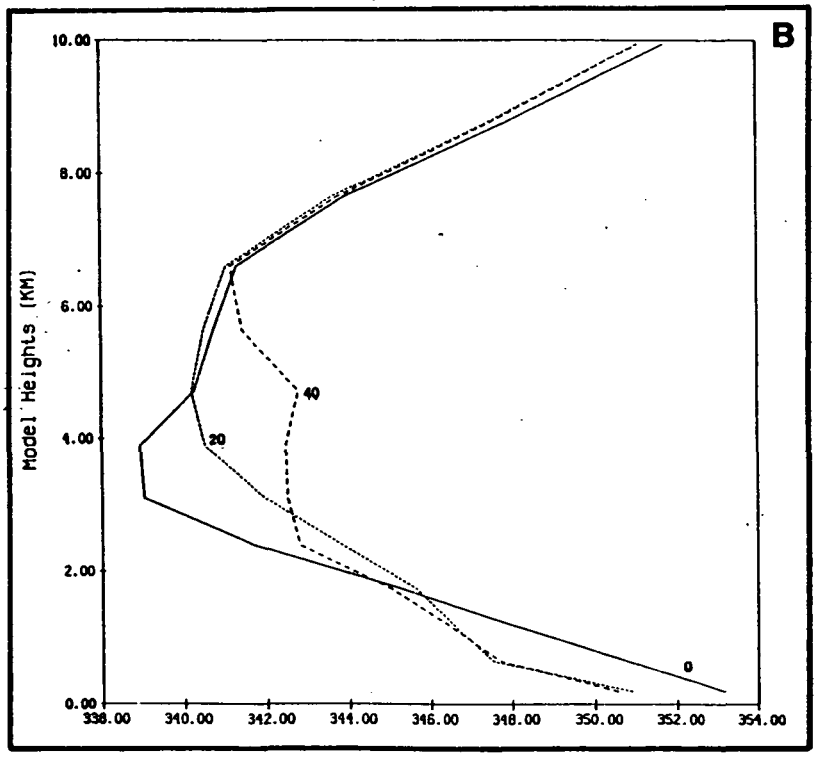

Figure 28b: Same as figure 19b but for the uniform-wind simulation.

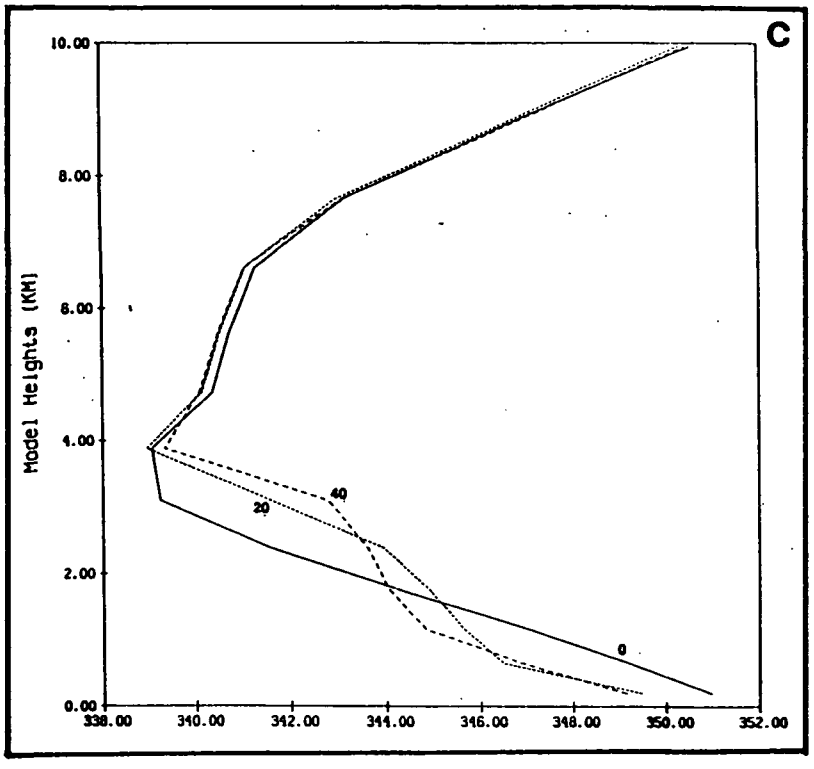

Figure 28c: Same as figure 19c but for the uniform-wind simulation.

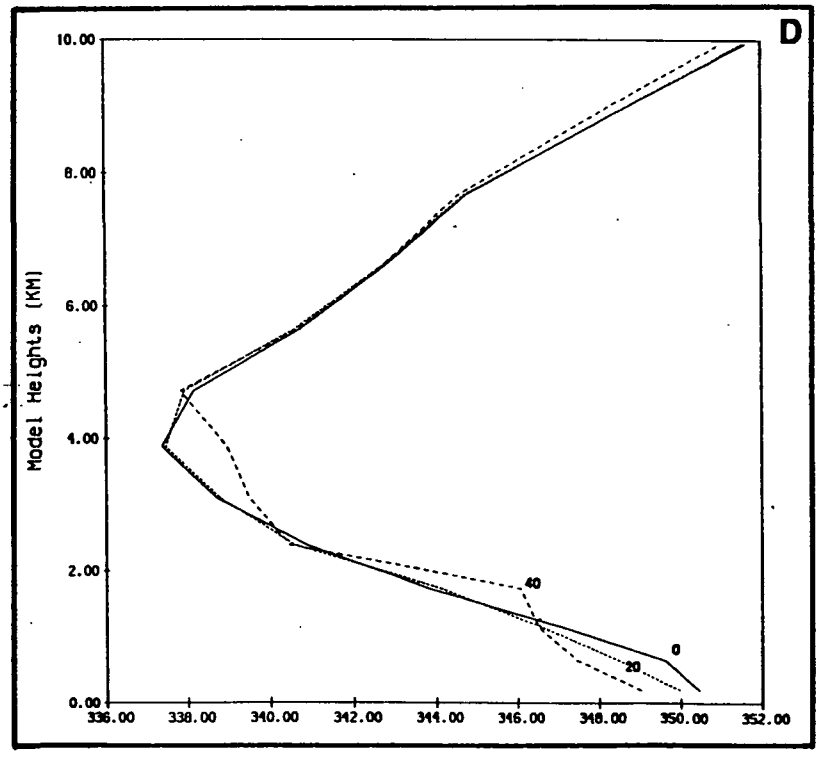

Figure 28d: Same as figure 19d but for the uniform-wind simulation.

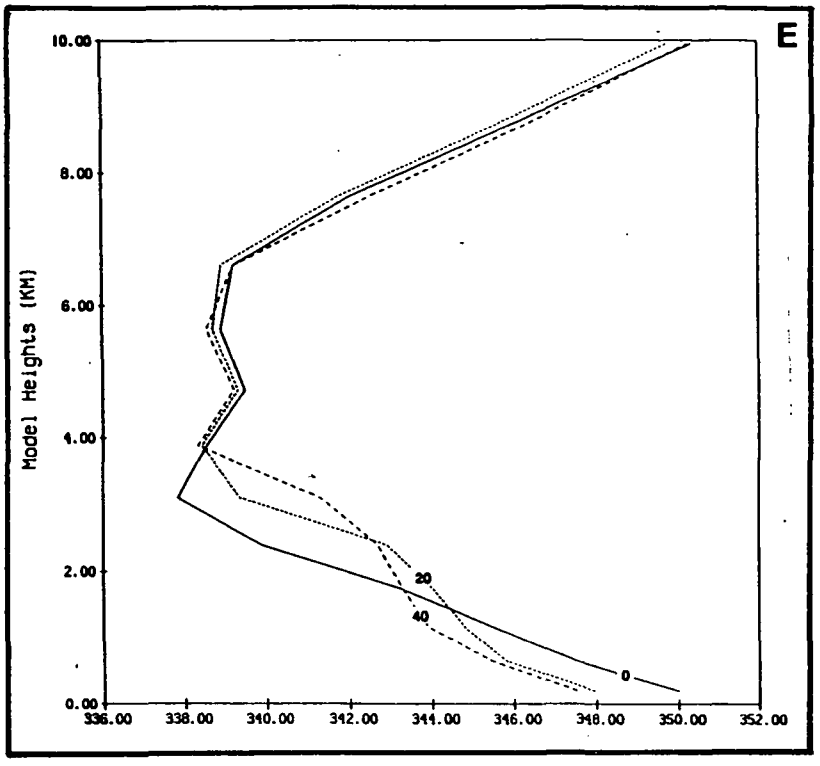

Figure 28e: Same as figure 19e but for the uniform-wind simulation.

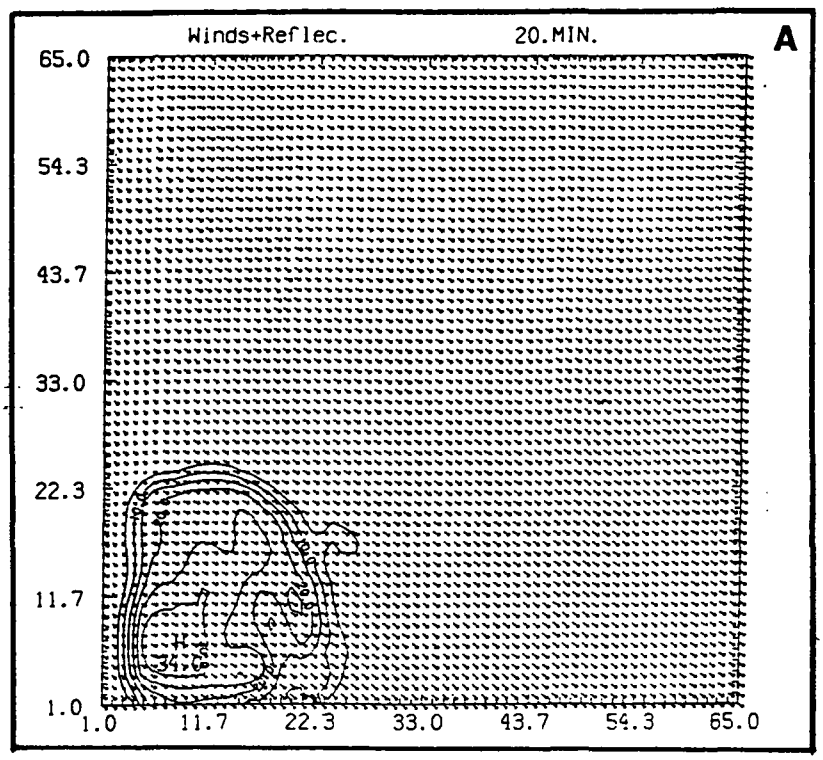

Figure 29a: Same as figure 22a but for the uniform-wind simulation.

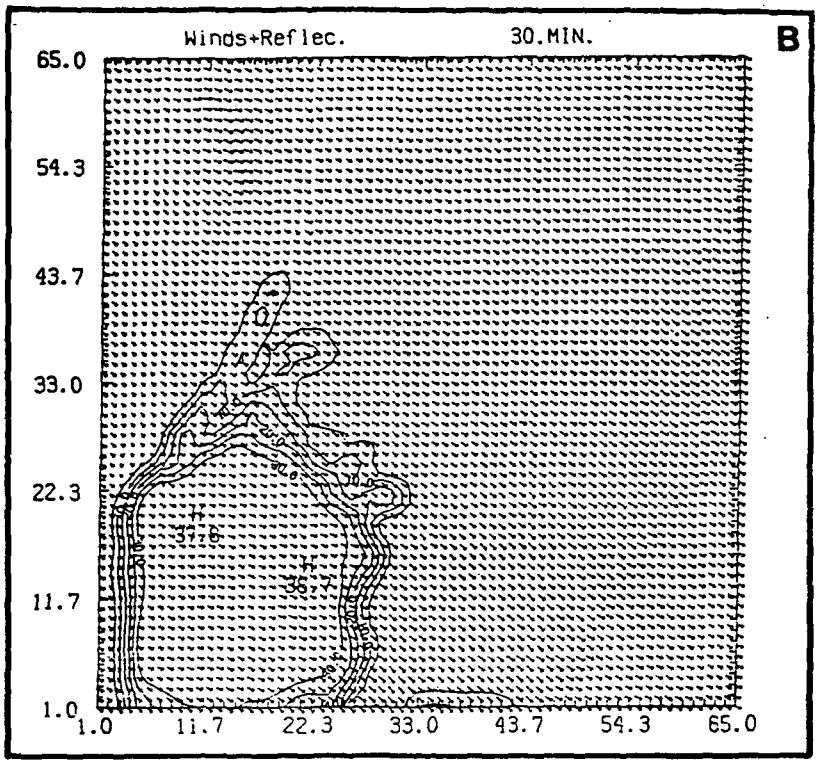

Figure 29b: Same as figure 22b but for the uniform-wind simulation.

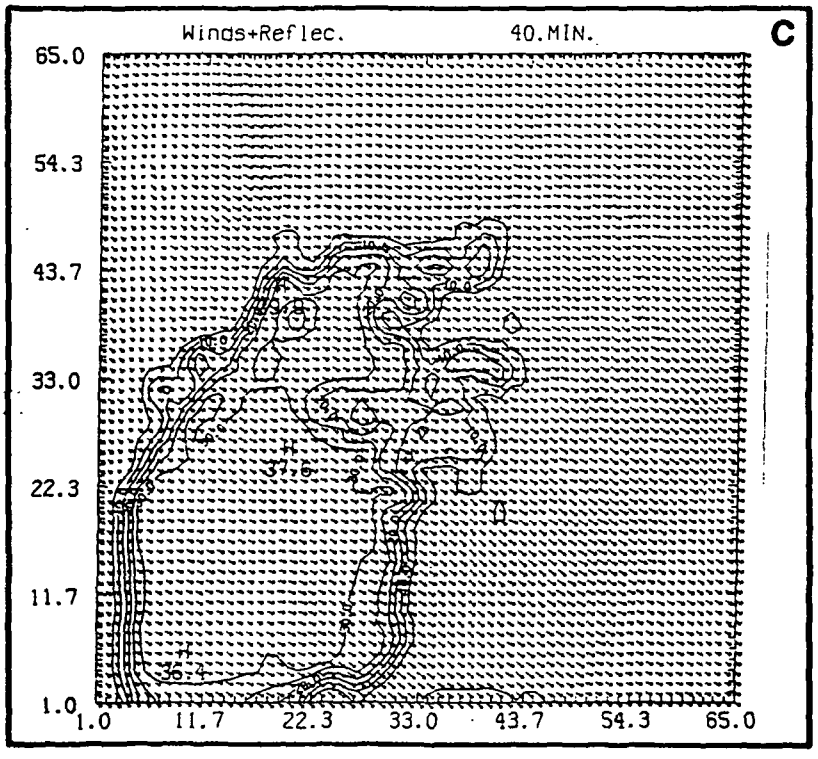

Figure 29c: Same as figure 22c but for the uniform-wind simulation.

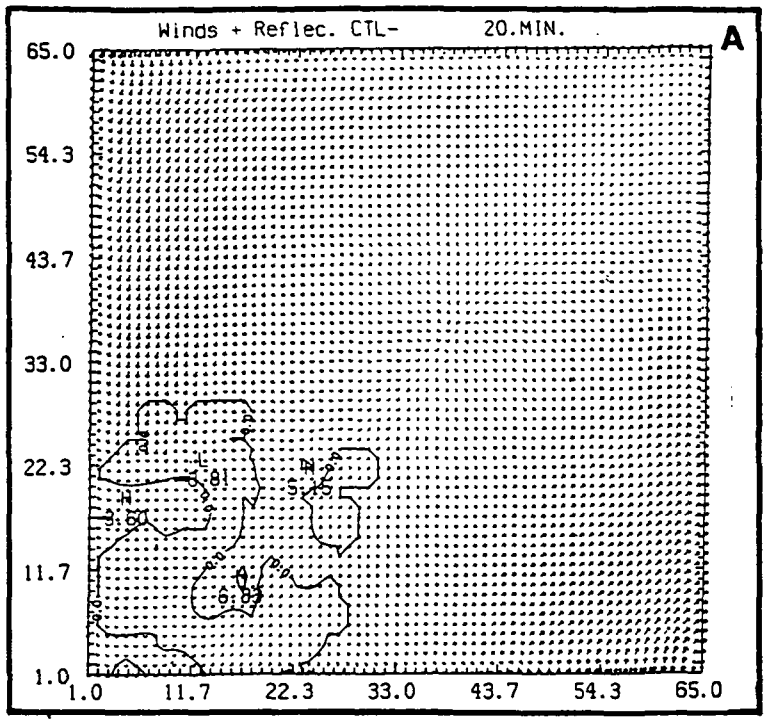

Figure 30a: Superimposing the "difference" field of model horizontal winds upon the "difference" field of model reflectivities at 20 minutes of model time, where the "difference" fields are obtained by subtracting the model quantities in the uniform-wind simulation from the corresponding quantities in the control simulation. The horizontal and vertical domains of these fields are exactly as those in figure 22a.

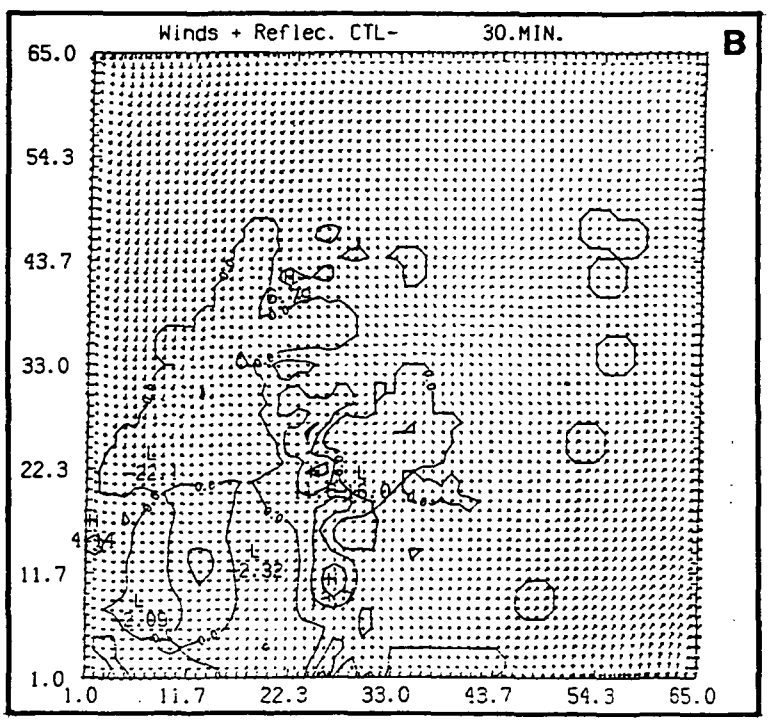

Figure 30b: Same as figure 30a but for 20 minutes of model time.

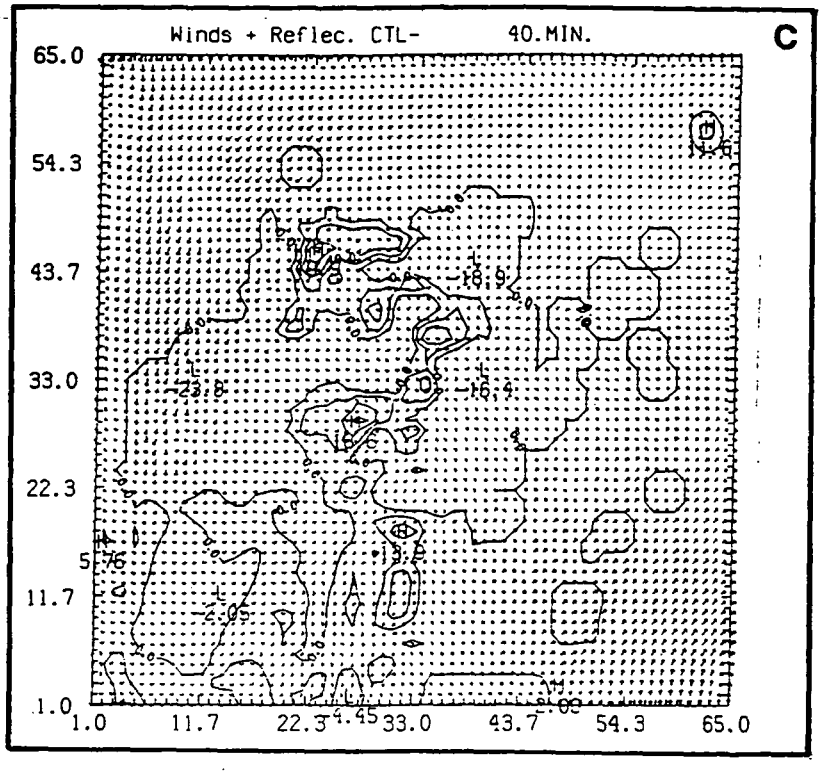

Figure 30c: Same as figure 30a but for 40 minutes of model time.

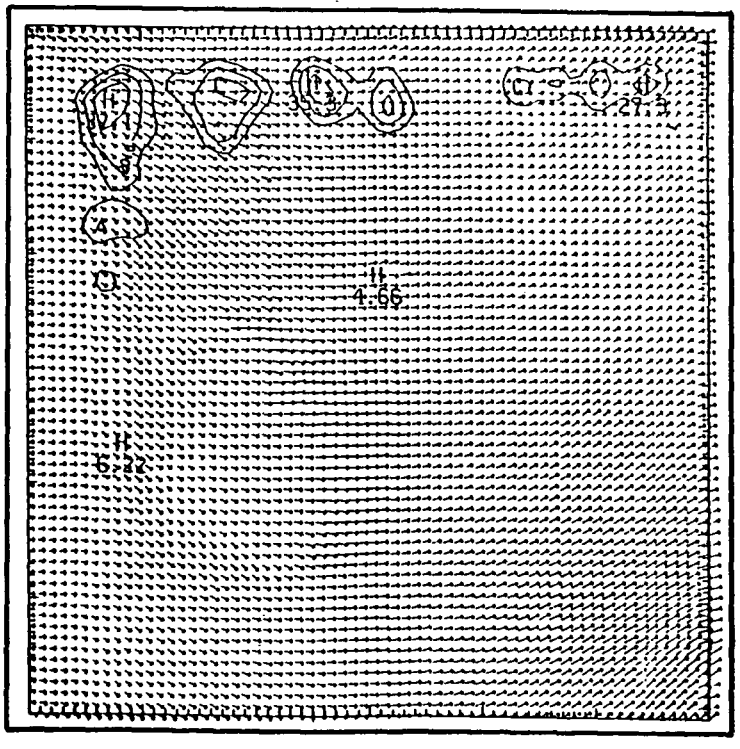

Figure 31: As in figure 22 but for the model result of 1-hour simulation which is initialized with the 2100 UTC data.

6. Implications For Mesoscale Predictability

The actual time of the TCI, as discussed previously, was shortly before 2200 UTC. Given the release times of the soundings (*i.e.* considering only the surface release times), the 0000 UTC and the 2100 UTC soundings provide the input data at 2315 UTC and 2015 UTC, respectively. Therefore, it is unfortunate that the most needed observational information is required in between the two available observations. This shortcoming of the data resource would produce no problem, of course, if there were no mesoscale atmospheric variability over the COHMEX network during the 3-hour period between the two soundings.

As stated previously, the control run of this study used the input data obtained from the 0000 UTC sounding observation. From a "typical" mesoscale modeling point of view, the 2100 UTC sounding data would have been a natural choice because it should describe the closest "pre-convective" situation for use in simulating the TCI. Figure 31 shows, as in Figure 22, the model wind and reflectivity fields from a simulation which is otherwise exactly the same as the control simulation except being initialized with the 2100 UTC data. It is seen clearly from Figure 31 that the model rainfall is over an area which does not appear to be related to the TCI at all. Instead, by comparing Figure 31 with Figure 7 it can be understood that the model rainfall results from the "pre-convective" thermodynamic pattern around 2100 UTC. That is, the model tends to always generate the convective development over the thermodynamically most favored zones which are established during the pre-convective stage.

Therefore, the problem for the 2100 UTC simulation is that the "mesoscale environment" changed during the time gap between the two sounding observations such that the model, which is initialized with only the "snapshot" 2100 UTC data, could not produce the desired convective development. On the other hand, the 0000 UTC simulation (*i.e.* the control simulation) does produce, at least qualitatively, the observed TCI because the model is initialized with the data in which the mesoscale variabilities have been already incorporated.

7. Summary And Conclusions

A convectively explicit simulation, which is initialized using a three-dimensional observed data set, is employed in this study for simulating an observed convective initiation during COHMEX. The physical background chosen for the numerical experiment is a synoptically undisturbed environment. The low-level horizontal moisture distribution is associated with the pre-convective southwesterly flow which tapped abundant upstream moisture producing a meso-β scale (100-200 km length scale) horizontal pattern of substantial observed convective potential. Three-dimensional gridded data in which this pattern is incorporated are used for initializing the convectively explicit simulations. The simulation results show that within the convectively most favorable zone as determined by the pre-convective horizontal pattern, the model produces the earliest convection in the form of lower-tropospheric plumes which root within the turbulent dry boundary layer where the moist PBL produces the lowest LCL. Within a time period of about one hour, the model convection shows a tendency to develop toward the northeast and subsequently the northeastern extension develops most during the later times. Both the earliest convection and the convective tendency are qualitatively verifiable as compared with the observations, thereby indicating the importance of the pre-convective horizontal pattern generated by mesoscale hydrostatic circulations upon the spatial organization of the observed convective initiation.

In this particular case, the pre-convective horizontal pattern appears to be strong enough such that even with completely independent surface observations, replacing the model lowest-level input data, or with a set of temperature impulses specified at randomly chosen grid points, the qualitative nature of the simulation results is not changed. Furthermore, the fact that the model produced convection which is too strong (based on precipitation observations) within the most favorable zone throughout the 1-hour period is due to the effect of the pre-convective pattern of moisture and static energy. The observed three-dimensional wind field in this case is found to be able to produce a quantitative influence upon the spatial organization of the model convection. Since the wind field is associated with the axis of a mid-to-lower tropospheric shortwave trough, the quantitative effect would imply a process-interaction between the synoptic-scale shortwave trough and cumulus convection. *However, the wind effect in this case is not significant when compared with the effect of the pre-convective thermodynamical pattern.*

Large mesoscale atmospheric natural variability is found to be responsible for a relatively dramatic difference between two "pre-convective" patterns separated by a time period of 3 hours or less. The result of such a natural variability in this case is that the simulation could not produce the desired convective initiation within a meso-β scale domain (~200 km across) when it is initialized with an earlier dataset, even if this data is earlier by only 1.5 hours. Therefore, according to the results of

this study, a necessary but not sufficient requirement for producing a meaningful mesoscale prediction over a limited domain, such as that of this study, is that the prediction can be only 1.5 hours in time or less given the specific boundary conditions employed in this study. In concluding this study, it is important to note the major contributions made based on the numerical results summarized above :

(1) Mesoscale boundary layer turbulence fueled by high values of low-level moist static energy and low elevations of the lifting condensation level resulting from a very moist planetary boundary layer are the two crucial ingredients in generating the spatial organization of early-stage convective development or convective 'triggering'.
(2) Periods of 90 minutes are sufficient to allow the hydrostatic scales of motion to modify the distribution of moist static energy and low-level relative humidity to result in a significant change in the pattern of convective initiation.
(3) The meso-γ scale variability of convective initiation patterns is discernible from the distribution of terms in the turbulent kinetic budget within the planetary boundary layer.
(4) Changing the *surface* moisture or the horizontal variability of the low-level wind field produced only minor changes in the position of the convective 'triggering'.

The above conclusions unambiguously indicate that the moisture field between the surface and the top of the planetary boundary layer as well as the thermal buoyancy within the planetary boundary layer strongly control convective initiation and that the hydrostatic motions can drastically modify these distributions over time periods of 1-2 hours.

Finally, as a suggested future study, it seems necessary to carry out a similar investigation but for a strongly "dynamic" event in which the three-dimensional wind field does produce significant effects upon the observed convective initiation. Also, it would be much more realistic and crucial for this study, to provide the limited-domain model with information about the time-dependent mesoscale effects through the lateral boundaries.

8. Acknowledgements

This work was supported by National Aeronautics and Space Administration contract NAS8-37141 under a subcontract to the Universities Space Research Association (USRA) at Huntsville, Alabama. The authors acknowledge the support of Dr. James Dodge of the Mesoscale Research Program at NASA Headquarters. Computations were performed at the CRAY-XMP/416 computer at the NASA/Marshall Space Flight Center (MSFC) at Huntsville, Alabama. Drs. Kevin Knupp and Steve Williams, University of Alabama in Huntsville (UAH), kindly provided the COHMEX data in various useful forms. During the study, comments from Dr. Ken Waight of MESO, Inc., Dr. Fred Proctor, formerly with MESO Inc. in Hampton, Virginia, and now affiliated with NASA/Langley Research Center, Dr. V. Mohan Karyampudi and Dr. Mike Kalb of USRA, Dr. Pete Robertson of MSFC, Dr. Greg Wilson of NASA Headquarters, and Dr. Richard McNider of UAH, among others, contributed significantly to the performance of this research. Ms. Jayanthi Srikishen, Ms. Lori McCain and Mr. Matt Smith are thanked for their help on the computer work and draft preparation.

9. References

Anthes, R. A., 1977: Hurricane model experiments with a new cumulus parameterization scheme. *Mon. Wea. Rev.*, **105**, 287-300.

Balaji,V. and T. L. Clark, 1988: Scale selection in locally forced convective fields and the initiation of deep cumulus. *J. Atmos. Sci.*, **45**, 3188-3211.

Bolton, D., 1980: The computation of equivalent potential temperature. *Mon. Wea. Rev.*, **108**, 1046-1053.

Businger, J. A., J. C. Wyngaard, Y. Izumi and E. F. Bradley, 1971: Flux-profile relationships in the atmospheric surface layer. *J. Atmos. Sci.*, **28**, 181-189.

Carbone, R. E., J. W. Conway, N. A. Crook and M. W. Moncrieff, 1990: The generation and propagation of a nocturnal squall line. Part I: Observation and implication for mesoscale predictability. *Mon. Wea. Rev.*, **118**, 26-49.

Clark, T. L., *1979:* Numerical simulations with a three-dimensional cloud model: lateral boundary condition experiments and multicellular severe storm simulations. *J. Atmos. Sci.*, **36**, 2191-2215.

Cotton, W. R. and G. T. Tripoli, 1978: Cumulus convection in shear flow; three-dimensional numerical experiment. *J. Atmos. Sci.*, **35**, 1503-1521.

Crook, N. A., R. E. Carbone, M. W. Moncrieff and J. W. Conway, 1990: The generation and propagation of a nocturnal squall line. Part II: Numerical simulations. *Mon. Wea. Rev.*, **118**, 50-65.

Crook, N. A. and M. W. Moncrieff, 1988: The effect of large scale convergence on the generation and maintenance of deep moist convection. *J. Atmos. Sci.*, **45**, 3606-3624.

Fritsch, J. M., and C. F. Chappell, 1980: Numerical prediction of convectively driven mesoscale pressure systems. Part I: convective parameterization. *J. Atmos. Sci.*, **37**, 1722-1733.

Klemp, J. B., R. B. Wilhelmson and P. Ray, 1981: Observed and numerically simulated structure of a mature supercell thunderstorm. *J. Atmos. Sci.*, **38**, 1558-1580.

Klemp, J. B. and R. B. Wilhelmson, 1978: The simulation of three-dimensional convective storm dynamics. *J. Atmos. Sci.*, **35**, 1070-1096.

Knupp, K. R. and S. F. Williams, 1988: Multiscale analysis of a sustained precipitation event. 12th Conference on Severe Local Storms, Feb 22-26, 1988, Baltimore, MD.

Lafore, J.-P. and M. W. Moncrieff, 1989: A numerical investigation of the scale interaction between a tropical squall line and its environment. *J. Atmos. Sci.*, **46**, 521-544.

Proctor, F. H., 1987a: The Terminal Area Simulation System. Volume I: Theoretical formulation. NASA Contractor Rep. 4046, 176 pp.

_____, 1987b: The Terminal Area Simulation System. Volume II: Verification experiments. NASA Contractor Rep. 4047, 112 pp.

_____, 1988: Numerical simulations of an isolated microburst. Part I: Dynamics and structure. *J. Atmos. Sci.*, **45**, 3137-3160.

Redelsberger, J. L. and T. Clark, 1990: The initiation and horizontal scale selection of convection over gentle sloping terrain. *J. Atmos. Sci.*, **47**, 516-541.

Schlesinger,R. E., 1982 : Effects of mesoscale lifting, precipitation and boundary layer shear on severe storm dynamics in a three-dimensional numerical modeling study, Preprints 12th Conf. on Severe Local Storms, San Antonio, Amer. Meteor. Soc., 536-541.

Stull, R. B., 1988: An Introduction to Boundary Layer Meteorology. Kluwer Academic Publishers, 666 pp.

Tripoli, G. J. and W. R. Cotton, 1989a: A numerical study of an observed orogenic mesoscale convective system. Part I: Simulated genesis and comparison with observation. *Mon. Wea. Rev.*, 117, 273-304.

Tripoli, G. J. and W. R. Cotton, 1989b: A numerical study of an observed orogenic mesoscale convective system. Part II: Analysis of governing dynamics. *Mon. Wea. Rev.*, 117, 273-304.

Wilhelmson, R. B. and C. S. Chen, 1982: A simulation of the development of successive cells along a cold outflow boundary. *J. Atmos. Sci.*, 39, 1466-1483.

Williams, S.F., H. M. Goodman, K. R. Knupp and J. E. Arnold, 1987: SPACE/COHMEX Data Inventory Document. NASA TM-4006, Marshall Space Flight Center, AL, 480pp.

Yoshizaki, M. and Y. Ogura, 1988: Two- and three-dimensional modeling studies of the Big-Thompson storm. *J. Atmos. Sci.*, 45, 3700-3722.